

For New Technology Network

NTN®

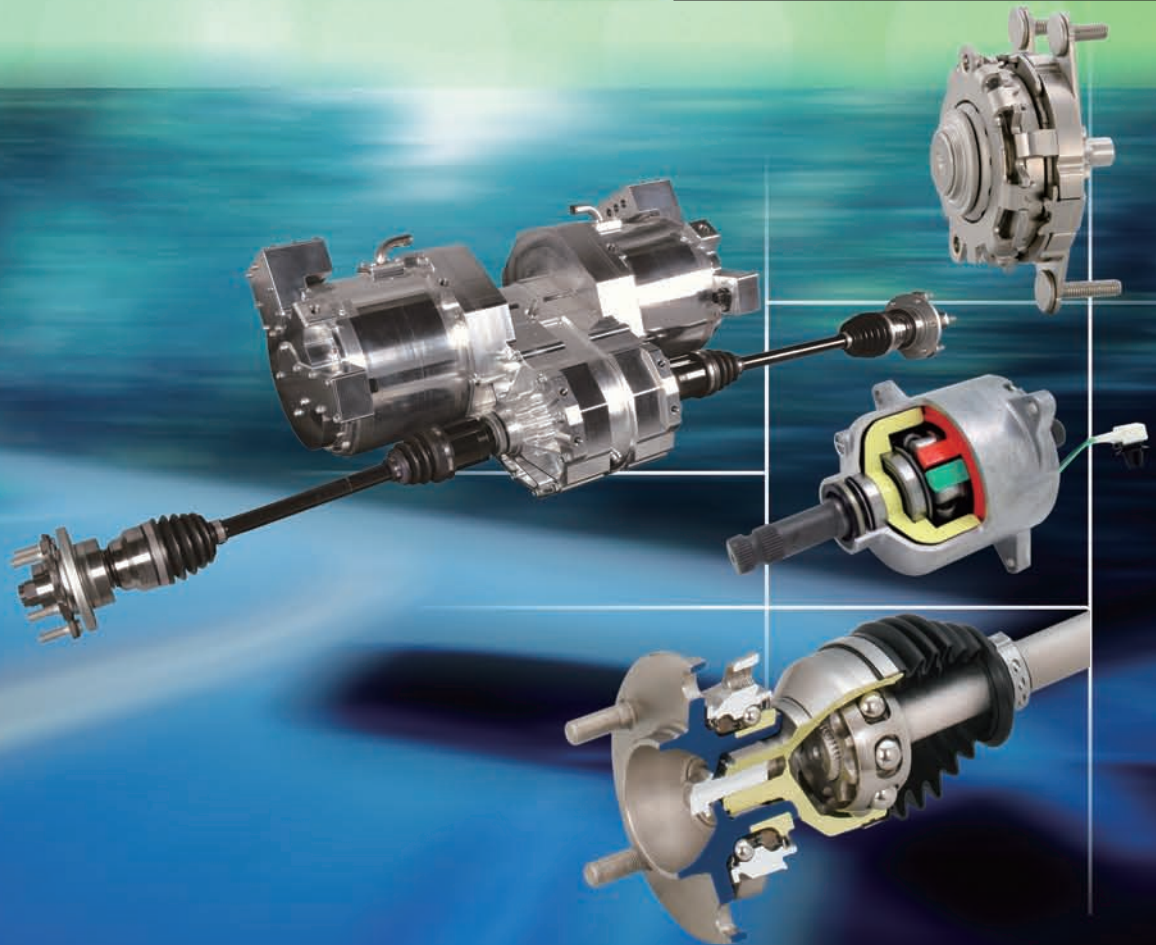
TECHNICAL REVIEW

No.

83

Special Issue for
Automotive Module Products

October 2015



NEW TECHNOLOGY TRANSFORMS THE NEXT



**Mechanical clutch unit (MCU)
for next-generation steering**



**Ball screw drive module
for electrohydraulic brakes**



Clutch for seat lifter



**Sensor embedded
third-generation hub bearings**



**Press connect spline hub joint
(PCS-H/J)**



Various bearings

NTN[®]



TECHNICAL REVIEW

No.83

Special Issue;

Automotive Module Products

NTN TECHNICAL REVIEW No.83

CONTENTS

Preface	Yoshinori TERASAKA	1
Contribution	Highly Efficient and Responsive Motor Drive Technologies Enable Robotics to Evolve Automobile into Autonomous Service Robots Hisashi TAKAHASHI Professor, Graduate School of Science and Technology, Shizuoka Institute of Science and Technology	2
Perspective	Electrification of the Automobile and Module Products of NTN Makoto OKASAKA	16

● Special Issue for Automotive Module Products

Two Motor On-board Drive System Ryou YUKISHIMA, Hidenori KARASAWA, Aiko MYOUKI, Katsunori SATOU, Yusuke MAKINO, Takeshi KANDA and Tomohiro SUGAI	20
Rear-wheel Independent Steering System Yasuhiro MATSUNAGA, Tatsuji INOUE, Hironori TOKUNAGA and Yukihiro NISHIO	26
MCU (Mechanical Clutch Unit) for Next Generation Steering Naotsugu KITAYAMA and Shintaro ISHIKAWA	32
Clutch for Seat Lifter Masayoshi YAMADA and Yasumasa HIBI	36
Next-generation Drive-shaft "ADS Module" Masafumi OOSUGI and Tatsuro SUGIYAMA	40
Technology Trends and Products for Accessory Drive Belt Systems Ayumi AKIYAMA and Hiroo MORIMOTO	43
Auto Tensioner with Variable Damper Mechanism for ISG-equipped Engines Hiroo MORIMOTO and Yuta MOCHIZUKI	48
Products Introduction of Composite Material for Automotive Kayo SAKAI, Eiichirou SHIMAZU, Takahiro GOTOU, Hajime ASADA and Takuya ISHII	54

● Technical Papers New Products

Modeling of Retained Austenite Transformation in Bearing Steels Christine SIDOROFF, Pierre DIERICKX and Pr. Michel PEREZ	60
Evaluation of Rolling Contact Fatigue by X-ray Diffraction Ring Naoya KAMURA, Takumi FUJITA and Toshihiko SASAKI	67
Influence of Induction Heating Conditions on Bearing Steel Characteristics Hiroshi YUKI and Miyu SATO	75
Grease Lubricated High-speed Deep Groove Ball Bearing for EV and HEV Motor Masahiko SATODA and Goro NAKAO	81
Deep Groove Ball Bearing for Alternator Corresponding to 200°C Tomoyoshi IZUTSU and Goro NAKAO	86
3D Microgeometry Measuring Machine Hiroaki OBA	91
High-speed Microscopic Coating Applicator Akihiro YAMANAKA	98

● Award Winning Products

"CHO" MONODZUKURI Innovative Parts and Components Award, "2014 Automotive Components Award" Mechanical Clutch Unit for Direct Adaptive Steering Naotsugu KITAYAMA and Shintaro ISHIKAWA	104
AVEC'14 "Best Paper Award" Roll Control Using Tire Longitudinal Forces Integrated with Tire Force Distribution of Full Drive-by-Wire Electric Vehicle Yuta SUZUKI, Tomohiro SUGAI, Junichi HIRATA and Nobuyuki SUZUKI	105

Our Line of New Products	106
---------------------------------	-----

Message for the Automotive Module Products Special Issue



Yoshinori TERASAKA
Managing Director

Due to growth of vehicles in emerging markets, the total number of vehicles produced globally has reached well over 80 million units, which has created an imminent challenge of reducing fuel consumption for mitigating global warming. In this regard, auto manufacturers are responding to this challenge by introducing eco-friendly vehicles with various modified drive systems such as vehicles with improved traditional internal-combustion engines, hybrid vehicles and electric vehicles.

For addressing these social requirements, NTN is not only exploring further improvement in miniaturization/lightweight technology, low friction technology and long-life technology that we have been successfully developing, but also accelerating development of various highly functional module products by combining electronic control technology to these technologies.

On this occasion of the 44th Tokyo Motor Show from Oct. 28 to Nov. 8, with the theme of “Your Heart Will Race”, this special issue was created featuring state-of-the-art module products/technology for vehicles. In this issue, we have asked Professor Hisashi Takahashi of Shizuoka Institute of Science and Technology to explain the trend of motor control technology, which is indispensable for module products.

In addition, we are introducing “automotive module products” in this special issue, including a two-motor on-board driving system characterized by both high motion performance and safety functionality, MCU for next-generation steering systems and a next-generation lightweight drive shaft, “ADS Module”, that uses new bonding technology. Further, we present basic research papers that affect the material evaluation methods and material properties, as well as bearing products for automotive use such as the grease lubricated high-speed deep groove ball bearing and bearing for alternators that can withstand 200°C.

At NTN, we will celebrate our 100th anniversary in fiscal year 2017. Starting fiscal year 2015 through fiscal year 2018, we will drive our mid-term management plan “NTN100” building foundation for ongoing growth in the next 100 years, following our theme, “For New Technology Network: We shall contribute to international society through creating new technologies and developing new products,” contributing for sustainable development of the industry through our eco-friendly product development.

For New Technology Network

Highly Efficient and Responsive Motor Drive Technologies Enable Robotics to Evolve Automobile into Autonomous Service Robots



Hisashi TAKAHASHI

Professor, Graduate School of Science and Technology,
Shizuoka Institute of Science and Technology

Electric motor-driven automobiles (EV) are getting a great deal of attention over conventional internal combustion engine-powered automobiles since EV is seen as a potential solution to the environmental pollution and energy crisis possible in the not too distant future. Electric motors, the power source of EV, are responsive in controlling the torque and it makes precise control of regenerative brake and vehicle body dynamics possible. Making use of the advantage of electric motor, by incorporating the vehicle navigation system, imaging, and radar technologies, which are now affordable to wide range of automobiles, automobiles are being transformed

from a means just to transport to a machine of robotics for even safer, more efficient, and more comfortable mobility. To make this happen, smaller-sized and highly efficient motors and inverters, and others like batteries with greater capacity and extended longevity are in great demand. This paper presents newest or most recent technologies essential for developing those building blocks in the automobile evolution including motor control technologies, application technologies of inverter and converter, sensorless control technologies, how to deal with the problem caused from the current leakage, and others which are existing and waiting extended study.

1. Introduction

Solutions for problems associated with global environment and energy consumption have become a major focus. Expectations for a shift from vehicles using internal combustion engines (ICEs), which consume a lot of energy and emit CO₂, to eco-friendly electric vehicles, is increasing. For electric vehicles to gain momentum, the development and broad utilization of compact and long-life batteries, batteries with fast-charging capabilities and a large number of charging stations are expected; however, the shift to electric vehicles without internal combustion engines that consume fossil fuel will continue to take place.

EVs can incorporate new functions and features which have been impractical for conventional vehicles with internal combustion engines, thus a new vehicle community is about to be created. In many cases, vehicles which utilize fossil fuel have their internal combustion engines placed in the front or back of the vehicles, and the energy produced by ICEs is transmitted to the wheels through the transmission and drive train. This arrangement prevented freedom of design in the placement of the different components.

On the other hand, since EVs use generators to produce electric power, the driving force can be obtained without the need of a mechanical transmission, depending on the design of the motors and controllers. In addition, with in-wheel motors where the motors are installed inside the hubs, (i.e. a motor is placed in each wheel) power can be produced by multiple distributed motors, which significantly increases the freedom of vehicle layout design.

Furthermore, EVs have higher torque responsiveness than ICEs and are capable of producing any desired torque in positive or negative rotation ranges by controlling the motors. The technology to regenerate, store and reuse the motion and potential energy of vehicles is impractical to incorporate with conventional ICEs. By introducing a drive system utilizing multiple motors, the driving power can be more precisely controlled in order to enable vehicle attitude control and stable driving.

By combining new control systems, such as a high response control system for motor torque, a steer-by-wire system and various sensors, it is possible to create vehicles with higher performance and functionality. By adopting car navigation systems, cameras, radars, etc., the robotization of automobiles

that enables safer transportation is about to begin.

For EVs to gain popularity, the development of compact and high-efficiency motors, the achievement of higher efficiency in drive circuits such as inverters and converters and the development of low-cost batteries with high capacity, long life and low loss, capable of high speed input/output of large currents, is required. Permanent magnet synchronous motors (PMSM) that use rare earth magnets such as NdFeB magnets are often used as the motors for driving power.

However, for manufacturing cost reduction and to ensure a stable supply, the use of induction motors (IM) and switched reluctance motors (SRM) that do not use rare earth magnets is expected to increase.

For EVs, the battery voltage can be 200V or more, the drive voltage of the main drive motors can be 500V or more and the output of the motors can be 100kW or more. For drive circuits, low-loss power elements that can be used under high voltage and high currents are required.

In particular, low-loss power devices allow the cooling structure of inverters to be changed from water cooling to air cooling, which contributes to a compact size and low cost, as well as the efficient use of electricity. Heat radiation design and measures against heat are essential. Also, drive methods, control circuits and implementation technologies for simplifying heat radiation systems are required. To achieve these methods, higher performance of power devices and efficiency in controlling methods are required, as well as the technology development of control systems for more efficient energy regeneration and storage of regenerated energy. It is also important to develop measures against noise emitted from the inverters and converters to protect the electronic data.

In this paper, the current state and future technologies such as recent motor control technology, properties of various motors, application technologies for inverters and converters, sensor-less control methods and issues associated with leakage currents due to motorization are described.

2. Recent control technologies

2.1 Higher efficiency of ICEs

Whether powered by ICEs or electric motors, completely new vehicles are required to be highly energy efficient and environmentally friendly with low emissions.

ICEs for automobiles are now being equipped with control systems using advanced controls and motors for the purpose of making the ICEs highly efficient and environmentally friendly.

In order to achieve compact, lightweight and highly efficient ICEs, the turbo charger, which is a device that supplies a compressed mixture of fuel and air or compressed air into the cylinders, is coming into the spotlight. This device uses exhaust gas from the internal combustion engine to turn a turbine to drive compressors in order to create compression. However, at lower rotation speeds, sufficient charging is not available, resulting in a delayed response called turbo lag.

Currently, charging systems called electrically assisted turbo chargers or super chargers, which have fast responses even at lower rotation speeds, are being developed by combining recent electronic control technology and high performance motors¹⁾⁻⁵⁾. The electric super charger system is composed of a compressor and motor to easily control the charging pressure and capacity without depending on the exhaust pressure from the internal combustion engine, which contributes to a faster response.

These devices often use permanent magnet synchronous motors (PMSM) driven at 100,000 – 200,000 rotations/min. To achieve these high speed rotations, the motor drive frequency can reach several kHz. Therefore, reduction of motor winding electric time constants, improvement of power density and small form factors, and creating inverter systems that enable precise power control are required. Mechanical components, such as bearings for high speed rotation that can withstand vibration and high temperatures must also be developed.

The motors used for electrically assisted turbo chargers and super chargers are required to be driven at high efficiency and controlled with precise identification of the magnetic pole positions of the rotor. Resolvers are often used for detecting the magnetic pole positions, which makes the motor system size, as well as the detection circuits and detection wiring, increase, resulting in higher costs. Consequently, systems to accurately estimate the magnetic pole positions without using rotor position sensors are needed.

Fig. 1 shows the transient analysis result of a 1.4 liter gas engine to reach the target torque. As shown in the figure, the rise time can be shortened by 35% compared with conventional turbo chargers using exhaust gas.

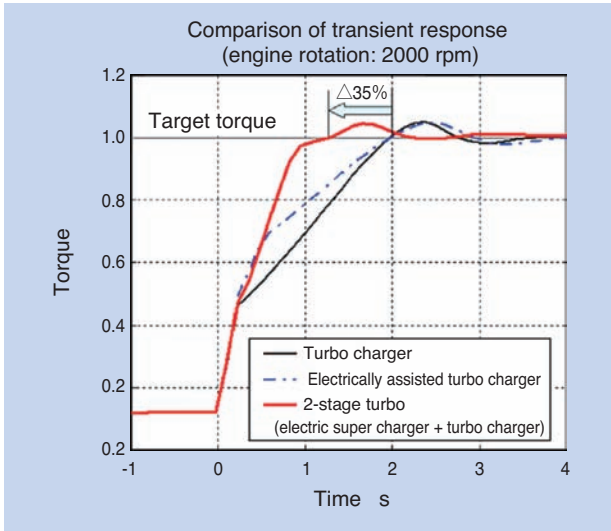


Fig. 1 Example of transient response of internal combustion engine³⁾

Source: Yukio Yamashita, Seiichi Ibaraki, et al., Development of Electric Supercharger. Contributing to the Downsizing of Automobile Engine, Mitsubishi Heavy Industries Technical Review, Vol. 47 No.4, pp.12-17 (2010) Fig. 3.

2.2 Properties required for motors of automobiles

The motors used in automobiles are required to operate from below -40 to +85°C indoors and from below -40 to +120°C in engine rooms (in some cases, +150°C or more). In addition, motors positioned in places other than the cabin must have a structure that avoids any problems caused by the adhesion of iron sand contained in dust and sand. Furthermore, high speed response is also required along with the improvement of the control performance.

For auxiliary motors, low-cost brushed DC motors (DCM) with simple control circuits are often used.

In applications where compactness, long-life and low noise are required or high efficiency is required, permanent magnet synchronous motors (PMSM) are used.

Motors used as the main engine of electric vehicles are required to have various rotation speed/torque properties depending on the driving conditions such as low speed/high torque application where start/stop operations are frequently repeated, driving on flat terrain or climbing slopes and driving on highways. Motors for main engines operate in four quadrants, as shown in Fig. 2. When moving forward, the direction of rotation (forward direction) and torque are both positive and the motor is used in the motoring mode where the electrical energy is converted to mechanical energy. When decelerated, the direction of rotation is positive, however, torque is negative, resulting in the generative mode where the mechanical energy is converted into electrical energy. Moving in reverse, the direction of rotation and torque are simply reversed, where both

motoring and regeneration modes are used in a manner similar to moving forward. In the motoring mode, the inverter transmits the electrical energy from the battery to the motor and in the regenerative mode, the motor operates in generative mode, transmitting kinetic energy from the motor to the battery. Therefore, the converter, which controls the motor drive voltage, needs to convert electric power in both directions.

Fig. 3 shows the rotation speed - torque characteristics required for the main driving motor. In the case of automobiles, the motor is used in the whole region surrounded by the line. Therefore, the motors for the main engine are required to have the following properties.

(1) Compact and lightweight

The weight of the motor increases the rolling friction between the tires and the road surface and climbing torque on slopes; therefore, light weight is an important factor. In addition, a structure to quickly radiate joule heat produced inside the motor due to copper loss and iron loss is indispensable.

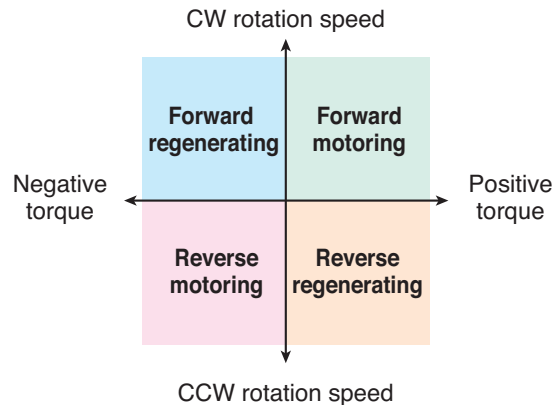


Fig. 2 Motor condition quadrants

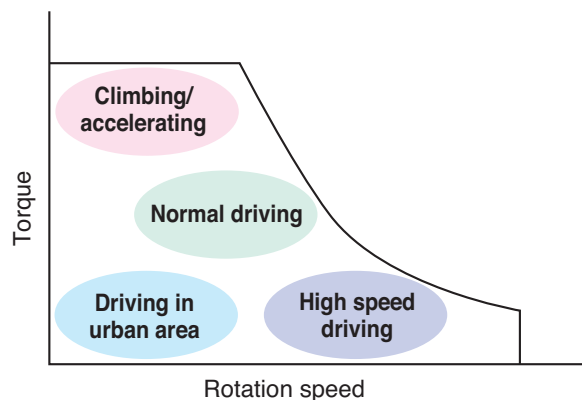


Fig. 3 Demanded characteristics of main driving motor

(2) Large power density

There is an increase in the maximum output power of the motors. It is feasible by increasing the maximum torque and rotation speed. However, to increase the rotation speed, there are still many challenges such as increasing the mechanical strength of the rotor, development of bearings capable of high speed rotation and the reduction of the electric time constant of the inverters and motors that can support motor drive frequencies of several kHz.

(3) High efficiency

Since the EVs are powered by batteries, the travel distance from the stored energy is an issue. Losses with motors are broadly classified into machine loss, iron loss and copper loss. Machine loss comes from loss from winding and bearing loss of the rotor. Iron loss is a loss in the magnetic circuit and can be reduced by selection of magnetic steel sheets and configuration of magnetic circuits. Copper loss is the joule loss from winding resistance and currents, and can be reduced by reducing the winding resistance. Since the copper loss is proportional to the square of the current, loss reduction is more effective when the drive voltage is increased and the current is reduced to obtain the same power output. In this case, the configuration of drive circuits and measures against leak currents will become critical technical challenges, as will be mentioned later.

2.3 Types and characteristics of main drive motors

The main drive motor for EVs is used with the direct current from the battery. Motors with the least consumable parts are used here. They are mainly induction motors (IM), permanent magnet synchronous motor (PMSM), synchronous reluctance motor (SyRM) and switched reluctance motors (SRM). In Japan, permanent magnet synchronous motors (PMSM) driven by 3-phase power are generally used.

These motors are expected to be compact, lightweight and capable of producing high power output in order to attain longer travel distance, with low vibration and low noise. A wide range of rotation speed must be supported from standstill to high speed driving, and high efficiency is desired for effective use of the battery power.

2.3.1 Induction motor (IM)

Induction motors are relatively inexpensive and robust, and highly efficient control by vector control is also available. In addition, since permanent magnets are not used, they are less susceptible to the operating environment. However, since the rotor includes windings, the cooling systems to radiate joule heat are difficult to build. In addition, mechanical structures to

prevent the windings from ejecting out due to centrifugal force during high speed rotation will be required.

These types of motors are expected to exhibit high efficiency when driven at constant high speed for a long distance; however, efficiency drops with repetitive starts and stops over short distances.

2.3.2 Permanent magnet synchronous motor (PMSM)

There are two types: the surface magnet (SPMSM) type, where the magnets are mounted on the surface of the rotor, and the interior magnet (IPMSM) type, where the magnet is embedded inside the rotor. For the main drive application, IPMSM, which can use magnet torque and reluctance torque, is widely used. There are two types of windings, distributed or concentrated and the distributed winding is used for the effective utilization of field weakening. It is widely used as the main drive motor for EVs and hybrid vehicles since it has high efficiency, even in the application of repetitive starts and stops over short distances.

Vector control can be used for field weakening to achieve high speed rotation; however, efficiency is reduced.

Also, since the coercive force of rare earth magnets such as NdFeB magnets decreases at high temperatures, resulting in demagnetization and reduction in the magnetic force, care should be taken in limiting the operating temperatures.

IPMSM has the following properties, compared with SPMSM.

- (a) Since the permanent magnets are embedded inside the rotators, cracking and scattering of magnets due to high speed rotation is unlikely.
- (b) SPMSM requires the permanent magnet to be processed in an arch whereas IPMSM can use plate-shaped magnets, resulting in manufacturing cost reduction.
- (c) As both torques from the magnet and reluctance can be used, high torque is achieved.
- (d) Taking advantage of rotor saliency, the position sensor-less control system can be easily configured.
- (e) Leakage flux may be generated at the end of the magnet.
- (f) As the q-axis inductance is large, q-axis armature reaction is large, likely to be affected by the increase of terminal voltage and magnetic saturation.

2.3.3 IPMSM capable of highly efficient control

When the **d**-axis current of IPMSM is set as i_d , the **q**-axis current as i_q , effective value of phase current as I_e , and the current phase as β , then the following relations can be found:

$$I_a = \sqrt{i_q^2 + i_d^2} = \sqrt{3} I_e$$

$$i_d = -I_a \sin(\beta)$$

$$i_q = I_a \cos(\beta)$$

The torque from the permanent magnets of IPMSM, T_m can be obtained from the following equation when the number of pole pairs is set as p :

$$T_m = p \times \Psi_a \times i_q = p \times \Psi_a \times I_a \cos(\beta)$$

On the other hand, torque from reluctance T_r can be obtained by the following equation when the number of pole pairs is p :

$$T_r = p (L_d - L_q) \times i_d \times i_q = \frac{p}{2} (L_d - L_q) \times I_a^2 \times \sin(2\beta)$$

where, Ψ_e is the effective value of the interlinkage flux of one phase of the permanent magnets: $\Psi_a = \sqrt{3} \Psi_e$.

The overall torque of IPMSM, T is the sum of the torque from the permanent magnets T_m and torque from reluctance T_r :

$$\begin{aligned} T &= T_m + T_r \\ &= p \times \Psi_a \times i_q + p(L_d - L_q) \times i_d \times i_q \\ &= p \times \Psi_a \times I_a \cos(\beta) + \frac{p}{2} (L_d - L_q) \times I_a^2 \times \sin(2\beta) \end{aligned}$$

Since the torque from the permanent magnets T_m can be expressed as

$$T_m = p \times \Psi_a \times I_a \cos(\beta)$$

the maximum torque from the permanent magnets is obtained when the current phase $\beta = 0$ degrees. On the other hand, torque from reluctance T_r can be obtained by the following equation when the number of pole pairs is p :

$$T_r = \frac{p}{2} \times (L_d - L_q) \times I_a^2 \times \sin(2\beta)$$

Therefore, the current phase β for the reluctance torque T_r becomes the maximum at either 45 or -135 degrees.

Hence, the current phase β that creates the overall torque of IPMSM, is in the range of 0 - 45 degrees. Also, since the torque from the permanent magnets T_m is proportional to the current and the torque from the reluctance, T_r is proportional to the square of the current, and the current phase β increases as current I_a increases. IPMSM is characterized by the controllability of the maximum torque by controlling the current phase β .

When the **d**-axis current i_d is controlled to be always set to 0, the motor generated torque T is proportional to the **q**-axis current i_q as shown in the following equation:

$$T = p \times \Psi_a \times i_q = p \times \Psi_a \times I_a$$

provided, $I_a = i_q$.

With SPMSM, since the **d**-axis current is 0, the supplied current for the same torque will become the minimum, resulting in high efficiency. On the other hand, with IPMSM, since the reluctance torque T_r cannot be used, the control system must be built with special consideration.

With IPMSM, current phase β that maximizes the motor generated torque T exists. That is, it is possible to generate torque most efficiently for the current I_a . The current phase I_a to obtain the maximum torque can be expressed in the following equation:

$$\beta = \sin^{-1} \left(\frac{-\Psi_a + \sqrt{\Psi_a^2 + 8(L_q - L_d)^2 \times I_a^2}}{4(L_q - L_d) \times I_a} \right)$$

The **d**-axis current i_d and the **q**-axis current i_q in this equation are as follows:

$$i_d = -I_a \sin(\beta)$$

$$i_q = I_a \cos(\beta)$$

Highly efficient motor control can be achieved by obtaining the current phase β for the motor current I_a and controlling the **d**-axis current i_d and the **q**-axis current i_q of IPMSM.

2.3.4 Synchronous reluctance motor (SyRM) and switched reluctance motor (SRM)

SyRM and SRM both use reluctance torque, not permanent magnets. With SyRM, the rotor is driven by the rotating magnetic field created by the windings, similar to inductance motors and permanent magnet synchronous motors, while the method of SRM drives the rotor by providing currents to the windings applying switched voltages. It is necessary to drive these motors by detecting or estimating the rotor position in order to gain an efficient reluctance torque.

The position sensor-less driving method of SRM will be described later.

Since these motors do not use permanent magnets and the rotors are made of iron core, their application is expected to increase. In addition, the traditional issues of vibration and noise associated with SRM are being addressed in recent research with development of structures with lower vibration and noise, for broader implementation.

2.4 In-wheel motor

In-wheel motors are the built-in motors within the wheels, with the direct drive method which drives the tires directly by motors, and the reducer method, which incorporates gear speed reducers within the motors.

They use multi-pole permanent magnet synchronous motors (PMSM), and outer-rotor type and pancake type are used to obtain large torque with the direct drive method and inner rotor type is also used with the reducer method.

Even if the reducer method requires an increased number of reducer components, since it can easily gain high torque, compact and lightweight motors can be achieved. The mechanical design using in-wheel motors is significantly different from the on-board method using differential gears and transmission, increasing the degree of freedom in the vehicle design.

With the in-wheel motor method, each wheel can be independently and precisely controlled, significantly enhancing driving stability and performance⁶⁾⁻¹⁰⁾.

However, the increased unsprung weight below the suspension may adversely affect the comfort level of passengers due to lower suspension responsiveness. Therefore, vehicle systems design must be made precisely.

In addition, the cooling system to radiate the heat from copper loss and iron loss of motor windings applied to each wheel is a critical technology.

2.5 Converter and inverter

The power source of the main drive motor is DC power from the battery. A converter is a device that transforms DC voltage to any desired DC voltage, and an inverter is a device that creates AC voltage from DC voltage. The converter is required to supply electric power from the battery to the inverter and motor in the motoring mode and convert kinetic energy to electric energy and store it in the battery in the regenerating mode. Therefore, the converter is required to have the capability to flow the current in both directions. Those converters are called bidirectional step-up/down DC-DC converters and used in the power supply circuits of EVs.

The DC-DC converters with electric coupling between the input-side power supply and output-side power supply are called non-insulated type. In this type, in general, the ground is commonly used as shown in Fig. 4 (a). On the other hand, the insulated type provides no DC coupling between the input-side power supply and output-side power supply using a transformer in between. The voltage obtained from the transformer is converted to DC voltage through the rectifier for output. The selection of type depends on the circuit type used; however, the insulated type is more effective for suppressing diffusion of noise.

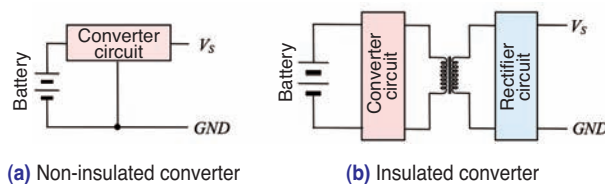


Fig. 4 Non-insulated and insulated converters

2.5.1 Non-insulated type bidirectional converter

In general, it is configured with circuits with a common ground and is capable of transmitting power in both directions. Fig. 5 shows a non-insulated bidirectional converter circuit using MOSFET (surrounded by dotted line) and an inverter circuit. This circuit is able to create the voltage supplied to the inverter, by stepping up the DC supply voltage from the battery.

In this case, MOSFET1 remains OFF and the duty ratio of the ON/OFF switch for MOSFET2 is controlled so that the terminal voltage V_c of the capacitor C , is set at the specified voltage.

On the other hand, when the regenerative energy is generated, the current (charge) is supplied to the capacitor C through the inverter, to increase the

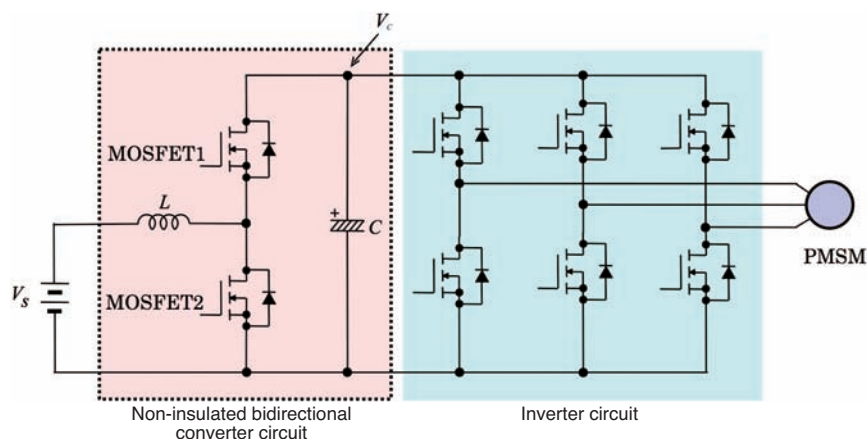


Fig. 5 Non-insulated bi-directional converter and inverter circuits designed with MOSFETs

terminal voltage of the capacitor V_c . The control circuit controls the capacitor voltage V_c , and when the voltage exceeds the specified voltage, it adjusts the duty ratio of the ON/OFF switch of MOSFET1 to allow the energy stored in capacitor C to be appropriately stored in the battery.

2.5.2 Insulated type bidirectional converter

The insulated type bidirectional converter has its input/output terminals decoupled from the DC standpoint but is able to control bidirectional transmission of power. Fig. 6 shows an example of an insulated type bidirectional converter circuit capable of stepping up/down the voltage. The following is the mechanism of power transmission.

(1) Transmitting power from V_1 to V_4

(i) In the case of $V_1 > V_4$

S1, S2, S7, S8, S9, S10 and S12 are all turned OFF. S3 and S6, as well as S4 and S5 are alternately switched ON/OFF at the duty ratio of 50%. The voltage V_2 and V_3 will become close to voltage V_1 . S11 is PWM controlled so that the output voltage V_4 becomes the specified voltage.

(ii) In the case of $V_1 < V_4$

S1, S7, S8, S9, S10 and S12 are all turned OFF. S3 and S6, as well as S4 and S5 are alternately switched ON/OFF at the duty ratio of 50%. S11 remains ON. S2 is PWM controlled so that voltage V_4 becomes the desired output voltage. Voltage V_2 and V_3 will become higher than voltage V_1 .

(2) Transmitting power from V_4 to V_1

(i) In the case of $V_4 > V_1$

S2, S3, S4, S5, S6, S11 and S12 are all turned OFF. S7 and S10, as well as S8 and S9 are alternately switched ON/OFF at the duty ratio of 50%. S1 is PWM controlled so that the regenerative current (current from V_4) or current supplied to the battery (charging current) becomes the specified value.

(ii) In the case of $V_4 < V_1$

S2, S3, S4, S5, S6 and S11 are all turned OFF. S7 and S10, as well as S8 and S9 are alternately switched ON/OFF at the duty ratio of 50%. S1 remains ON. S12

is PWM controlled so that the regenerative current (current from V_4) or current supplied to the battery (charging current) becomes the specified value.

2.5.3 Inverter

Inverters are the circuits to generate AC voltage from DC voltage. Three-phase permanent magnet synchronous motors are usually used for vehicles, because of the gains in efficiency. The basic circuit configuration of the three-phase inverters consists of 6 power devices, as Fig. 7 shows, and each power device is controlled by switching. The wiring depicted with bold lines in the figure carries large currents. Wiring is implemented using copper bars, etc. to reduce the impact of inductance.

Inverters control power devices with PWM to supply sinusoidal current to the motor windings by switching. The higher the switching frequency (PWM frequency), the more the reduction of motor magnetic noise and current ripples can be achieved. As the switching loss of power devices is proportional to PWM frequency, the vehicle systems use a frequency of 5-10 kHz.

Currently, IGBT based on silicon (Si) is widely used as power devices for vehicle drive systems; however, PWM frequency, circuit configuration, radiation method, etc. are expected to change significantly, when devices using silicon carbide (SiC) and gallium nitride (GaN) emerge.

For the main drive motor of vehicles, permanent magnet synchronous motors of 50-100 kW are used and the voltage of approx. 500V is used for

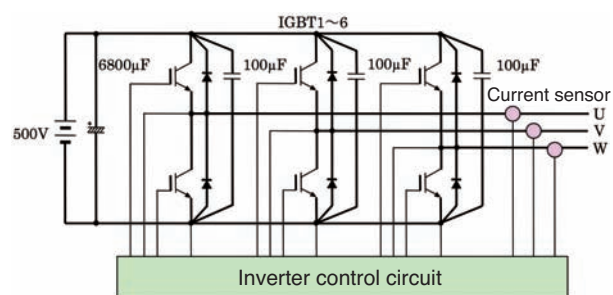


Fig. 7 Three-phase inverter circuit

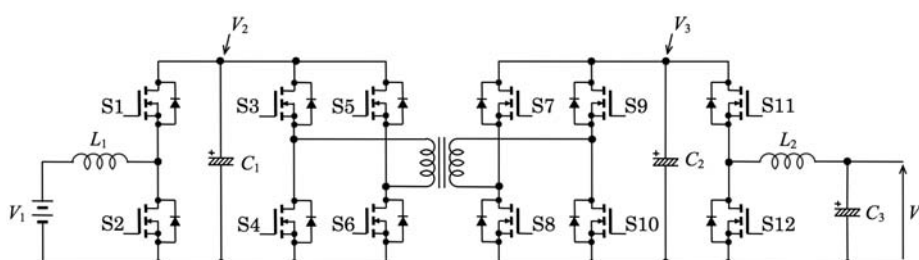


Fig. 6 Insulated bi-directional step up & down converter circuit

compactness and high efficiency, supplying large currents. The motor voltage is expected to increase further along with the development of power devices. Therefore, ingenuity in design is needed to maintain the insulation of the wiring and providing thicker wiring (bus) to avoid the impact from inductance, as well as reducing the inductance. In general, copper bars are frequently used to configure the wiring. Also, capacitors of approx. several 100 μF with good high frequency characteristics (devices with small ESR and ESL, such as ceramic capacitors) need to be inserted between power supplies into each arm of the inverter in order to reduce the noise due to switching.

Since the power source voltage supplied to inverters has large fluctuations, a control system with fast response is required to obtain the specified motor torque even with the voltage fluctuation. Also, a small form factor is required for installation in the vehicles, with special consideration on the configuration of the cooling system.

For selecting power devices, it is required to consider sufficient capabilities for supply voltage and motor drive current. The devices are required to have small switching losses at high PWM frequencies, as well. In addition, inverter control circuits for driving the devices in high speed are also required.

2.6 Leakage current of vehicles

Permanent magnet synchronous motors (PMSM) of 50-100 kW are used as the main drive motor and power is supplied to the motor with bidirectional step up/down DC/DC converters and inverters. Recently, the supply voltage to inverters has been stepped up from the battery voltage of approx. 200 V to approx. 500 V, to reduce the drive current.

As shown in Fig. 8, the windings of PMSM are wound on the iron core, with insulation in between. Fig (a) shows distributed windings and (b) indicates concentrated windings. The motor is installed on the

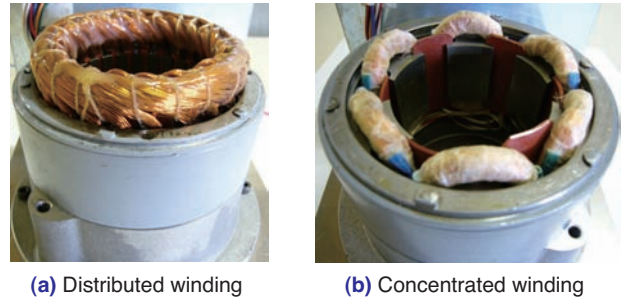


Fig. 8 PMSM windings

conductive vehicle body and capacitance is present between the windings and the motor enclosure.

The inverter controls power by PWM control (switching control) to supply adequate current to PMSM based on the torque command. The power device in the drive circuit provides high frequency switching. The stray impedance between the power supply and the load connected with the inverter and vehicle body is the main cause of electromagnetic noise and leakage current.

Fig. 9 shows the stray impedance in the motor drive circuit. In the figure, C_{f1} to C_{f5} indicate examples of stray capacitance, L_{f1} and L_{f2} indicate examples of stray inductance. Stray capacitance produces leakage current and diffuses noise when the voltage changes quickly. On the other hand, stray inductance produces high voltage when the current changes quickly, which may destroy the device. Transient voltage and leakage current due to stray inductance and capacitance produce noise.

Since motors have stray capacitance between the windings and the motor enclosure, leakage currents are produced inside the motor enclosure when PWM voltage is applied to the motor windings as it acts on the stray capacitance, etc. that exists in electronic circuits such as batteries and inverters.

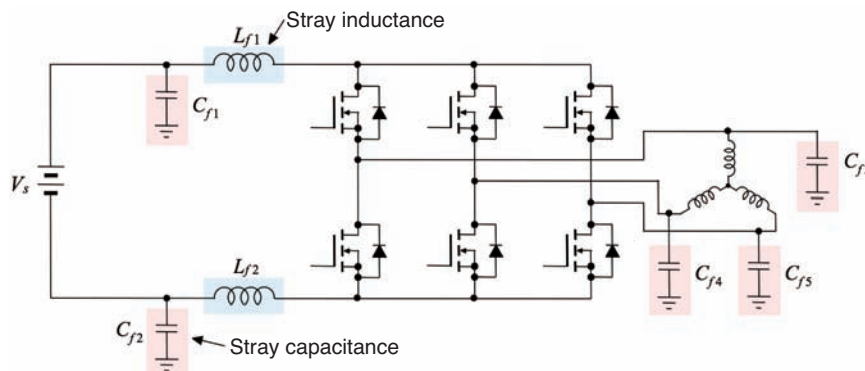


Fig. 9 Stray impedance of inverter circuit and motor

3. Switched reluctance motor (SRM) to achieve high speed rotation

3.1 Characteristics and rotor position estimation methods

The switched reluctance motors (SRM) have a simple structure not requiring permanent magnets, therefore, they are suitable for driving at high speed or under high temperatures¹¹⁾⁻¹²⁾. In order to operate SRM at variable speeds, it is necessary to obtain the rotor position information similar to permanent magnet synchronous motors. However, most rotor position detection devices that are used in general industry fields, such as encoders and Hall effect sensors, are not suited for severe environments such as vehicle use. Several methods are proposed such as estimating the angles from driving voltage/current, taking advantage of the rotor rotation angle dependency properties of SRM winding inductance, and obtaining the angles from the change in inductance by superimposing the high frequency voltage on the driving voltage, etc.¹³⁾⁻¹⁶⁾.

There are other methods of estimating the rotor position such as using observer or analytical models to estimate the rotor positions from multiple parameters not in linear relation with the rotor position, using some kind of artificial intelligence, or applying signals other than the driving voltage on the motor windings, etc.¹⁷⁾⁻¹⁹⁾.

In this section, two methods of estimating the rotor positions not affected by driving voltage and current are proposed, when the windings are driven by PWM.

3.2 Rotor position estimation method I

The proposed sensor-less SRM driving method provides leader lines at the connection points of the opposing serially connected windings as a driving terminal and high frequency signal terminal, and is used for the injection and detection of signals. **Fig. 10** shows a part of the connection diagram when this proposal is applied to a 4-pole 6-slot SRM. It shows the cross section of the rotor having the salient poles in the center. 6 windings from L_1 to L_6 are placed as the stators. It shows the availability of leader point T in the connection of windings L_1 and L_4 . The same wiring applies to the remaining two pairs of windings.

The symmetric properties, when the SRM is regarded as a transformer from this connection, can be applied to reduce the interference of high frequency signals and driving voltage. In addition, the accuracy of the detection can be increased by reducing the interference of the driving voltage to the detection circuit, by inserting a differential mode choke transformer into the circuit where high frequency signals are injected/detected.

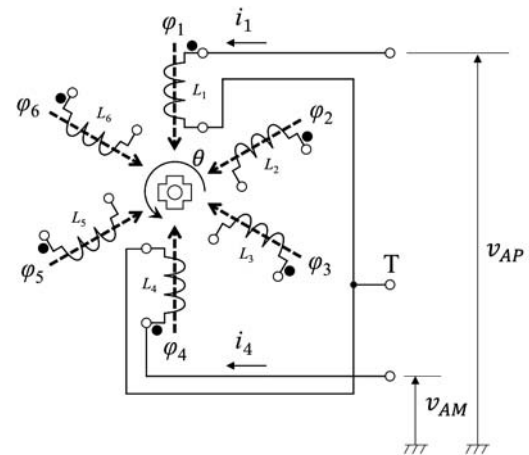


Fig. 10 Wire connections of SRM

3.2.1 Rotor position detection method

Fig. 11 shows a rotor position detection circuit that is not affected by PWM voltage and winding current, driven by a circuit with a common mode network (CMN)²⁰⁾. **Fig. (a)** is a high frequency injection circuit, and **(b)** is a detection circuit for high frequency signal injected into a different phase. When the phase, where the high frequency is injected, is aligned with the teeth of the stator, the high frequency signal levels in the other two phases match. By injecting high frequency waves into only one phase, the rotor position is detected based on the high frequency detection signals obtained from the other two phases, and when the alignment is detected, the phase where the high frequency is injected is switched and the above operation is repeated. This is how the rotor position is detected. **Fig. 12** shows equivalent circuits shown in **Fig. 11** for the high frequency signal and common mode signal detection circuits. In the case of high frequency signals, the circuit impedance is 0 and the amplitude of the detection signal can become large. On the other hand, in the case of differential mode signals, the circuit impedance is high and the output signal becomes small.

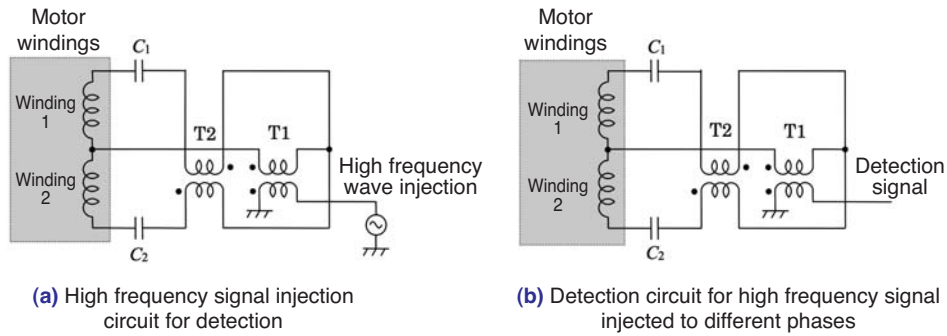


Fig. 11 Rotor position detecting circuit with CMN

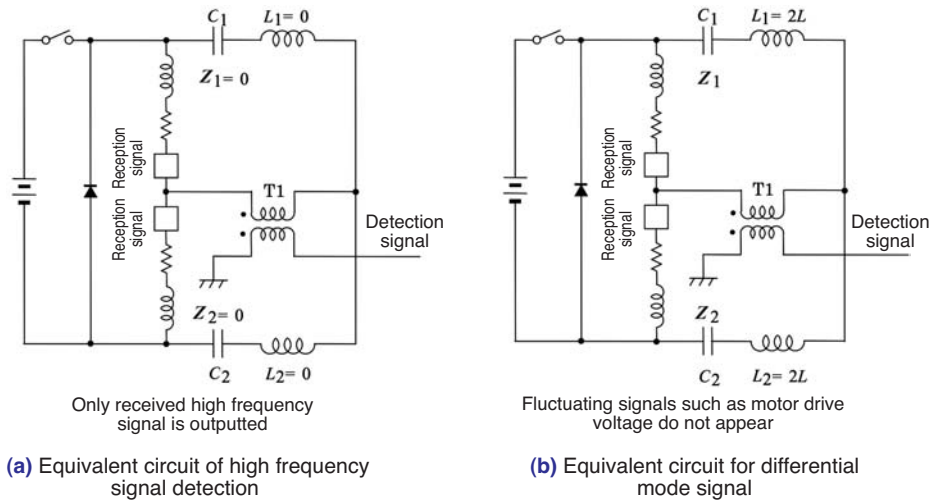


Fig. 12 Equivalent circuits for the high-frequency signal and differential mode signal detection circuits

3.2.2 Example of implementation

Fig. 13 shows an example of implementing the proposed sensor-less rotor position detection method. In the figure, OSC is an oscillator, CTL is a control circuit and DET is the detection circuit. The detection circuit detects the amplitude of waveforms using the general envelope detection or product detection circuits, etc. The control circuit CTL selects a CMN to inject signals into by controlling the switch group, detects the timing for commutation by examining the amplitude detected from the other phases and notifies the power circuit. Fig. 14 shows the measurement results of self-inductance to the rotor angle.

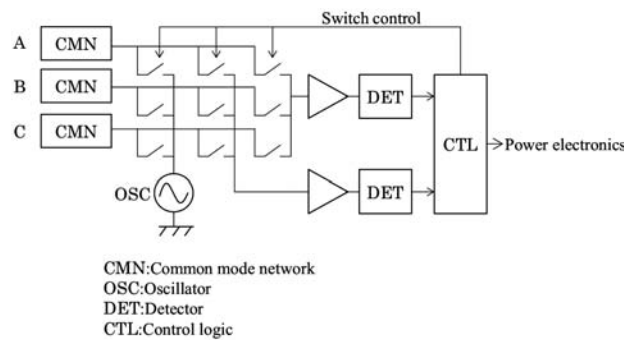


Fig. 13 Proposed sensor-less rotor position detecting method

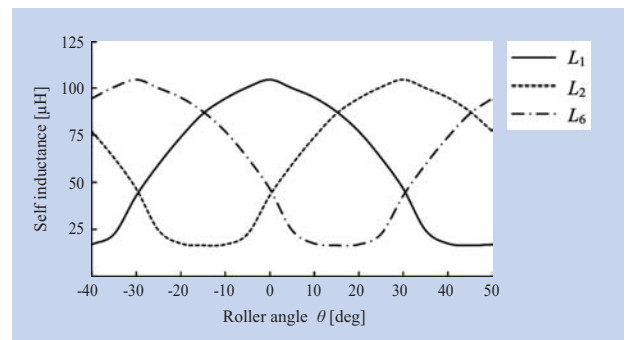


Fig. 14 Relation of self inductance to rotor angle

3.2.3 Experiment results

Fig. 15 shows the waveforms from the experiment at $10,000 \text{ min}^{-1}$ of rotating speed with no load. They are, starting from above, the output waveform of the Hall effect sensor installed for monitoring the rotor position, the A-phase current and overlapping B-phase detection waveform v_{DB} and the C-phase detection waveform v_{DC} . The Hall effect sensor generates 4-period pulses per rotation. In the experiment, advance control is applied to compensate for the delay of current phases.

Fig. 16 shows waveforms of the experiment at $100,000 \text{ min}^{-1}$ with no load. In the experiment, the rotating speed was controlled by monitoring the Hall effect sensor waveform and adjusting the DC rail voltage to obtain the specified rotating speed. However, the control of the rotating speed can be automatically adjusted.

We have confirmed that the sensor-less rotor position control can drive the motor at $200,000 \text{ min}^{-1}$ or

more of rotating speed by adjusting the timing of commutation (advancing) in the experiment.

In addition, this method is applicable for the rotor position detection of the motors where the inductance changes depending on the rotor position such as IPMSM.

This method provides a relatively easy detection of the rotor position; however, magnetic saturation at the stators can affect the mutual inductance which prevents the correct detection of position. Therefore, further study is required.

3.3 Rotor position estimation method II

The previous section proved that, with SRM, the rotor position can be detected when the inductance of windings is measured. In production systems, motor windings are connected to power circuits such as inverters and driven by PWM. The inductance must be measured while the voltage is applied and currents are carried in the windings.

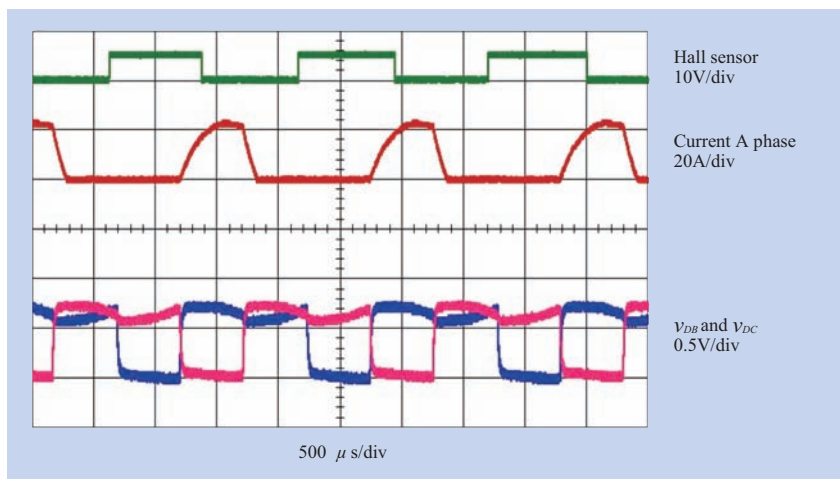


Fig. 15 Waveform at $10,000 \text{ min}^{-1}$

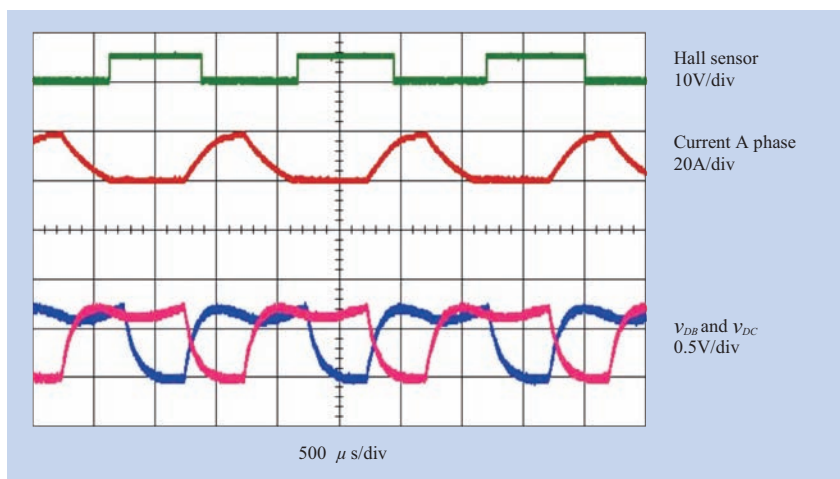


Fig. 16 Waveform at $100,000 \text{ min}^{-1}$

In this section, we propose a new method of measuring the self-inductance of 4-pole 6-slot SRMs that have parallel connections of phase windings, which is not affected by the driving voltage/current, even with magnetic saturation. ²¹⁾⁻²²⁾ Fig. 17 shows the connection and winding inductance measurement circuit for 4-pole 6-slot SRMs. The windings in parallel connection are excited by currents supplied by driving circuits based on the rotor position, and the rotor generates torque.

3.3.1 Equivalent circuit

Fig. 18 shows an equivalent circuit configuration of one winding. In this circuit, two wires that supply current to the two windings in parallel connection are placed through the toroidal core alternately to cancel out the magnetic flux generated by the currents. It is possible to measure the inductance of parallel connection of the two windings L_1 and L_2 , by measuring the impedance of the winding (between Terminals a and b) placed around the toroidal core.

3.3.2 Measurement principle and characteristics

In the circuit of Fig. 17, the terminals A and B are connected to the power circuit that drives the motor and supplied with an agitation current. The current supplied to terminal A runs through winding L_1 and reaches terminal B through the winding on the toroidal core. Similarly, the current runs through winding L_4 . The magnetic fluxes inside the toroidal core are mutually cancelled because the directions of the winding current are different; therefore, windings L_7 and L_8 cannot be seen from the power circuit. If we consider the output impedance of the power circuit as 0, the impedance observed from winding L_9 placed on the toroidal core is the impedance of windings L_1 and

L_4 in parallel connection.

This method is characterized by its ability to detect the rotor's salient pole position regardless of the motor's driving conditions, since the impedance of the motor windings can be observed without any impact from the current supplied from the power circuit by the use of toroidal core.

3.3.3 Rotor position detection method

As shown in the previous section, we have proven that the inductance of each phase of SRM in parallel connection can be measured while the motor is in operation. By using this method, when the inductance of three-phase windings is measured and if the inductance levels of the phases not excited match, then the alignment to maximize the self inductance of the excited phases is occurring. Highly efficient drives can be achieved by appropriately controlling the switching timing of the current rising and falling points by detecting the rotor positions from these conditions and using the estimated rotor position information. This method requires more leader lines; however it is characterized by being able to detect rotor positions without any impact from magnetic saturation.

3.3.4 Summary of this method

We have proposed a method of sensor-less detection of SRM rotor positions and confirmed the operation of this method through simulation, as well as with a test circuit using this method where high speed rotation can be achieved with sensor-less position detection. These methods are characterized by the following:

With estimation method I, no electronic components are required for the motor if an intermediate tap wiring for CMN is added for the number of phases between

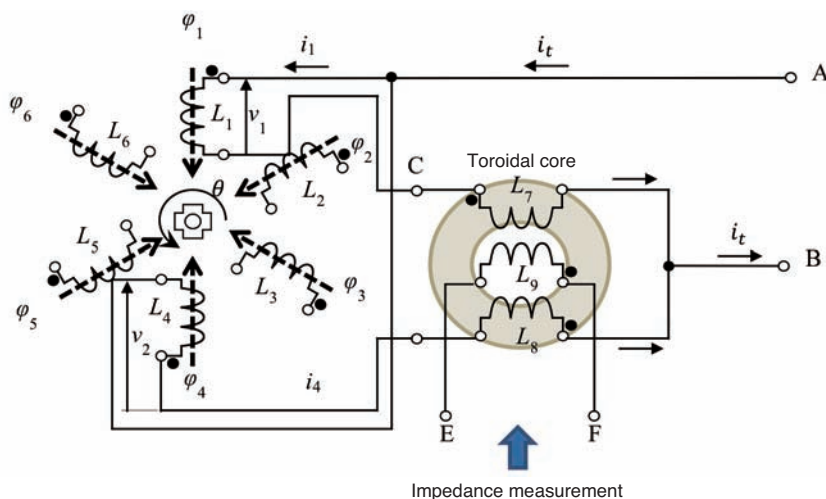


Fig. 17 Impedance measuring circuit

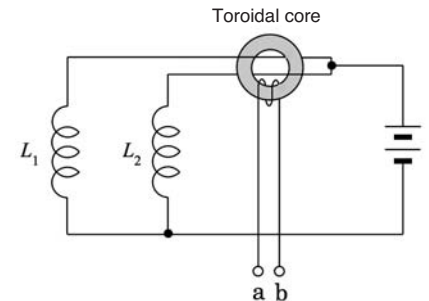


Fig. 18 Impedance measuring principle

the motor and power circuit and CMN is installed in the electronic circuit. Therefore, the rotor position can be estimated under high temperatures while the motor is in operation. In addition, since it is not affected by the winding current, no complex calculation or filter design is required.

Estimation method II requires more leader lines connected to the motor, however, it is a highly practical method since the rotor position can be estimated without any impact from magnetic saturation.

These rotor position detection methods should be suitable for applications where installing magnetic pole position sensors is difficult such as in vehicles.

4. Challenges

Current state and future technologies such as recent motor control technologies, the properties of various motors to be used in vehicles, application technology for inverters and converters, sensor-less control methods and issues associated with leakage currents due to motorization have been described.

Vehicles, not only electric vehicles but also vehicles with internal combustion engines, are making progress in higher efficiency using motors and electronic control technology. Furthermore, in recent years, driver assistance features such as automatic parking systems, pedestrian detection alarms and collision prevention functions are being installed. Safety functions are also being installed due to the progress that has been made. In the future, safer and more friendly automobiles for environment and people will be developed, including autonomous driving, and it is expected that automobiles will be heading in the direction of robotization with high intelligence in both function and performance.

For these automobiles, motors and electronic control are essential systems and critical technology. In addition, since the vehicles are for humans to operate and ride, driving and riding comfort must be emphasized. Informing the driver of the external forces applied to the vehicle and changes in the environment is also important, and various sensors are used for this. Software to comprehensively evaluate these types of information is also necessary.

In order to increase the responsiveness to vehicle motion, it is necessary to reduce the weight of vehicles and increase the control performance.

Reduction of weight can be accomplished with a lighter body, as well as the smaller and lighter main drive motors and heat radiation systems including inverters, batteries, etc.

Smaller and lighter main drive motors are important factors that can be achieved comprehensively, even for

in-wheel motors, by installing reducers. By reducing the unsprung weight, the responsiveness is increased and the comfort is improved. For compactness, high speed rotating motors and reducers that can withstand high speed rotation are required. In addition, as power assisted turbo chargers and superchargers, used for higher efficiency of internal combustion engines, generate pressure by the high speed rotation of turbines, bearings are also required to withstand the high speed rotation. Also, the magnetization of bearings by leakage flux of motor windings and magnets cause the generation of currents during rotation, resulting in electric corrosion and lower product life; therefore, bearings with low magnetization properties are required.

Motors will be used, more than ever, for service robots and vehicles, with increased demands, for which higher efficiency, low vibration/noise and long life will be required. Bearing technology to support these rotational bodies are expected to be a critical element and further development at NTN is highly expected.

References

- 1) Ibaraki, S. et al., Numerical and Experimental Reliability Evaluation of the High Temperature Turbine Wheel for Gasoline Engines, 13th Supercharging Conference (2008)
- 2) Ibaraki, et al., Development of the "hybrid turbo," an electrically assisted turbocharger, Mitsubishi Heavy Industries Technical Review, Vol. 43, No. 3 (2006)
- 3) Yukio Yamashita, Seiichi Ibaraki, et al., Development of Electric Supercharger to Facilitate the Downsizing of Automobile Engines, Mitsubishi Heavy Industries Technical Review, Vol. 47 No.4, pp.12-17 (2010)
- 4) Toshihiko Noguchi, et al., 220,000-r/min, 2-kW Permanent Magnet Motor Drive for Turbocharger, International Power Electronics Conference, IPEC-Niigata (2005)
- 5) Toshihiko Noguchi, Yosuke Takata, Yukio Yamashita, Yoshimi Komatsu, Seiichi Ibaraki, 220000-r/min, 2-kW PM Motor Drive for Turbocharger, IEEJ Transactions on Industry Applications Vol. 125, No. 9, pp. 854-861 (2005)
- 6) Tomoaki Makino, Aiko Ishikawa, Chinami Ito, Kayo Sakai, Recent Technology Trends of In-Wheel Motor System for Automotive, NTN TECHNICAL REVIEW No. 81, pp. 22-29 (2013)
- 7) Yuichi, Itoh, Kayo Sakai, Yusuke Makino, In-Wheel Motor System, NTN TECHNICAL REVIEW No. 79, pp. 22-28 (2011)
- 8) Hiroaki Yoshida, Evolution of In-Wheel Motor System, The Society of Instrument and Control Engineers, 50 (3), 184-188 (2011)
- 9) Satoshi Murata, Development of In-Wheel Motor Drive Unit, Transactions of the Society of Automotive Engineers of Japan, 42 (3), pp. 767-771 (2011)

- 10) Suzuki, Kano, Abe, et al.: "Roll Control Using Tire Longitudinal Forces Integrated with Tire Force Distribution of Full Drive-by-Wire Electric Vehicle", AVEC'14 (2014)
- 11) R. Krishnan, "Switched Reluctance Motor Drives: Modeling, Simulation, Analysis, Design, and Applications", CRC Press (2001)
- 12) Takashi Kenjo, SR Motor, The Nikkan Kogyo Shimibun, Ltd. (2012)
- 13) Mohammad S. Islam, Iqbal Husain, Robert J. Veillette and Celal Batur: "Design and Performance Analysis of Sliding-Mode Observers for Sensor-less Operation of Switched Reluctance Motors", IEEE Transactions on Control Systems Technology, Vol.11, No.3, pp.383-289 (2003)
- 14) Hongwei Gao, Farzad Rajaei Salmasi and Mehrdad Ehsani: "Inductance Model-Based Senseless Control of the Switched Reluctance Motor Drive at Low Speed", IEEE Transactions on Power Electronics, Vol.19, Issue 6, pp.1568-1573 (2004)
- 15) Estanislao Echenique, Juan Dixon, Roberto Crdenas and Ruben Pe a: "Sensorless Control for a Switched Reluctance Wind Generator, Based on Current Slopes and Neural Networks", IEEE Transactions on Industrial Electronics, Vol.56, Issue 3, pp. 817-825 (2009)
- 16) Akitomo Komatsuzaki, Ichiro Miki, A Position Sensorless Control Method for SRM Based on Variation of Phase Inductance, IEEJ Transactions on Industry Applications, Vol 127, No 9, pp. 1023-1029 (2007)
- 17) H. J. Guo, M. Takahashi, T. Watanabe, and O. Ichinokura: "A New Sensorless Drive Method of Switched Reluctance Motors Based on Motor's Magnetic Characteristics", IEEE Transactions on magnetics, Vol. 37, No. 4, pp.2831-2833 (2001)
- 18) E. Afjei, O. Hashemipour, M. M. Nezamabadi and M. A. Saati: "A self-tunable sensorless method for rotor position detection in switched reluctance motor drives", Iranian Journal of Science & Technology, Transaction B, Engineering, Vol.31, No.B3, pp.317-328 (2007)
- 19) Akitomo Komatsuzaki, Tatsunori Bamba, Ichiro Miki, Estimation of Rotor Position in a 3-Phase SRM at Standstill and Low Speeds, IEEJ Transactions on Industry Applications, Vol. 129, No. 3, pp 311-318 (2009)
- 20) Kenji Yamamoto, Hisashi Takahashi, et al., Sensorless Rotor Position Detection for SRMs with Drive Current-isolated Signaling System, IEEJ Transactions on Industry Applications, Vol. 135, No. 5, pp. 521-530 (2015)
- 21) Kenji Yamamoto, Hisashi Takahashi, A study on sensorless rotor position detection of an SRM with phase windings connected in parallel, IEEJ RM-15-97, pp. 57-61, 2015
- 22) Mine Itaba, Naoto Natsuyama, Hisashi Takahashi, Kenji Yamamoto, A method of driving SRM for improved efficiency by means of instantaneous inductance information, IEEJ RM-15-95, pp. 41-46, 2015

<Author biography>

Hisashi Takahashi

**Senior Member, Institute of Electrical Engineers of Japan, Doctor (Engineering),
Professor, Graduate School of Science and Technology, Shizuoka Institute of Science and Technology**

[Specialty]

Electronic Circuit Engineering, Control Engineering, Motor Applications Engineering
(Motor Control, Robot Control, Medical Engineering, Research on Parametric Estimation)

1975	Graduated from Faculty of Electrical Engineering, Polytechnic University, Assistant, then Instructor of Faculty of Electrical Engineering of Polytechnic University, Associate Professor, Electrical Information Specialty, Graduate School of Engineering
1997-1999	Dispatched to Tianjin University of Technology and Education in Tianjin, China as professional in control technology (Long-term Expert) in a National Project.
Since 2000	Member, Program Committee, IEEJ
2001	Special lecture on control technology at the Electrical Electronic Engineering, Nanyang Technological University in Singapore (Short-term Expert)
2003-2007	Member, Technical Committee of Rotational Machines, IEEJ
2003-2005	Chairperson, Investigating R&D Committee for Advanced Technology of Small Motors, IEEJ
2005-2007	Chairperson, Investigating R&D Committee of Performance Improvement and Evaluation Technology by Applications for Small Motors, IEEJ
Since October 2011	Professor, Faculty of Science and Technology and Graduate School of Science and Technology, Shizuoka Institute of Science and Technology
Since 2012	Chairperson, Power Electronics Business Development Program, Hamamatsu Agency for Innovation
Since April 2013	Director of the Yaramaika Education Site, Director of the Yaramaika Innovation Center for Engineering Design and Manufacturing Shizuoka Institute of Science and Technology

Has held many positions such as Academic Society Committee Member, University External Evaluation Committee Member, Subsidy Review Committee Member, etc.

Electrification of the Automobile and Module Products of NTN

Makoto OKASAKA



About 250 years ago, the very first “auto-mobile” started to run in the world, and now, full-scale developments of “autonomous” car are started. On the other hand, the world is facing a serious problem of global warming caused by greenhouse gases mainly CO₂, and each region and country began to move regulation of severe CO₂ emissions, what we call, strict fuel economy regulation to the automobile.

Automobile manufacturers are developing downsized engines as next-generation vehicle and electrification devices for low fuel consumption. This paper introduces modular products by NTN contributing to upgrade of vehicle electrification in various places.

1. Introduction

In 1769, a “self-propelled” vehicle powered by steam engine, “Cugnot’s Wagon”, ran as the world-first automobile in France under King Louis XV’s regimen.

Approximately 250 years since the development of “self-driven” vehicles started, the world is facing a serious problem called global warming. A significant contributor for this problem is said to be greenhouse gasses, mainly consisting of carbon dioxide (CO₂). Countries around the world are working on regulating this CO₂ emission.

CO₂ regulations are particularly strict in Europe (EU), specifying a corporate average CO₂ emissions as 2021 as 95 g/km per company.

This requires more than 38% of fuel efficiency improvement when compared with 2008 efficiency standards. The automobile manufacturers are working on development and promotion of next-generation automobiles. These include hybrid vehicles (HEV/P-HEV) with less CO₂ emission and better fuel efficiency, electric vehicles (EV) and fuel cell vehicles (FCV) with no CO₂ emission, and a shift from the conventional fossil fuel vehicles such as gasoline and diesel engine vehicles.

However, according to the outlook of new passenger vehicle sales in 2050 by the International Energy Agency (IEA) ¹⁾, as shown in Fig. 1, the vehicles only driven by fossil fuels such as gasoline and diesel will decrease to around 10%. The vast

majority will be shifted to the next-generation vehicles with electric motor technology. EVs/FCVs with no CO₂ emission at all are not yet widely spread, with less than half of the total number of vehicles.

In other words, even in 2050, more than half of all the vehicles sold will be using fossil fuel, including HEVs, that emit CO₂.

During this transition, components of automobiles are being developed with electrification in mind, with complete transition to 48V-based technology for improved fuel efficiency. Automobile manufacturers are addressing electrified vehicles for “running”, “turning” and “stopping” with the upcoming transition to self-driving in mind and developing system/module products for that will be important items for future improvement of fuel efficiency.

In this paper, some examples of NTN module products that contribute to the improvement of functions in this transition to electrified vehicles will be introduced.

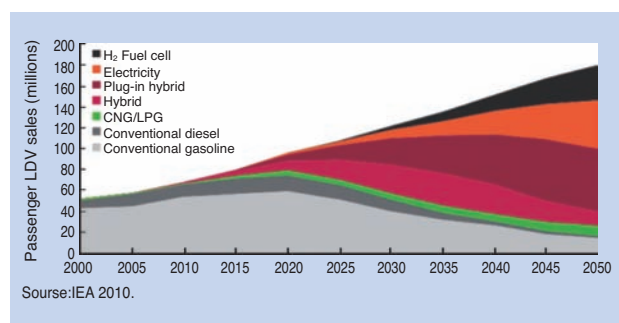


Fig. 1 Annual light-duty vehicle sales by technology type

* Executive Officer, Automotive Business HQ

2. Module/system products addressing electrification of vehicles

NTN has been developing in-wheel motors to replace from internal combustion engines that consume fossil fuel, for reduction of emission of the greenhouse gas CO₂ ²⁾.

In addition, in order to help improve fuel economy of the existing vehicles with internal combustion engines, NTN has been developing and launching electric modular products of operational/control components, since 2004 as shown in Fig. 2, supporting “by wire” technology. These components are based on products such as ball screws, considering that improvement of mechanical efficiency by refined electric control of operational/control components is important for improvement of fuel efficiency.

Furthermore, electric module products and their systems are indispensable for next-generation electric vehicles (EV) and fuel cell vehicles (FCV), which do not use fossil fuel at all. NTN is developing electric module products and system products including their control shown below and in Fig. 3, for improvement of each of the “running”, “turning” and “stopping” functions of vehicles, using demonstration tests with the actual vehicles.

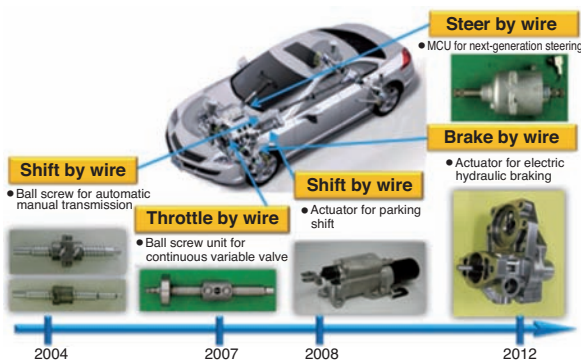


Fig. 2 Electrification with by-wire technology

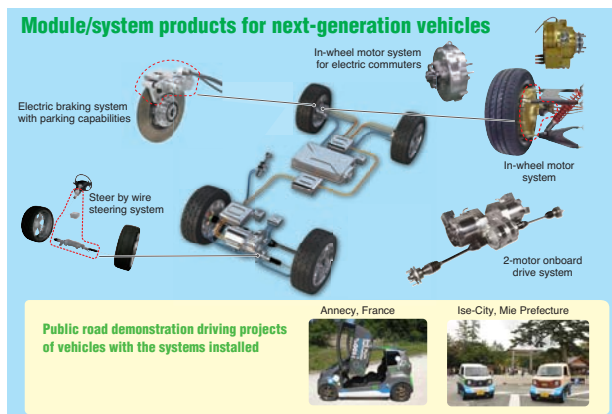


Fig. 3 Modular & system products with electrification for next-gen. vehicles

- For “running”,
 - ... In-wheel motor system
 - ... In-wheel motor system for electric commuters
 - ... 2-motor onboard drive system
 - ... Automatic transmission module/system
- For “turning”,
 - ... Mechanical clutch unit for next-generation steering
 - ... Steer by wire control system
 - ... Rear wheel independent steering system
- For “stopping”,
 - ... Electric braking system with parking mechanism
 - ... Electric hydraulic braking system

3. Addressing next-generation vehicles with electrified modules

The worlds-first automobile, “Cugnot’s Wagon”, collided with a mural the following year, causing the worlds-first vehicle accident.

Approximately 250 years since then, the development of “self-driving” vehicles has greatly accelerated. This was triggered by the development and market introduction of “collision prevention” vehicles that include radars and/or stereo cameras and automatic braking systems.

Since self-driving vehicles control the “running”, “turning” and “stopping” operations, which were conventionally conducted by humans, development of electrified modules/systems is strongly required.

(A) Electrified modules/systems for “running”

The next generation vehicles will “run” with a driving system equipped with multiple motors. NTN is developing in-wheel motor systems and 2-motor onboard drive systems (Fig. 4) as a running system to improve traveling stability of vehicles against many disturbances. These disturbances include braking by unlimited variable control and speed reduction torque for the left/right wheels with independent motors. This development will also improve performance of “turning” by controlling vehicle attitude with torque vectoring from the added torque to the left and right wheels.

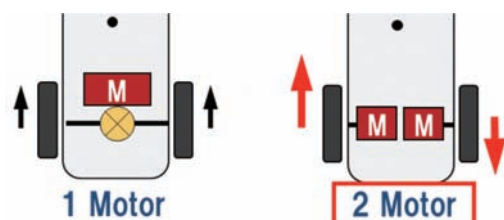


Fig. 4 Torque-vectoring mechanism with 2 motor on board driving system

Vehicles driven by internal combustion engines, that still emit CO₂, and will still account for more than half of the vehicles in 2050 are equipped with transmissions. Transmissions use hydraulic pumps to operate and cause low fuel efficiency. Therefore, the hydraulic mechanisms for operation systems, such as gear shifts, are being replaced by electric shifts.

Large trucks and light passenger cars continue to use gear-based manual transmissions that are characterized by low-cost and high transmission efficiency. However, the use of automatic transmission systems with electrified modules using ball screws in the transmission mechanism is expanding. This change reduces workload of the drivers, particularly for aged drivers.

Continuously variable transmissions (CVT) operate with improved fuel efficiency when compared to a traditional transmission. However the vehicle fuel efficiency of a CVT has been further improved. Fuel loss due to hydraulic pumps that operate pulleys holding the metallic belt is not negligible. Therefore, the CVT pulley driving system using hollow ball screw units is an effective improvement of fuel efficiency for the next-generation CVTs (Fig. 5 and 6).

Some examples include, downsized turbo engines with broad torque band and diesel engines with large absolute torque. Both are widely used due to low fuel consumption, and the efficient transmission of CVT's pinpoint input power is reduced. It is important to

provide coordinated control of both pulleys in the input and output sides with an electrified ball screw unit to achieve more than 95% transmission efficiency ⁴⁾.

(B) Electrified modules/systems for “turning”

The worlds-first steer-by-wire vehicle using an NTN mechanical clutch unit (MCU), shown in Fig. 7, became commercially available in 2014, opening a new chapter of self-driving.

This MCU makes it possible to establish type II steer-by-wire which does not connect steering wheel and tire during normal operation but immediately connects in case of failure, an indispensable module product for self-drive vehicles (Fig. 8).

The next-generation vehicles will evolve from “collision prevention vehicles” to “steering away vehicles”. Type III steer-by-wire is when the vehicle autonomously steers to avoid obstacles.

In other words, the next-generation vehicles will not be equipped with column assist electrified steering, but rack and pinion assist. A downstream assist method will be the main steering method.

NTN has developed a rear wheel independent steering system including toe angle control by proactively steering individual rear wheels to improve vehicle stability during braking and turning (Fig. 9). A new electrified system where the tire geometry in contact with the road is individually controlled will be developed to optimize turning.

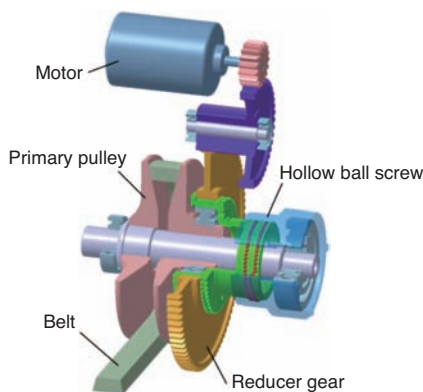


Fig. 5 CVT pulley driving module

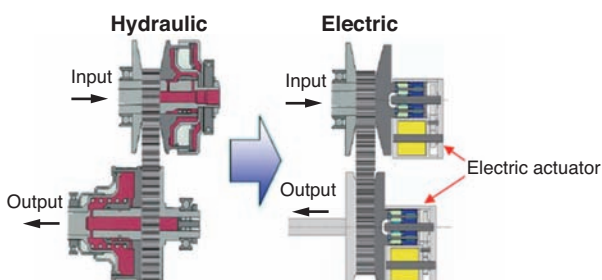


Fig. 6 Electric CVT pulley driving system

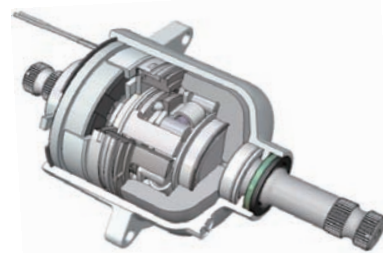


Fig. 7 MCU for steer-by-wire

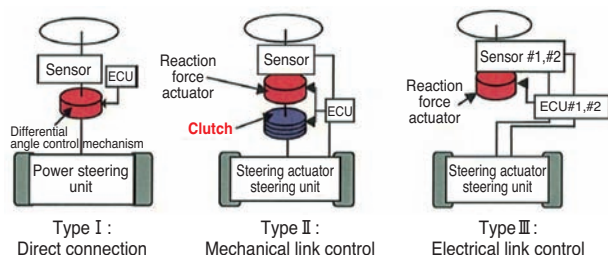


Fig. 8 Steer-by-wire mechanisms

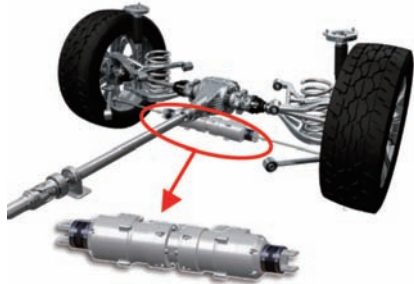


Fig. 9 Rear-wheel independent steering system

(C) Electrified modules/systems for “stopping”

The maximum regeneration of energy during braking was made possible by continuous variable control of braking hydraulic pressure with electric hydraulic braking system using NTN’s ball screws in 2014 (**Fig. 10**).

For “stopping” of next-generation vehicles, electric brakes shown in **Fig. 11** will be adopted for all wheels. Until then, a hybrid system, namely, electric hydraulic braking system, driven by ball screws will be adopted for the front wheels, and electric braking system will be adopted for rear wheels from fail-safe design standpoint.

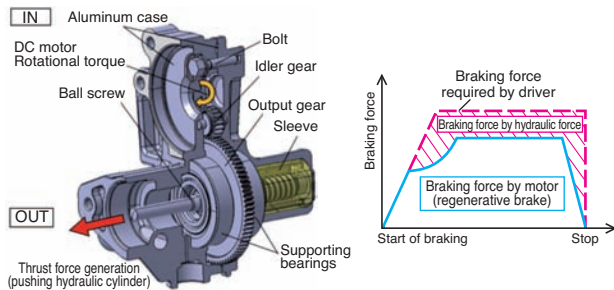


Fig. 10 Ball screw module to electric braking system



Fig. 11 Electric mechanical braking system

4. Conclusion

In next-generation vehicles with self-driving in mind, electric modules/systems which operate without steps will be used by developing electrification of operational/control system components.

NTN is poised to develop module/system products for each of “running”, “turning” and “stopping” based on NTN technology. Since the next-generation vehicle performance will depend on these components, this development is critical.

References

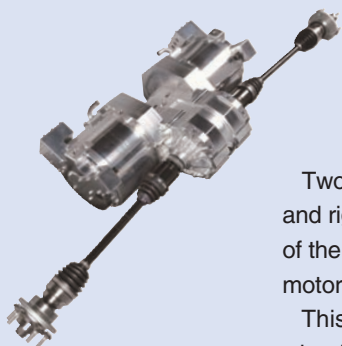
- 1) “Technology Roadmap Electric and plug-in hybrid electric vehicles”, IEA, p14 (2011)
- 2) NTN TECHNICAL REVIEW No 79, (2011) 22-28
- 3) Nikkei Business Publications, Inc. “HEV/EV Element Component Technology 2012-2013”
- 4) Nikkei Business Publications, Inc. “Automobile Component Industry: Path to Growth”
- 5) Nikkei Business Publications, Inc. “Next-Generation Vehicles” 2015

Photo of author



Makoto OKASAKA
Executive Officer,
Automotive Business HQ

Two Motor On-board Drive System



Ryou YUKISHIMA*
Hidenori KARASAWA*
Aiko MYOUKI*
Katsunori SATOU*

Yusuke MAKINO**
Takeshi KANDA**
Tomohiro SUGAI***

Two motor type electric vehicle has improved driving performances because the left and right wheels are driven by independent motors in accordance with driving conditions of the vehicle. NTN has focused on the two motor on-board type and developed "Two motor on-board drive system" that consists of motor drive units with an inverter.

This paper introduces overviews of this system and effects of independent left/right wheel drive.

1. Introduction

Recently, electric vehicles have gained attention as a measure against environmental problems such as global warming and air pollution, as well as energy supply problems with many initiatives taken by various factors for broader adoption ¹⁾.

The driving mechanism of electric vehicles can be broadly classified into the onboard method where the motor is placed on the vehicle body and the driving force is transmitted to tires through drive shaft ²⁾, and the in-wheel motor method where the motor is placed within the wheels to drive tires directly ^{3), 4), 5)}. The onboard method can be implemented onto the vehicles with suspension structure adopted by the conventional vehicles without any change.

The onboard method can be further classified into the 1-motor method and the 2-motor method. With 1-motor electric vehicles, the driving torque from the single motor is distributed to left and right wheels evenly by differential gears. On the other hand, with 2-motor electric vehicles, the left and right wheels are driven by their own motors depending on the driving conditions; therefore, it is possible to improve the turning performance and driving stability during driving on low friction roads.

NTN has focused on the 2-motor onboard method for these characteristics and developed a "2-motor onboard driving system". This system combines motor

driving units consisting of a reducer, motor, and inverter.

In this paper, we will introduce an overview of this system and the effect of independent driving mechanisms for the left and right wheels.

2. System configuration

2.1 Motor driving unit

Fig. 1 and **2** show the appearance of the developed 2-motor onboard drive system and structure of the motor drive unit. **Table 1** shows the specification of the motor drive unit and **Fig. 3** shows an image of the unit installed on the vehicle.

This drive unit consists of two motors and a reducer which transmits power from each motor by reducing rotational speed. The drive unit has a symmetric structure so that drive shafts of the same length can be applied to the left and right wheels. The coupling of this drive unit and drive shafts is placed in the center of the unit. This structure allows the drive shafts to be longer to place the reducer closer to the wheels. This can reduce the impact of position of the drive unit and reduce the variation of operational angle of the drive shafts due to vertical movement of tires. This results in an improved degree of freedom in designing and installation of the unit on the vehicles.

*Drive System Engineering, EV Module Business HQ

**Control System Engineering, EV Module Business HQ

***Chassis System Engineering, EV Module Business HQ

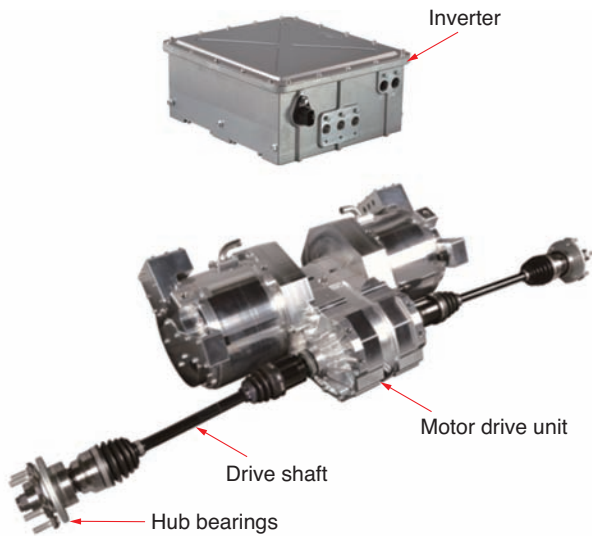


Fig. 1 Appearance of two motor on-board drive system

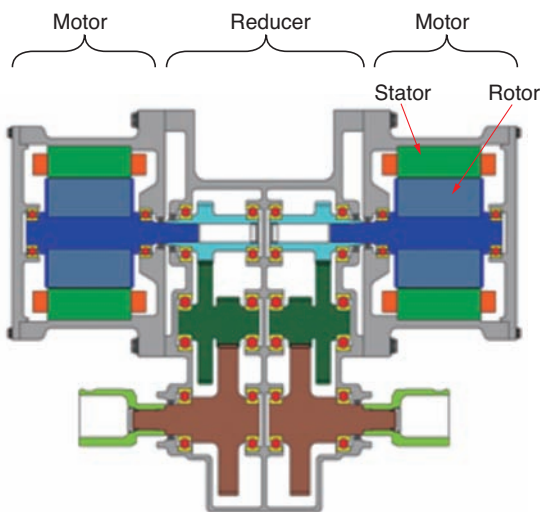


Fig. 2 Section of motor drive unit

Table 1 Motor drive unit specifications

Maximum output	50kW※
Maximum torque	1100Nm※
Maximum rotational speed	1300min ⁻¹ (Equivalent to 150 km/h assuming tire diameter of 0.6 m)
Reducer type	Parallel axis gear method
Reduction ratio	1/6.16
Cooling method	Motor part: water cooling Reducer part: air cooling

※ Value per wheel

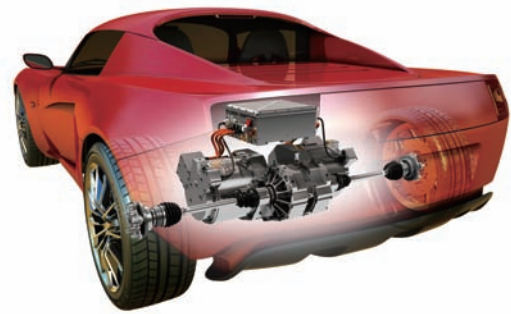


Fig. 3 Image of the vehicle equipped with the system

2. 2 Motor

The specification of the motor is shown in Table 2. Improvement of reluctance torque output was achieved by adopting distributed windings.

Table 2 Motor specifications

Motor type	Radial gap type permanent magnet synchronous moto
Winding method	Distributed winding
Maximum torque	180Nm
Maximum output	50kW
Maximum rotational speed	8000min ⁻¹

2. 3 Inverter

The specification of the inverter is shown in Table 3. This inverter houses all the circuits required for control of two motors in one enclosure. A portion of the circuit is common for both motors. With this configuration, the volume was reduced by 30% compared to cases installing individual inverters.

Table 3 Inverter specifications

Power supply voltage for driving	DC 250~400V
Power supply voltage for control	DC 12V
Maximum output	50kW × 2
Driving method	Sine-wave PWM
Cooling method	Water cooling

3. Performance

The efficiency of 1-motor and 2-motor drive units are shown in Fig. 4 and 5. The efficiency of the entire system including the inverter is shown in Fig. 6. The motor achieved 90% or more efficiency in a wide range of operational conditions and the maximum efficiency of the motor drive unit and entire system was 93% and 91%, respectively.

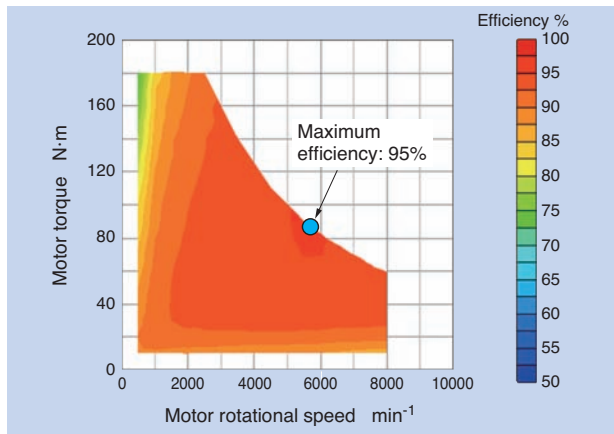


Fig. 4 Motor efficiency

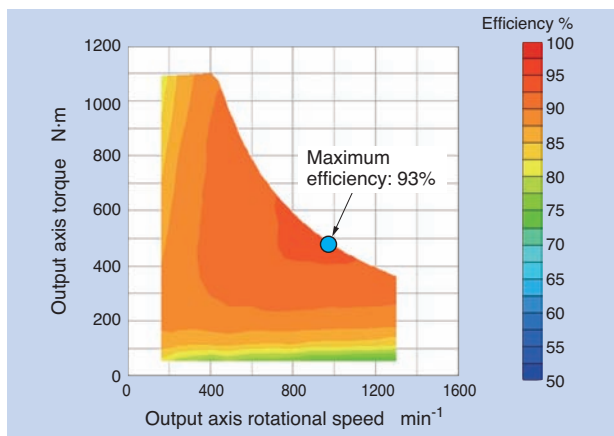


Fig. 5 Motor drive unit efficiency

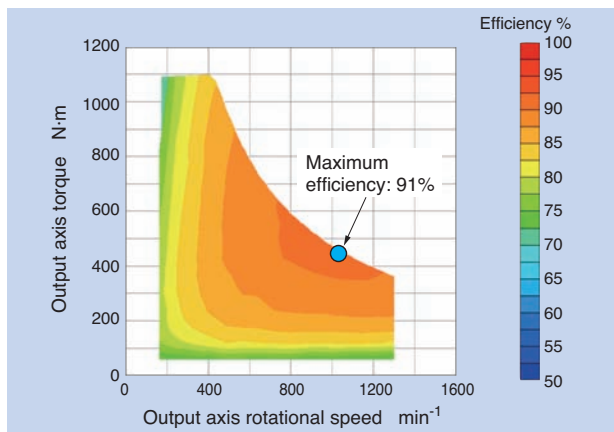


Fig. 6 Motor drive system efficiency

4. Vehicle motion control

4.1 Effect of independent drive for left and right wheels

Direct Yaw-moment Control (DYC), which controls vehicle motion by giving direct yaw-moment onto the vehicle body, is introduced more frequently, with the purpose of improving turning performance and driving stability. In general, yaw moment in DYC is generated by either differential gears with a driving torque distribution mechanism or friction brakes to give different driving/braking force to the left and right wheels^{6), 7)}.

The driving force control by electric motors has advantages for higher precision and responsiveness in generating torque compared with internal combustion engines. In addition, it can control not only driving torque but also braking torque. Furthermore, since this system drives the left and right wheels by their dedicated motors, it can control the vehicle yaw moment in any way, as required, with high precision.

Fig. 7 shows the concept of DYC by independent left and right drives. Typically, there is a delay in response of vehicle yaw-moment from steering. If yaw moment can be generated in the right timing against steering, the turning performance will increase.

By using the advantages of motor driving force control, the slip ratio can be controlled to effectively reduce slippage of tires when driving on a low friction road. In the verification test with the actual vehicles described in this paper, we applied Yaw-rate feedback Traction Control System (Y-TCS). Y-TCS reduces disturbance of the vehicle attitude by optimally controlling the slip ratio of the left and right wheels in a coordinated manner, in addition to the above slip ratio control.

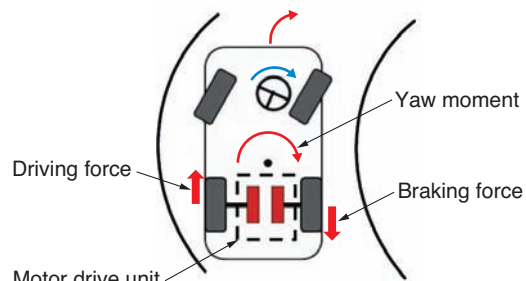


Fig. 7 Concept of DYC by the independent driving of each wheel

4.2 Vehicle with the system equipped

Fig. 8 and 9 show the appearance of the test vehicle equipped with this system and the view of the system installation from underneath, respectively. The specification of the vehicle with the system is shown in Table 4. The vehicle is based on a commercially available vehicle with this system installed on the rear side of the vehicle body. Underbody structure such as suspension, hub bearings and knuckles are not changed from the base vehicle.



Fig. 8 Appearance of the vehicle equipped with the system

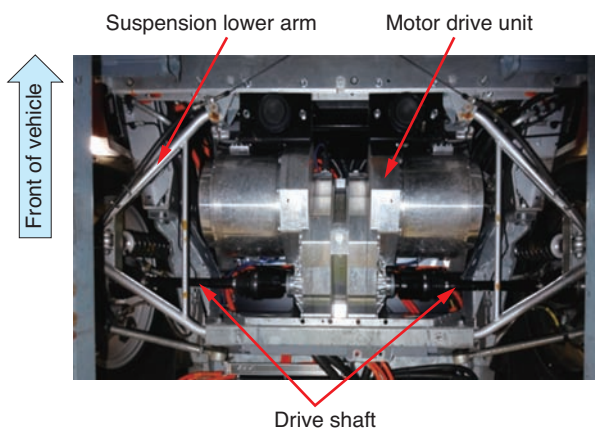


Fig. 9 State of the system mounted onboard

Table 4 Specifications of vehicle equipped with the system

Vehicle weight	1100kg	
Capacity	2	
Drive shaft	Rear 2 wheels	
Maximum output	50 kW x 2 wheels	
Maximum torque (wheel)	1100 Nm x 2 wheels	
Battery	Type	Li-ion
	Capacity	23.3kWh

4.3 Verification with actual vehicles

4.3.1 DYC

Fig. 10 shows the test results from driving with sine-wave steering angle input and Fig. 11 shows the picture of this driving test. Without DYC, the delay of the yaw-rate response was 50 ms against the change of steering angle. With DYC, the response was approx. 30 ms, which is a reduction of 60%. DYC showed an improvement in vehicle responsiveness.

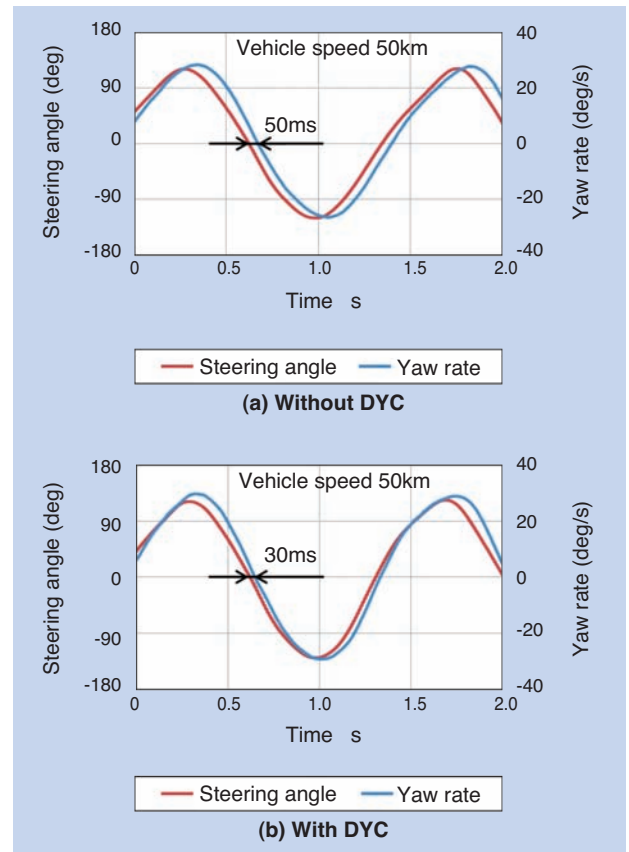


Fig. 10 Results of driving test with sine-wave steering angle input



Fig. 11 Driving test with sine-wave steering angle input

4.3.2 Control of slip ratio

Fig. 12 shows the change of speed of the driving wheels at the quick start of vehicles from a complete stop on the road with a low friction factor μ between the road surface and tire. The left and right wheels showed almost the same behavior; therefore, Fig. 12 only shows the behavior of the left rear wheel. By application of the slip ratio control, the wheel slips immediately after starting, and then tire rotation is sufficiently controlled following the target value.

Furthermore, in order to verify the effect of adding Y-TCS on the slip ratio control, we conducted the quick start test from complete stop on the split low friction road with different μ for the left and right wheels.

The result and the picture of the test are shown in Fig. 13 and 14, respectively. In this test, the steering angle was held at 0 degree (straight) and the acceleration pedal was stepped in to the maximum. As shown in Fig. 13, with Y-TCS, the deviation from the target route is reduced to less than 1/2 compared to without Y-TCS. This shows that the coordinated control of the left and right driving force according to disturbance of the vehicle attitude improves the steering stability when driving on a low friction road.

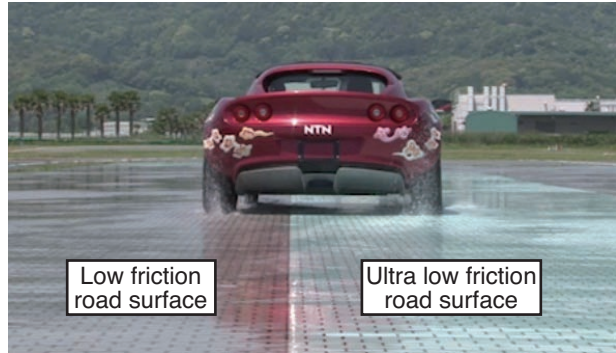


Fig. 14 Split friction road driving test

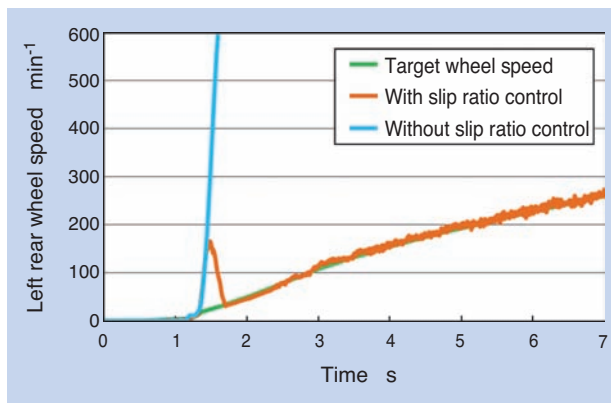


Fig. 12 Results of low friction road test

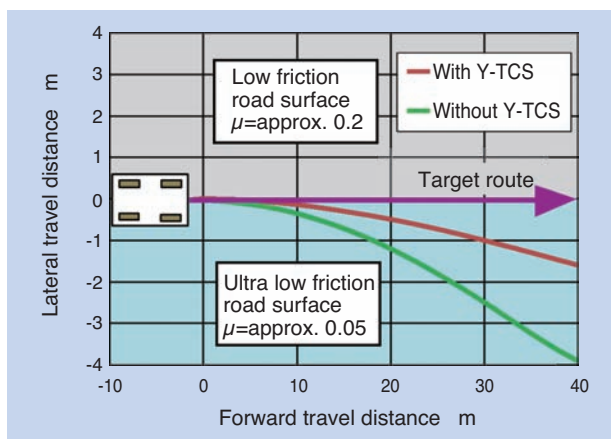


Fig. 13 Results of split friction road test

5. Conclusion

In this paper, we have introduced the structure and performance of the developed 2-motor onboard driving system. Independent drive on the left and right wheels by this system can improve both turning performance and driving stability of vehicles.

We will continue with the evaluation of the vehicle in Fig. 15 for further improvement of performance and reliability and address further enhancements.

Reference

- 1) Ministry of the Environment: Next Generation Vehicle Guidebook 2014, (2014)
- 2) Sano, et al.: Cutting-edge EV component technologies used in the "i-MiEV", Mitsubishi Motors Technical Review, No. 22, (2010) 23-28.
- 3) Murata: Development of In-wheel-motor drive unit, Proceedings of Society of Automotive Engineers of Japan, No. 28-10 (2010) 5-9.
- 4) Okamoto, et al.: Development of High Efficiency In-wheel Motor System for using 20 inch Wheel Mounted Motor, Toyo Denki Review, No. 117, (2008) 12-17.
- 5) Itoh, et al.: In-Wheel Motor System, NTN TECHNICAL REVIEW, No. 79, (2011) 22-28.
- 6) Kunii, et al.: Development of SH-AWD (Super Handling-All Wheel Drive) System, Honda R&D Technical Review, Vol.16, No.2, (2004) 9-16.
- 7) Ushiroda, et al.: Development of Super AYC, Mitsubishi Motors Technical Review, No. 15, (2003) 75-78.



Fig. 15 Appearance of converted vehicle

Photo of authors



Ryou YUKISHIMA
Drive System Engineering,
EV Module Business HQ



Hidenori KARASAWA
Drive System Engineering,
EV Module Business HQ



Aiko MYOUKI
Drive System Engineering,
EV Module Business HQ



Katsunori SATOU
Drive System Engineering,
EV Module Business HQ



Yusuke MAKINO
Control System Engineering,
EV Module Business HQ



Takeshi KANDA
Control System Engineering,
EV Module Business HQ



Tomohiro SUGAI
Chassis System Engineering,
EV Module Business HQ

Rear-wheel Independent Steering System



Yasuhiro MATSUNAGA*
Tatsuji INOUE*
Hironori TOKUNAGA*
Yukihiro NISHIO*

Rear-wheel steering in automobiles is a function to assist vehicle stability at medium to high speed driving as well as improve cornering at low speed driving and is already installed in some luxury-class models. NTN announced the “Rear-wheel Independent Steering System” that utilizes steer-by-wire technology for electronically-controlled steering in 2013, and has made further enhancements for even better response and a more compact, lighter weight design.

This report introduces the “Rear-wheel Independent Steering System” that is capable of toe angle control with a one body combined-type steering system.

1. Introduction

Four wheel steering (4WS) systems have long been known for improving driving stability by steering the rear wheels.

4WS systems were introduced into the market in the 1980s and later rear wheel steering by mechanical means was introduced. Unfortunately, drivers may have felt uncomfortable by the lag in the transmission of power. However, recent developments in electronic components and control technologies have made it possible to steer the wheels by motor drive. Because of the improvement in responsiveness, it is now possible to eliminate this uncomfortable feeling; consequently, this technology is being adopted, especially in luxury vehicles for enhanced driving stability.

Four wheel steering is a steering system to steer the rear wheels along with the front wheels depending on the driving patterns, and is classified into the modes shown in Fig. 1. The characteristics of each mode are as follows:

(1) In-phase

Mainly used in the mid/high speed range. The rear wheels are steered in the same direction as the front wheels when turning, to improve the stability and maneuverability for changing lanes and reduce cornering.

(2) Anti-phase

Mainly used in the low speed range. The rear wheels are steered in the reverse direction of the front wheels when turning to make the turning radius smaller.

(3) Toe-in

The front side of the rear wheels is steered inside (when the distance between the front sides of both tires is compared to the distance between the rear sides of both tires, the rear distance is wider). It improves the vehicle's straight line stability.

(4) Toe-out

The front side of the rear wheels is steered outside (when the distance between the front sides of both tires is compared to the distance between the rear sides of both tires, the front distance is wider). Not usually used.

NTN developed steer-by-wire steering system for front wheels in 2011¹⁾ and now applies this technology for developing rear wheel independent steering system capable of controlling each of the above mentioned modes.

In this paper, we will report the system configuration and results of the vehicle test.

*New Product Development R&D Center

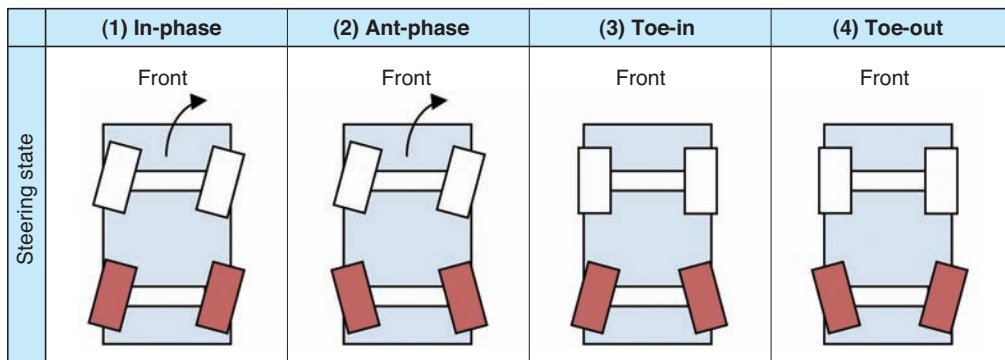


Fig. 1 Operation mode of 4WS

2. System overview

2.1 Structure

This system, which steers the rear wheels according to the angle of the steered front wheels, makes it possible to achieve in-phase and anti-phase steering control, as well as independent toe angles for left and right rear wheels by adopting an independent and symmetrical linear motion mechanism for the left and right wheels, as shown in Fig. 2. In addition, as shown in Fig. 3, since it can be installed on the chassis, there is no impact on the driving/riding comfort level due to the change of unsprung weight.

The linear motion mechanism uses hollow DC brushless motors for compactness, and the motor torque is transmitted to the trapezoidal screw through the planetary gear reducer to drive the rotation-restrained steering shaft.

The detailed internal structure is shown in Fig. 4 and 5. A large thrust external force (lateral withstand load) generated by stationary steering etc. is received by the needle thrust bearings located in the central part. The rolling motion in the radial direction is suppressed by the sliding bearings installed at the tips of the steering shaft and the trapezoidal screws, and

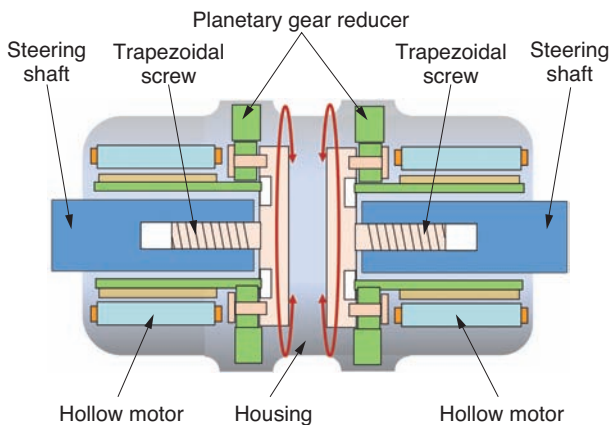


Fig. 2 Actuator structure

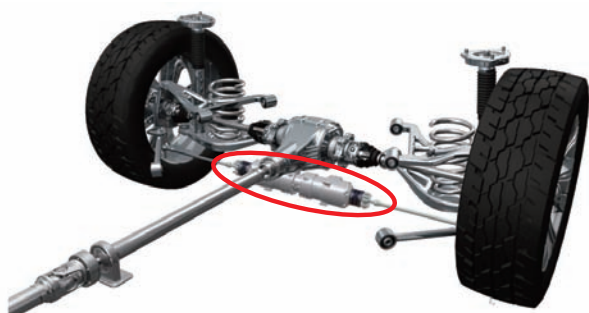


Fig. 3 Actuator layout

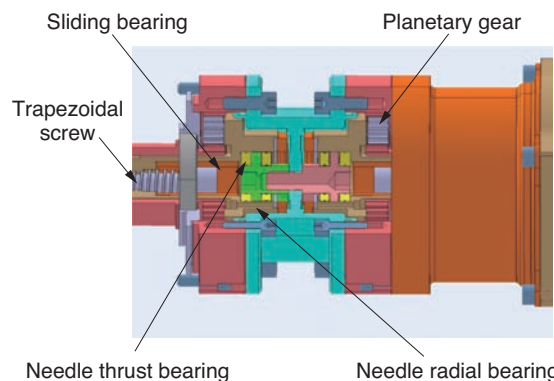


Fig. 4 Internal structure (Central part of actuator)

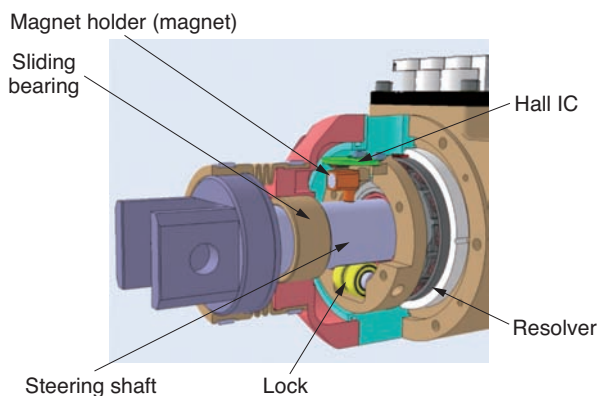


Fig. 5 Internal structure (Peripheral part of steering shaft)

the needle radial bearings supporting the outer diameter of the material that works as the carrier for the trapezoidal screw and the planetary gear. There is no displacement of the trapezoidal screw due to the thrust external force (lateral withstand load) since the efficiency for the reverse input to the trapezoidal screw is low. In addition, resin is used as the material for the planetary gear for quietness.

In addition, a resolver is used for controlling the motor. Furthermore, the flux changed due to the movement of magnets installed on the steering shaft is detected by the Hall effect IC to determine the absolute position of the steering shaft.

2.2 Specifications of the actuator

Table 1 shows the actuator of this system. The lateral withstand load is 3.5 kN or more on one side and is capable of addressing the upper medium to executive class of vehicles of around 4.9 m in total length.

Fig. 6 shows the measurement results of the relation between the lateral withstand load and shaft speed of the steering shaft. It can achieve a shaft speed of 30 mm/s or more with 2.5 kN of lateral withstand load.

Table 1 Specification of actuator

Item	Specification
Linear-motion method	Trapezoidal screw
Shaft motion level	±7 mm (max. motion level ±10 mm)
Motor	Brushless DC12V
Rotation sensor	Resolver (4X)
Reducer	Planetary gear reducer mechanism
Shaft absolute position detection	Hall IC
Lateral withstand load (one side)	3.5 kN or more
Maximum steering angle*	±2.5 degrees
Maximum feeder speed	30 mm/s (at lateral withstand load of 2.5 kN)
Mass	9 kg
Case size	φ81×375mm

*Reference only as the values vary depending on the vehicle structure

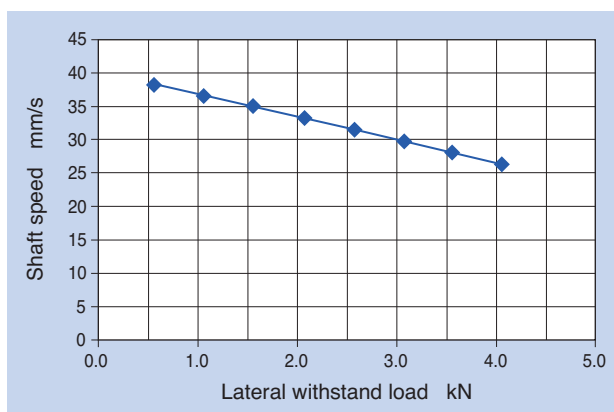


Fig. 6 Lateral load-rear steering speed characteristics

2.3 Control system

The control system consists of two ECUs which control the respective motor, as shown in Fig. 7. Two ECUs receive the target values of the steering angles according to the vehicle status from the upper ECU and determine the positions of each motor by PWM control.

These two ECUs have the functions of mutual monitoring and partial redundancy to increase safety.

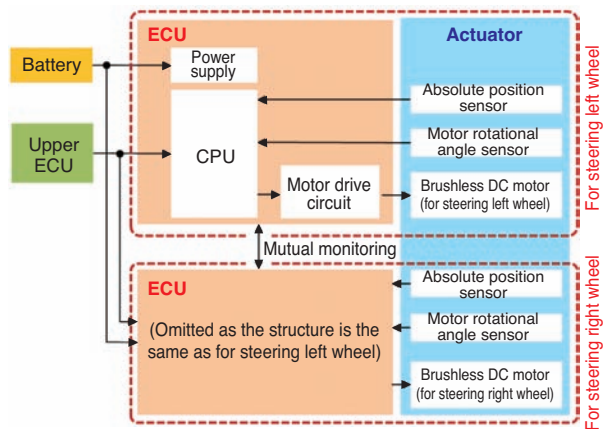


Fig. 7 Block diagram of control system

3. Rear wheel steering control method

In order to confirm the effect of this system with the actual vehicle, “Vehicle speed response type front wheel steering angle proportional control”²⁾, which is the typical control law when rear wheel steering is added to a vehicle, was adopted. In this paper, we will describe this effect from the basic motion properties of the vehicle against the steering operation.

The degree of freedom for the vehicular motion generated from steering is lateral, yawing and rolling, however, we can ignore rolling as the vertical movement is a secondary motion and if we set the following assumptions, we can consider the motion of a vehicle running at a constant speed in the horizontal X-Y plane shown in Fig. 8.

- Vehicular traveling velocity is constant
- Tire properties of the left and right tires are the same

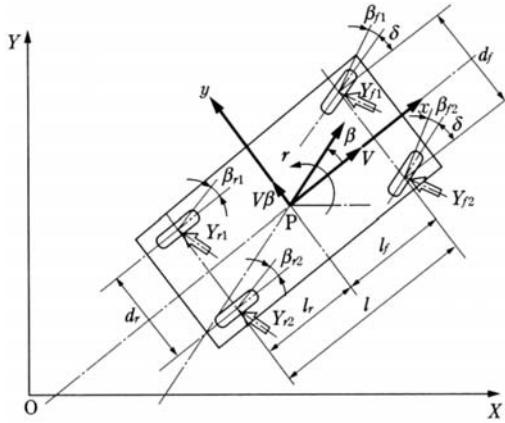


Fig. 8 Motion of vehicle

As mentioned above, the basic vehicular motion equation in a horizontal plane ignoring rolling can be expressed as follows:

$$mV \left(\frac{d\beta}{dt} + r \right) = Y_{f1} + Y_{f2} + Y_{r1} + Y_{r2} \quad (1)$$

$$I \frac{dr}{dt} = l_f (Y_{f1} + Y_{f2}) - l_r (Y_{r1} + Y_{r2}) \quad (2)$$

where,

- β : Lateral slip angle of the vehicular center of gravity
- V : Vehicular traveling velocity
- m : Inertial mass of the vehicle
- Y_{xx} : Cornering force given to tires
- r : Yaw angle velocity
- l : Yawing inertial moment of the vehicle
- l_f : Distance between the vehicular center of gravity and the front shaft
- l_r : Distance between the vehicular center of gravity and the rear shaft

If we assume that there is no difference between the properties of the left and right tires themselves, then there is no difference in the cornering forces felt by both tires. Therefore, if we set the cornering force of the front and rear tires as Y_f and Y_r , respectively, we get the following equations:

$$2Y_f = Y_{f1} + Y_{f2} \quad (3)$$

$$2Y_r = Y_{r1} + Y_{r2} \quad (4)$$

By considering this force to be the force on the y direction in Fig.8, equation (1) and (2) can be written as follows:

$$mV \left(\frac{d\beta}{dt} + r \right) = 2Y_f + 2Y_r \quad (5)$$

$$I \frac{dr}{dt} = 2l_f Y_f - 2l_r Y_r \quad (6)$$

When the lateral slip angle is small, the cornering forces acting on the tire Y_f and Y_r are proportional to the lateral slip angles of the front and rear tires β_f and β_r . By taking the counterclockwise angle positive, the cornering force, when the lateral slip angle is positive, can be written as follows, since the cornering force acts on the negative y direction in Fig.8:

$$Y_f = -K_f \beta_f \quad (7)$$

$$Y_r = -K_r \beta_r \quad (8)$$

where,

K_f : Front wheel cornering power

K_r : Rear wheel cornering power

In the above equations, when a small steering angle is given to the front and rear wheels, the lateral slip angle of the front and rear tires β_f and β_r can be approximated as follows:

$$\beta_f = \beta + \frac{l_f}{V} r - \delta_f \quad (9)$$

$$\beta_r = \beta - \frac{l_r}{V} r - \delta_r \quad (10)$$

where,

β_f : Front wheel steering angle

β_r : Rear wheel steering angle

Assigning equations (9) and (10) to equations (7) and (8), the cornering force can be expressed as follows:

$$Y_f = -K_f \left(\beta + \frac{l_f}{V} r - \delta_f \right) \quad (11)$$

$$Y_r = -K_r \left(\beta - \frac{l_r}{V} r - \delta_r \right) \quad (12)$$

By assigning equations (11) and (12) to equations (5) and (6), the following motion equations can be obtained:

$$mV \frac{d\beta}{dt} + 2(K_f + K_r) \beta + \left\{ mV + \frac{2}{V} (l_f K_f - l_r K_r) \right\} r = 2K_f \delta_f + 2K_r \delta_r \quad (13)$$

$$2(l_f K_f - l_r K_r) \beta + I \frac{dr}{dt} + \frac{2(l_f^2 K_f + l_r^2 K_r)}{V} r = 2l_f K_f \delta_f - 2l_r K_r \delta_r \quad (14)$$

The above equations are the basic motion equations describing the vehicular motion for the front and rear wheels in the horizontal plane.

“Vehicle speed response type front wheel steering angle proportional control” adopted with the vehicular tests, the front steering angle and rear steering angle can be written as follows:

$$\delta_f = \frac{\delta}{n} \quad (15)$$

$$\delta_r = k \delta_f = \frac{k}{n} \delta \quad (16)$$

where,

- δ : Steering angle
- n : Gear ratio of front wheel steering system
- k : Steering angle ratio

By assigning the equations (15) and (16) into the equations (13) and (14), calculating k so that the lateral slip angle β of the vehicle center of gravity becomes 0, and by rearranging the equation, we obtain:

$$k_0 = - \frac{l_r \left(1 - \frac{m l_f}{2 l_r K_r} V^2 \right)}{l_f \left(1 + \frac{m l_r}{2 l_f K_f} V^2 \right)} \dots\dots\dots (17)$$

If we set the proportional constant of the rear wheel steering angle against the front wheel steering angle as set in equation (17), we can achieve zero lateral slip angle of the vehicular center of gravity in steady-state circular turn, which, theoretically, aligns the vehicular direction and its traveling direction. The steering angle ratio k is determined by the vehicle specifications. With the vehicle we used in this test, it provides anti-phase at lower speed and in-phase at higher speed with the switch occurring at around 50 km/h of speed, as shown in Fig.9.

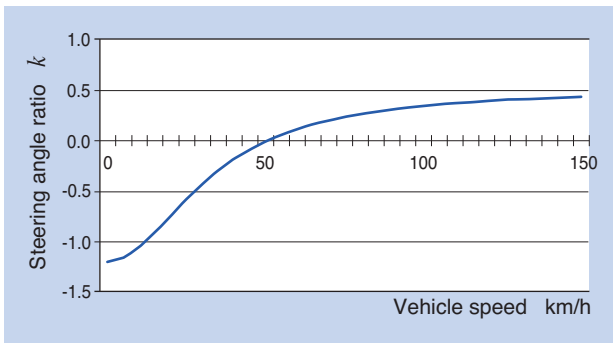


Fig. 9 Steering angle ratio

4. Vehicle test

4.1 Test vehicle and driving conditions

We installed this system in the test vehicle with the specifications shown in Table 2 and conducted driving tests on the test course. We used “Vehicle speed response type front wheel steering angle proportional control” described in the previous section to determine the rear wheel steering level according to the front wheel steering angle and the vehicle speed, and evaluated the vehicle response under actual driving.

Table 2 Specifications of test vehicle

Item	Specification
Vehicle size	4940x1940x1500 (LxWxH mm)
Weight	Approx. 1700 kg
Drive method	Rear wheel drive
Rear-wheel max. steering angle	±2.5 degrees
Rear-wheel max. steering speed	10 degrees/s (axial force: 2.5 kN)

4.2 Response evaluation

The test was conducted in the double lane change course with a dry surface, as shown in Fig. 10, with the vehicle entering the course at the speed of 70 km/h and maintaining the speed as constant as possible, and the yaw rate and lateral acceleration against the steering angle were recorded. Fig. 11 shows the results.

When the rear wheel steering function is OFF (Fig. 11 (a) and (c)), there will be a delay in the trackability of the yaw rate and the lateral acceleration against the steering angle requiring the driver's unnecessary steering manipulation. On the other hand, when the rear steering function is ON (Fig. 11 (b) and (d)), the rear wheels turn approx. 1.5 degrees in-phase with the front wheels at 70 km/h. As a result, it is revealed that the linearity of lateral acceleration and yaw rate with respect to the steering angle are improved. This means that the driver is operating the vehicle as desired, with improved trackability of the yaw rate and lateral acceleration against the steering handling , proving the effect of the rear wheel steering for driving stability.

With actual vehicles, there is a difference between these quantitative data and the feeling that the drivers sense when steering. By applying various tunings at the vehicle level, we are ready to develop this technology by leveraging the advantages of 4WS that contribute to driving stability.

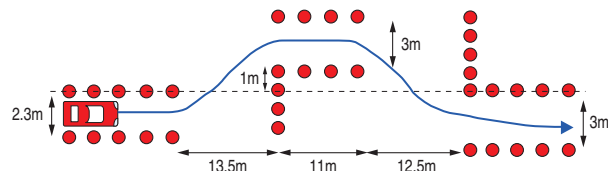


Fig. 10 Test course

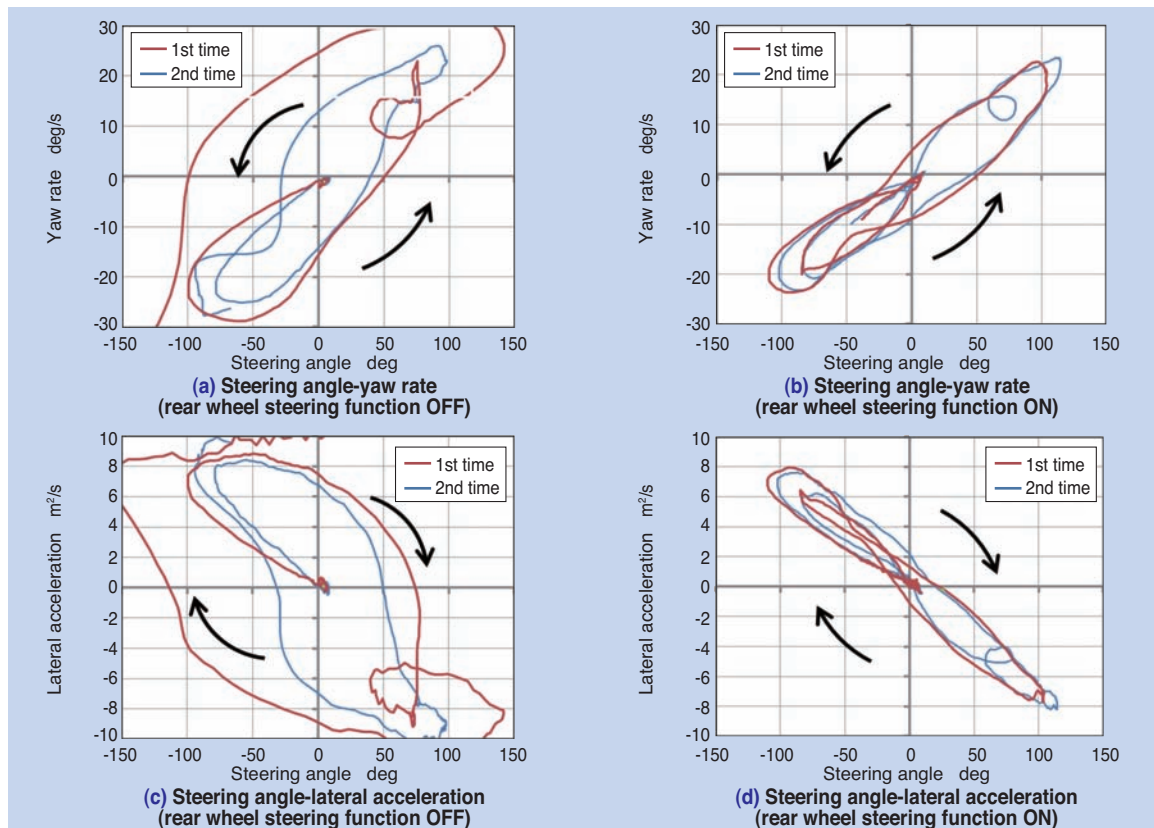


Fig. 11 Linearity control test result at 70km/h

5. Conclusion

In this paper, we introduced the "rear wheel independent steering system". With actual vehicle tests, we have confirmed the effect of the in-phase mode, however, since this system is able to independently and proactively control the toe angles of the left and right wheels regardless of the suspension structure, it is possible to apply various steering controls according to the driving conditions. By using these features, it is expected that toe-in for improved driving stability and anti-phase mode for automatic parking, etc. are expected to be applied.

Along with the electrification of vehicles, the adoption of by-wire technology and the development

of autonomous vehicles, market expansion of these module products to contribute to the performance enhancement of safety, stability and convenience is expected to continue. To be prepared for further development of the electrified modules including vehicle control technologies, we strive to develop new module/system products that contribute to the electrification, improved fuel consumption and enhanced driving performance of vehicles.

References

- 1) Katsutoshi MOGI, Tomohiro SUGAI, Ryo SAKURAI and Nobuyuki SUZUKI, Development of New Steer-by-wire System, NTN TECHNICAL REVIEW No79, (2011) 42-50.
- 2) Masato ABE: Automotive Vehicle Dynamics (2nd Edition), Tokyo Denki University Press (2012) 5-226.

Photo of authors



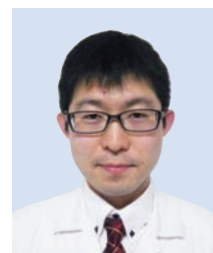
Yasuhiro MATSUNAGA
New Product Development
R&D Center



Tatsuji INOUE
New Product Development
R&D Center



Hironori TOKUNAGA
New Product Development
R&D Center



Yukihiro NISHIO
New Product Development
R&D Center

MCU (Mechanical Clutch Unit) for Next Generation Steering



Naotsugu KITAYAMA*
Shintaro ISHIKAWA*

The next generation steering system which controls steering with electric signal starts to be adopted for the purpose of automated cruise or alleviating driver's fatigue. On the other hand, the system must be obtained something mechanical back up function in case of emergency condition such as electric failure.

By using the NTN's own MCU (Mechanical Clutch Unit) technology, NTN has developed "smaller" backlash type new MCU for the next generation steering system. And it has very useful feature which makes a quickly locking when the electric power is shut off, it is our unique technology.

1. Introduction

Recent improvements in function and reliability of electronic control capabilities have enabled conventional mechanical control systems to be replaced by electrical control systems, as is the case with brake and acceleration by wire. One technology leading this trend is steer by wire (SBW), which is the next generation steering system aimed at autonomous driving and reduction of driver fatigue.

SBW can be broadly classified into three types, as shown in Fig. 1¹⁾.

Type 1 is a system that changes steering angles by operating angle control mechanisms consisting of a conventional steering system, motor and reducer.

Type 2 transmits the steering angle of the steering wheel by an electrical signal to the steering actuator to control the vehicle steering angle, with a mechanical backup mechanism to enable steering when electrical

failure occurs.

Type 3 is similar to type 2 without the mechanical backup mechanism. Instead, an electrical backup system, like those in aircrafts, is installed to introduce redundancy. Current regulation requires a mechanical backup mechanism for steering when electrical failure occurs, which makes it difficult to introduce Type 3 into the market.

Therefore, the mainstream SBW technology for vehicles is expected to be the type 2 for the time being, with a reliable mechanical backup mechanism.

NTN has developed a mechanical backup mechanism: a compact and high torque capacity mechanical clutch unit (MCU) with reduced backlash for next generation steering. The MCU contains a newly adopted ball cam mechanism that converts linear motion to rotational motion and has the optimum layout of rollers in the roller clutch, based on our proprietary technology.

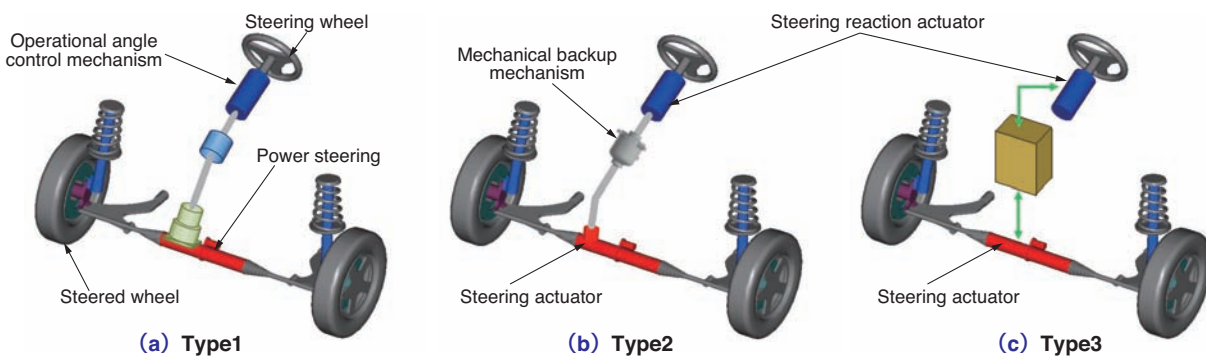


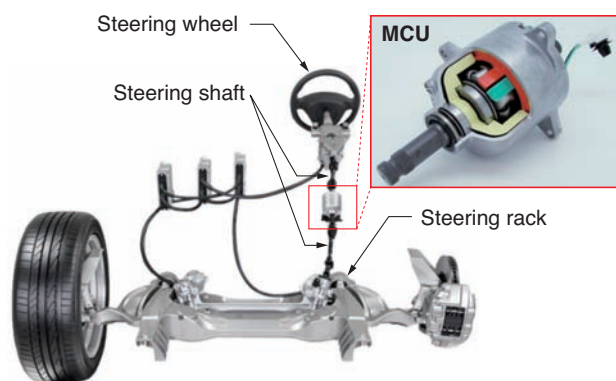
Fig. 1 Types of next generation steering

*Automotive Business HQ

2. Application area of MCU for next generation steering (introduction of direct adaptive steering※)

Direct adaptive steering (DAS) is the world's first next generation steering system that Nissan Motor introduced to the market. NTN's MCU is installed as the mechanical backup mechanism of this DAS (Fig. 2).

DAS releases the roller clutch coupling by supplying current to the electromagnetic clutch inside the MCU, and connects the steering wheel and the steering rack, that had been mechanically connected, with electrical signaling. When electrical failure occurs and current to the electromagnetic clutch is lost, the embedded roller clutch is immediately engaged to mechanically connect the steering wheel to the steering rack, enabling traditional vehicle steering.



Direct adaptive steering
Photo: Courtesy of Nissan Motor Corp.

Fig. 2 Layout of MCU for DAS

3. NTN proprietary technologies supporting MCU for next generation steering

The MCU for next generation steering requires the following three points as a backup mechanism:

- (1) Secure engagement and release of roller clutch
- (2) Reduction of backlash while the roller clutch is engaged
- (3) Low friction

We have created a compact MCU with high torque capacity and reduced backlash by:

- (1) adopting a new ball cam mechanism
- (2) placing a pair of rollers in the roller clutch area

The design of our MCU contains the roller clutch and electromagnetic clutch made into a single unit, which is our proprietary technology. Table 1 shows the specification of the MCU for the next generation steering system.

Table 1 Specifications of MCU for next generation steering system

Size	φ85×190mm
Rated torque	80N·m
Response time	0.1 s or less

3.1 Adoption of ball cam mechanism

The typical electromagnetic clutch transmits power from the input shaft to the output shaft when current is supplied. No power is transmitted when current is not supplied. This is called positive operation. However, as the backup mechanism of SBW, the roller clutch must be engaged to transmit power when electric failure occurs (reverse operation).

We adopted a ball cam in the developed MCU, which converts the linear motion of the electromagnetic clutch to rotational motion. It is placed between the electromagnetic clutch and roller clutch to adjust the circumferential position of two cages. In this configuration, the roller clutch is released when current is supplied to the electromagnetic clutch, and power is not transmitted from the input shaft to the output shaft. When current is not supplied to the electromagnetic clutch, the roller clutch is engaged to transmit power from the input shaft to output shaft, achieving reverse operation (Fig. 3).

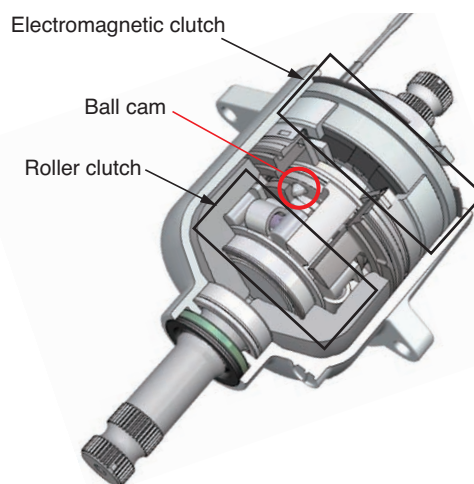


Fig. 3 Structure of MCU

3.2 Improvement of roller placement

Conventional MCUs are single roller clutch systems with one roller placed on the cam surface. However, in the MCU for next generation steering, we introduced a twin roller clutch system where two rollers are placed in a pair to reduce backlash when the rotational direction is switched (Fig. 4).

※Registered trademark of Nissan Motor Corp.

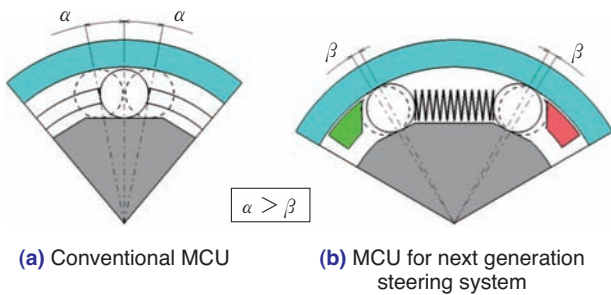


Fig. 4 Reducing backlash

3.3 Operation principles

The following indicates the operation principles for releasing and engaging the roller clutch (Fig. 5).

<Releasing roller clutch (SBW state)>

- (1) When current is supplied to the electromagnetic clutch, cage 1 is attracted to the electromagnetic clutch (linear motion in axial direction).
- (2) The linear motion of cage 1 is converted to rotational motion by the ball cam mechanism and cage 1 and 2 rotate in opposite directions (conversion from linear motion to rotational motion).
- (3) Due to the counter rotation of cage 1 and 2, the distance between the rollers is reduced.
- (4) Due to the gap between the output shaft and the rollers, power from the input shaft (steering wheel) is not transmitted to the output shaft, resulting in SBW state.

<Engaging roller clutch (mechanical coupling state)>

- (5) When current is not supplied to the electromagnetic clutch, the rollers are maintained at the engaging position by the pressure of the spring located between the rollers.
- (6) When power is given from the input shaft to the output shaft, the rollers are pushed into the “wedge” made between the input shaft cam surface and the output shaft, making mechanical connection.

4. Evaluation test

4.1 Torsional endurance test

Fig. 6 shows the torsional endurance test result of applying 1,000,000 cycles of load while measuring the repetitive rated torque in the CW/CCW direction at the input shaft, with the roller clutch engaged. The rated torque of roller clutches is determined by the repetitive torque load, and is 80 N·m for the MCU for next generation steering. There were no issues, such as increase of backlash, breakage or wear before and after the test.

4.2 Measurement of rotational torque

Fig. 7 shows the result of the rotating torque test when the input shaft is rotating in one direction while the roller clutch is released. The increase in rotational torque remained within 10% of the rotational torque of the embedded bearing, accomplishing low friction.

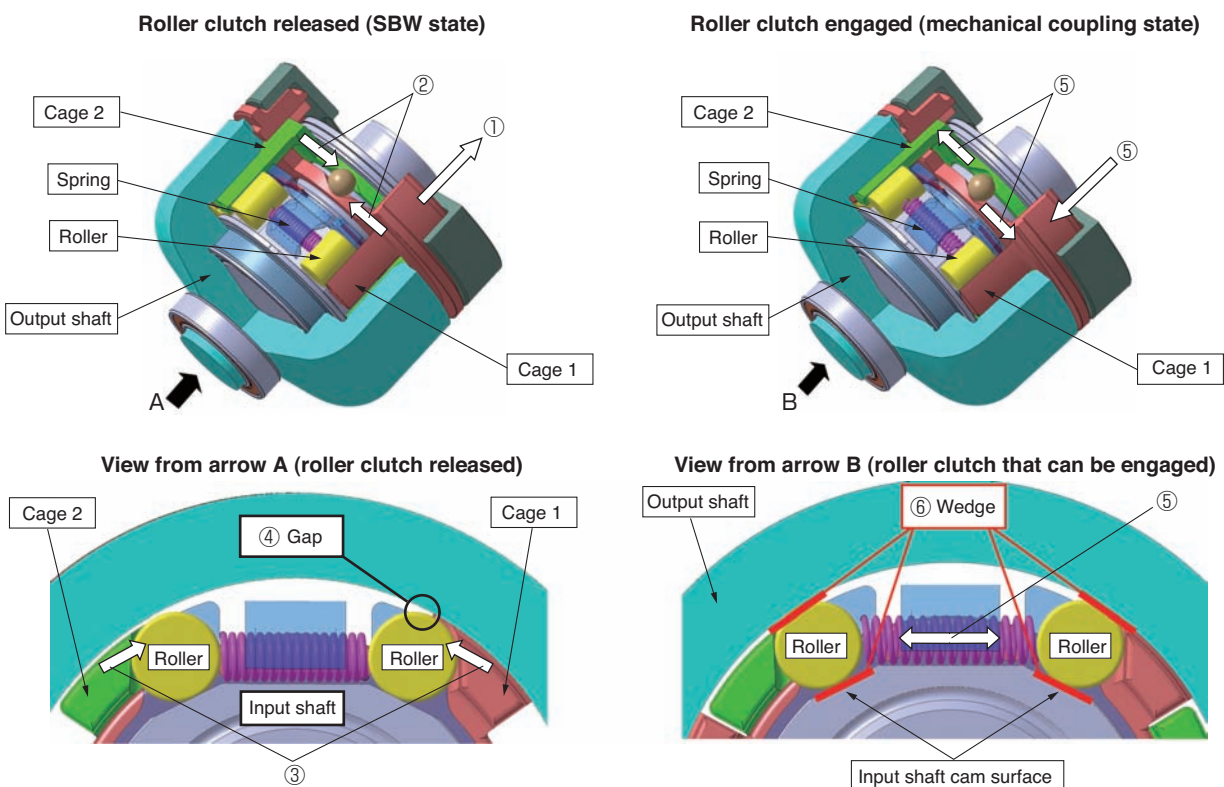


Fig. 5 Roller clutch mechanism (Pattern diagram)

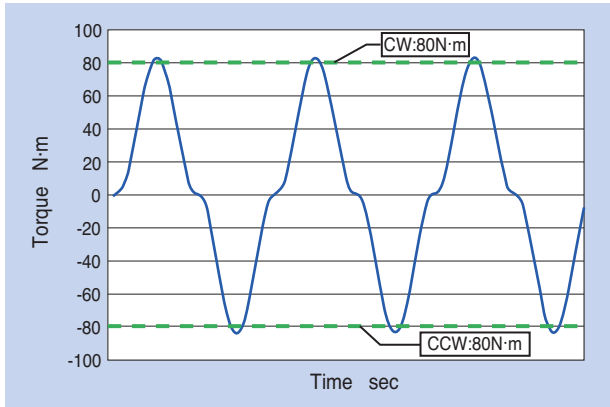


Fig. 6 Result of torsional endurance test

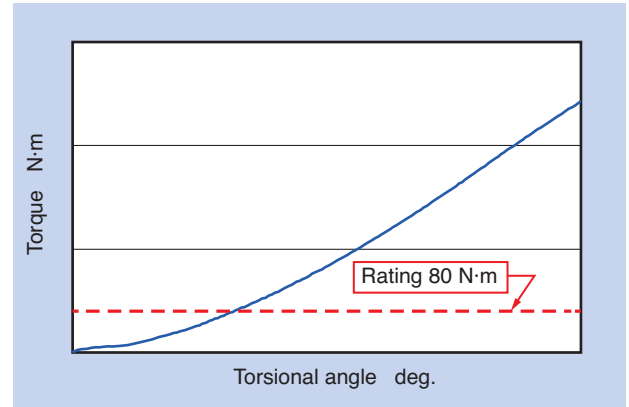


Fig. 8 Result of Static torsional strength test (example)

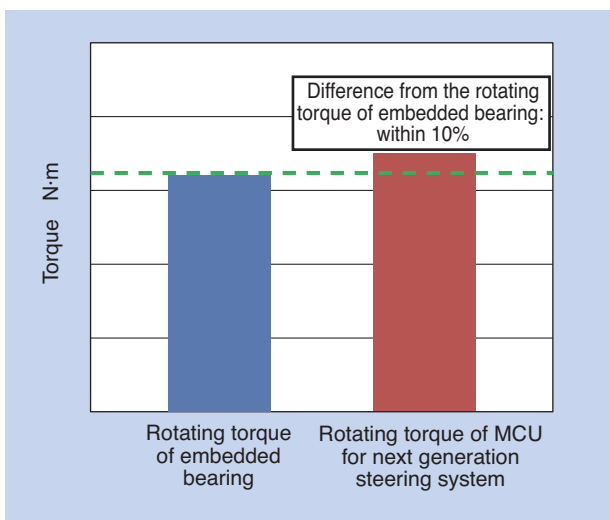


Fig. 7 Result of rotating torque test

4.3 Static torsional strength test

Fig. 8 shows the result of static torsional strength test with torque applied in one direction while the roller clutch is engaged. When the roller clutch is engaged, it possesses the rated torque of 80 N·m or more.

5. Conclusion

In this paper, we have introduced NTN's MCU for next generation steering, with reduced backlash from the adoption of a ball cam, and placing a pair of rollers in the roller clutch area. These developments are NTN's proprietary technology. We will launch it in the market as a product to add backup function to next generation steering systems, contributing to improved reliability.

Reference

- 1) Automotive Electronics Research Group, TER Sougougi Ken, Corp., Current Status and Future of Automotive By-Wire Technology, 2014 Edition, Sougougi Ken, Corp, (2014) 68-97.

Photo of authors



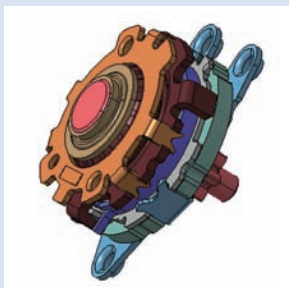
Naotsugu KITAYAMA
Automotive Business HQ



Shintaro ISHIKAWA
Automotive Business HQ

Clutch for Seat Lifter

Masayoshi YAMADA*
Yasumasa HIBI*



NTN has been developing torque diode for seat lifter that adjusts the height of a seat cushion with manual action. Market deployment has been begun since 2002. For safety improvement of seat, high brake capacity and reliability are required for torque diode.

In this paper, we will introduce the structure and our product line-up.

1. Introduction

Requirements for vehicle safety have increased more than ever in recent years. Countries around the world are conducting assessments for improved vehicle safety and the assessment criteria for passenger protection performance are made stricter every year.

Seats for vehicles (hereinafter called seats) are one of the components which significantly affect the passenger protection performance. NTN has been developing clutches for seat lifters which are capable of manually adjusting the seat height to the desired position*1, and then held, contributing to the safety and comfort of seats.

This product uses NTN's unique mechanism, the "Torque Diode," and we introduce its function, mechanism and line-up in this paper.

*1 Jointly developed with Shiroki Corporation

2. Function of the torque diode

A torque diode is a bidirectional engaging clutch based on a roller clutch mechanism, that can be used to transmit the rotating force from the input to the output side, while locking the rotating force from being transmitted from the output to the input side. By using this function, the up/down seat height can be continually adjusted, and its position held, by operating the lever installed on the side of the seat.

Fig. 1 shows the typical installation of the torque diode on the seat.

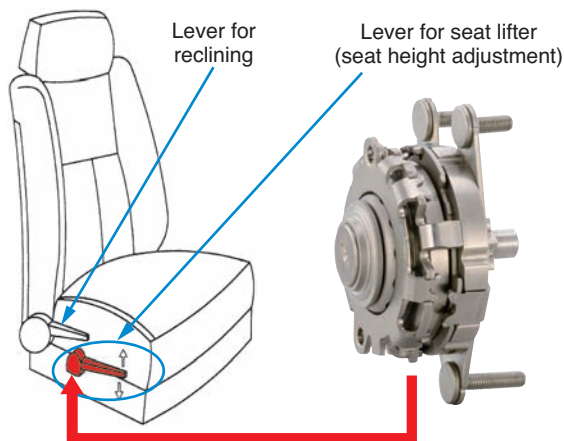


Fig. 1 Installation condition of torque diode

Fig. 2 shows the layout of the torque diode and the sector gear installed on the seat.

When a load is applied to the seat, the torque is transmitted to the pinion gear (output shaft) of the torque diode via the sector gear (link mechanism) and the seat height is held by locking the torque diode.

On the other hand, when the lever is operated from the input side, the pinion gear rotates and the entire seat moves up/down and forward/backward by the link mechanism of the sector gear, and so the seat height can be adjusted.

*Automotive Business HQ

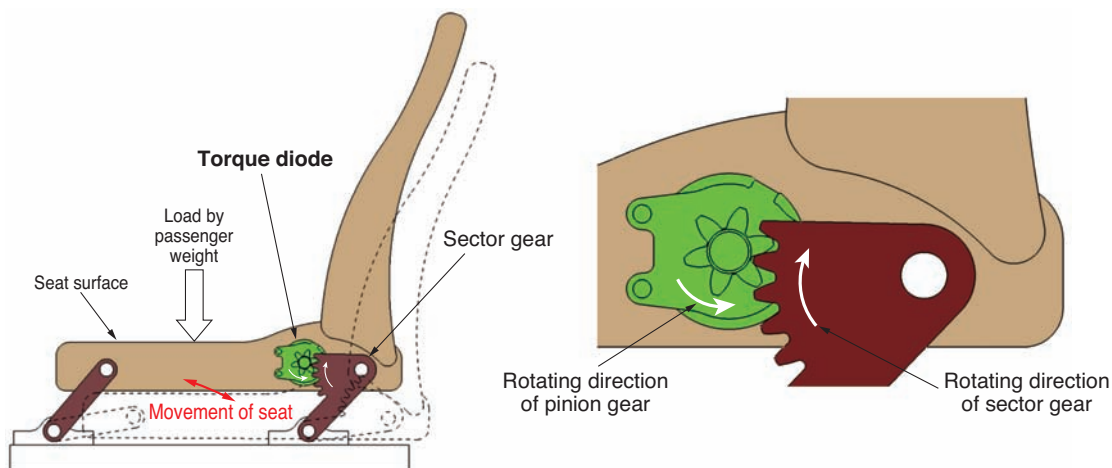


Fig. 2 Layout of torque diode

3. The mechanism and operating principle of the torque diode

The torque diode for the seat lifter is required to have both

- (1) An ability to hold the seat height, and
- (2) An ability to move the seat up and down by controlling the lever.

As shown in Fig. 3, the torque diode consists of two clutches, a clutch on the brake side with the above mechanism (1) and a clutch on the lever side with the function of transmitting the up/down operation of the lever to the clutch on the brake side. With these two clutches, the output components of the lever-side clutch (inner ring) and the input components of the brake-side clutch are made into one assembly.

Structure/operation principle

(1) The mechanism to hold the seat height

Fig. 4 shows the torque transmission path when the seat height is held. The load from the seat is transmitted from the pinion gear to the outer ring on the brake side fixed to the stationary seat frame via the roller of the brake-side clutch; consequently, the output shaft becomes locked in order to maintain the seat height. Fig. 5 shows the pattern diagram of the cross section of the clutch on the brake side, for this example. A pair of rollers and a spring are inserted into the wedge-shape space formed by the output shaft and the inner diameter of the outer ring, and because the rollers are pushed into the narrow area of the wedge-shape space by the spring, the assembly is locked.

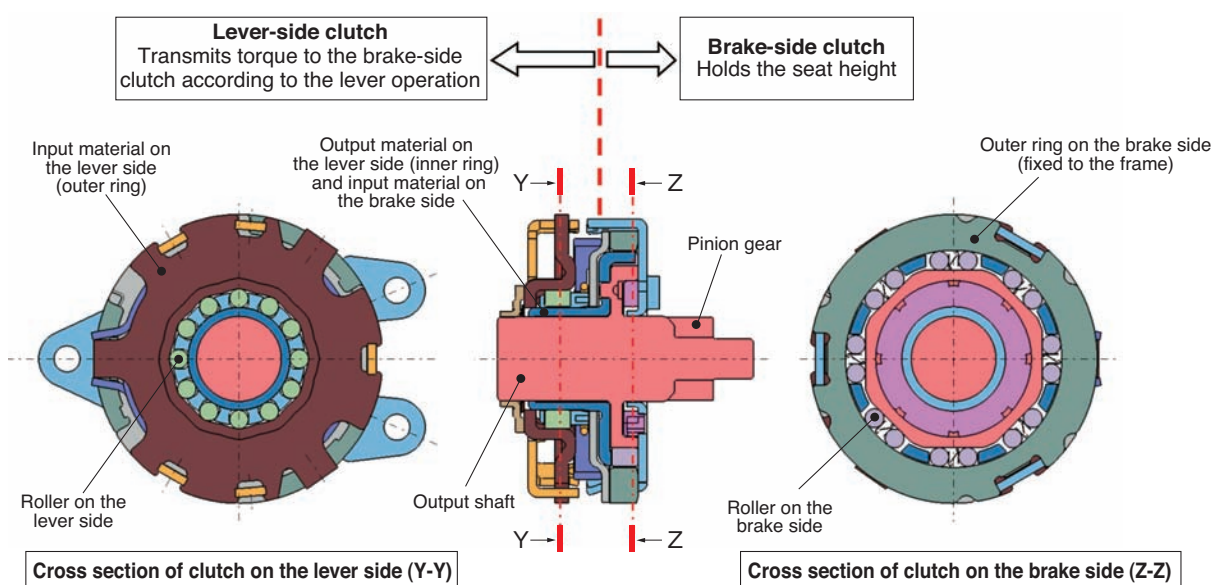


Fig. 3 Structure of torque diode for seat lifter

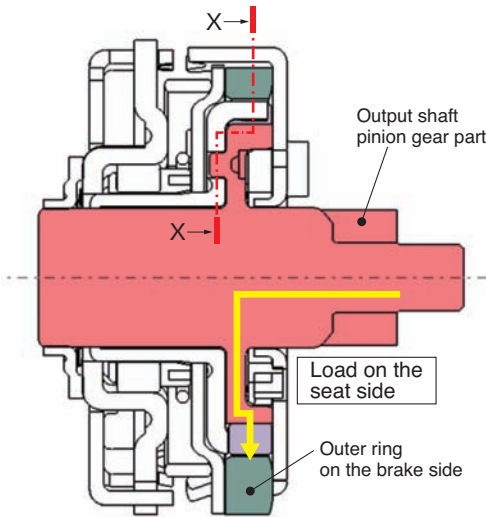


Fig. 4 Torque flow at neutral position

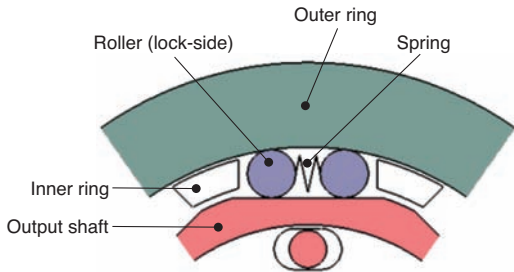


Fig. 5 Neutral position of brake-side clutch (cross section viewed from X-X)

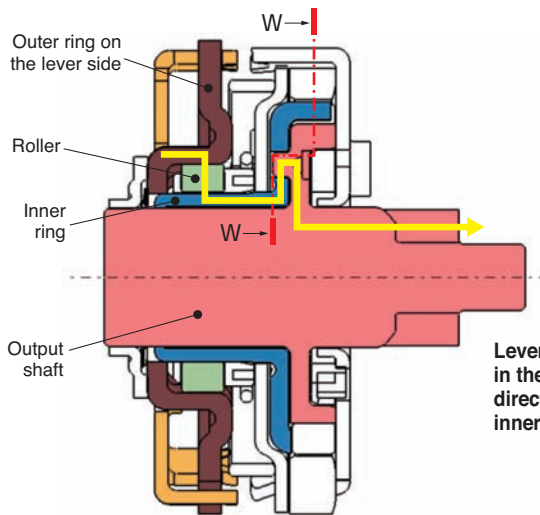


Fig. 6 Torque flow at switching position

(2) The mechanism to move the seat up and down by controlling the lever

When the seat is moved up/down by the lever operation, the rollers on the brake-side clutch need to be released from the wedge-shaped space and the torque from the lever-side clutch needs to be transmitted to the pinion gear and the sector gear. The torque transmission path when operating the lever is shown in Fig. 6. By using this lever, the torque is transmitted to the output shaft of the brake-side clutch via the lever-side outer ring, rollers and inner ring.

At the start of the rotation of the inner ring, the side of the pillar section of the inner ring pushes the roller onto the brake-side clutch, moving it to the wider area of the wedge-shape space (unlocking the output shaft; Fig. 7 (a)).

Rotating the inner ring further, the rotating force of the inner ring is transmitted to the output shaft by the contact of the elongated hole of the inner ring and the protruded portion of the output shaft (Fig. 7 (b)).

When the lever stops moving, the rollers are pushed to the wedge-shaped space by the compressive force of the spring placed between the rollers, and the locking state is restored, where the rotation of the output shaft is locked in both directions, (Fig. 5).

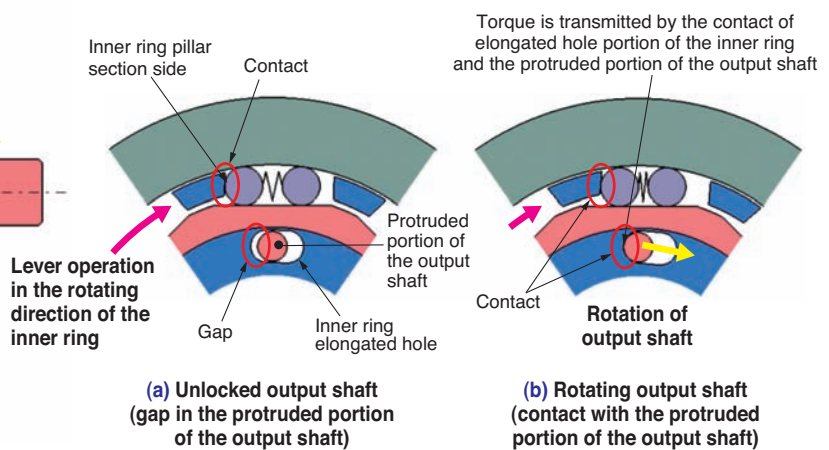

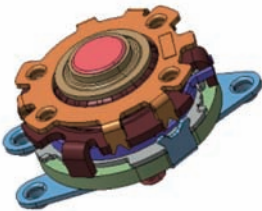
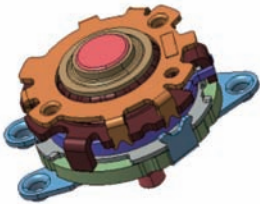



Fig. 7 Switching position of brake-side clutch (cross section of viewed from W-W)

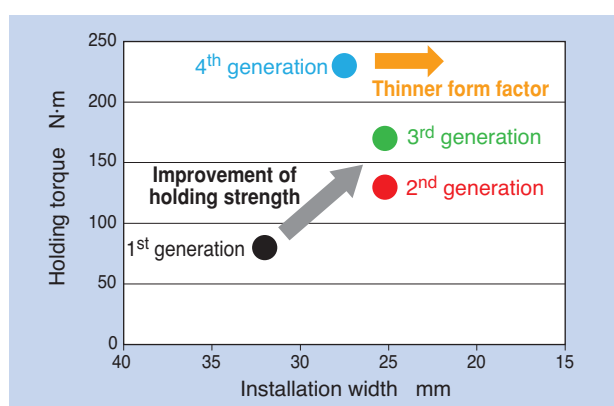
Table 1 Product line-up of torque diode for seat lifter

	Appearance	Specification	Characteristics
1 st generation		(1) 80N·m (2) $\phi 50 \times 32$ mm (3) 330g	<ul style="list-style-type: none"> Thin outer ring is adopted as the outer ring of the brake-side clutch Lightweight and compact design
2 nd generation		(1) 130N·m (2) $\phi 60 \times 25$ mm (3) 380g	<ul style="list-style-type: none"> Thinner and higher torque realized by thinner outer ring of the brake-side clutch Improved seat holding tolerance against rear-ended accidents Improvement in comfort level along with larger seat cushion
3 rd generation		(1) 170N·m (2) $\phi 61 \times 25$ mm (3) 390g	<ul style="list-style-type: none"> Improved safety against collision by higher torque, yet maintaining similar installation size as the 2nd generation
4 th generation		(1) 230N·m (2) $\phi 61 \times 27$ mm (3) 420g	<ul style="list-style-type: none"> Improved safety against collision by even higher torque than the 3rd generation by longer rollers

(1) Holding strength (2) Clutch OD x Installation width (3) Weight

4. Product line-up and features

Since starting mass production in 2002, we have been responding to the market needs of increasing seat height holding capability and tighter space constraints. We have a line-up of products, up to the 4th generation, which have been adopted by many auto manufacturers and vehicle models (Table 1 and Fig. 8).

**Fig. 8** Performance comparison

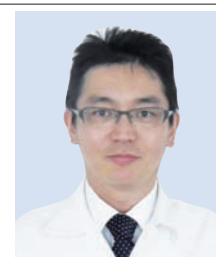
5. Conclusion

In this paper, we have introduced the function and mechanism of the torque diode, invented by NTN, as well as the product line-up. The torque diode is an important product contributing to the improved safety and comfort of seats. We will continue to improve/develop products that meet market needs.

Reference

- Masahiro KAWAI, NTN TECHNICAL REVIEW No. 79 (2011) Torque Diode for Seat Lifters

Photo of authors

Masayoshi YAMADA
Automotive Business HQYasumasa HIBI
Automotive Business HQ

Next-generation Driveshaft “ADS Module”



Masafumi OOSUGI*
Tatsuro SUGIYAMA*

Recently, low-fuel consumption and weight reduction are important problems worldwide in the automotive industry. And, development speed-up and development man-hour reduction according to standardization of a car component are also important problems. Responding to these problems, NTN proposes to worldwide automobile manufacturers the ADS module (Advanced Drive Shaft module) which modularized the constant velocity joint (CVJ) and hub-bearing (H/B) for drivetrain with a new concept and high manufacturing technology.

1. Introduction

The power from the engine is transmitted to the tires through the transmission, differential gear (hereinafter, differential) and drive shaft. Because the differential gear shaft, which is the shaft to input power, and the hub bearings (H/B), which support the tires, rotate at different angles, the drive shaft uses a constant velocity joint (CVJ). This ensures that torque is transmitted smoothly and with constant velocity.

The requirement specifications for a differential, H/B and torque vary depending on the vehicle.

Conventional drive shafts require combining CVJs and shafts individually designed according to the required specifications. Each vehicle requires repeating trial productions and evaluations, which results in longer development lead time.

NTN possesses technologies accumulated from research and development activities with the background of one of the world's top class sales volume, and state-of-the-art manufacturing technologies such as the "press-connect method" joint, which will be described later, and electron beam welding, ¹⁾. By using these technologies, we are proposing the next generation drive shaft called "Advanced Drive Shaft (ADS) module". ADS combines various components that are different depending on the vehicle types, such as shafts with different lengths and shapes and CVJ components commonly designed according to the required torques.

2. Structure and features

The ADS module is a combination of the tire side and the differential side or "EBW drive shaft", which will be discussed later. The tire side is made by connecting a CVJ and a H/B that is standardized with common architecture based on torque requirement with the "press connect method". The differential side is made by connecting a CVJ similarly standardized with common architecture based on torque requirement and individually designed stem part with electron beam welding.

2.1 Common specifications

The specifications of the internal components such as inner rings, cages, balls, and boots which constitute CVJ are already standardized with the common architecture.

With the ADS module, NTN is designing CVJs on the tire side and the cup of the CVJ on the differential side with the common architecture. The H/B, the stem on the differential-side CVJ, and the shaft to be engaged between the tire-side CVJ and the differential-side CVJ are to follow the individual specifications according to the vehicle model (Fig. 1 and 2).

2.2 Features of PCS-H/J

For connection, the splines are pre-formed on the inner diameter of H/B with smaller tooth width than the outer ring stem splines (pre-spline) and gaps are provided between the tips of the stem teeth and the bottom part of the grooves of H/B, enabling a bolt joint

*Drive Shaft Engineering Dept. Automotive Business HQ

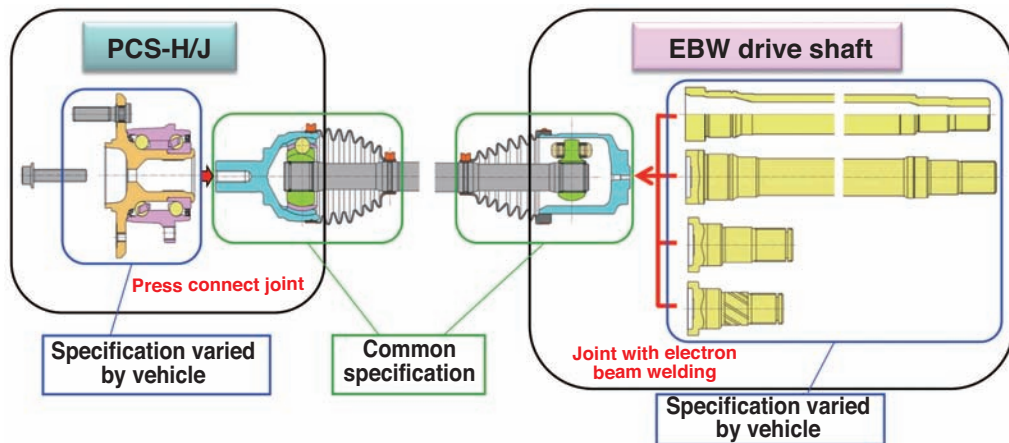


Fig. 1 Structure of ADS module



Fig. 2 Structure of ADS module (photo)

and reducing the load required for the joint process. This joining method is called the press connect method (PCS). By this design, the assembly process of vehicle production line of the automotive manufacturers is not required to be changed for assembling the PCS-H/J (Fig. 3).

This joining method is characterized by significant reduction of weight and elimination of backlash of the spline joint. With this method, there is no gap in the joint as opposed to the conventional spline joint; therefore, the input torque can be uniformly borne by the entire circumference. We could also reduce the length of the CVJ stem by approx. 65%. Furthermore, the weight was reduced to 0.94 kg/unit (approx. 12% compared with the conventional unit in case of application to the C segment) by thinning the inside wall of the hub ring and the use of a bolt instead of a nut.

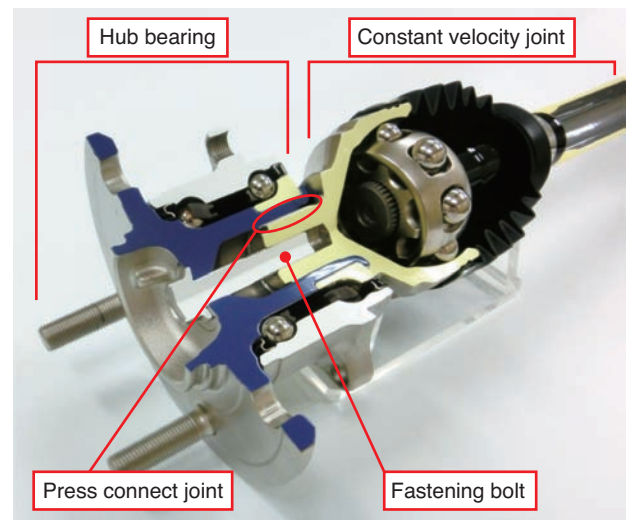


Fig. 3 Structure of PCS-H/J

2.3 Features of EBW drive shaft

Electron beam welding (EBW) is developed for connecting the common cup (outer ring) and the stem (shaft) (Fig. 4).

In the case of long stem type, the joint of EBW drive shaft can be made closer to the cup when compared with conventional friction welding. Therefore, EBW is a more suitable joining method for common cups.

In the case of short stem type, the cup has been conventionally integrated. However, by separating the stem, which shape can vary depending on the vehicles, we could achieve commonality of cups.

The welding quality is better than the other welding methods because it is done in a vacuum, with less welding flaws and sufficient strength to meet the requirements.

Furthermore, since there is no flash on the joints, the turning process can be eliminated after the joining process.

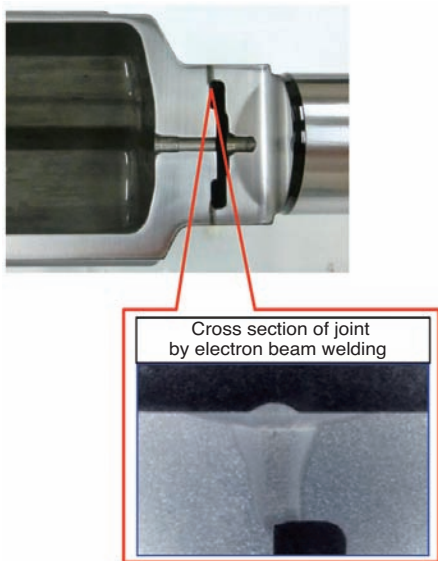


Fig. 4 Structure of EBW driveshaft

3. Summary

The ADS modules can reduce the development lead time of drive shafts and contribute to the vehicle ride quality and fuel economy by making the module products smaller and lighter.

We will proactively propose the ADS modules to the auto manufacturing industry.



Fig. 5 Application

Reference

- 1) Takayuki NORIMATSU, Tsutomu NAGATA, Press Connect Spline Hub Joint, NTN TECHNICAL REVIEW No. 81, (2013) 58-63.

Photo of authors



Masafumi OOSUGI
Drive Shaft Engineering
Department,
Automotive Business HQ



Tatsuro SUGIYAMA
Drive Shaft Engineering
Department,
Automotive Business HQ

Technology Trends and Products for Accessory Drive Belt Systems

Ayumi AKIYAMA*
Hiroo MORIMOTO**



As a superior car in the mileage, strong and mild HEVs are increasing and the accessory drive belt system is diversifying. On the other hand, requests for the accessory drive belt system are changing rapidly under the influence of ISG (Integrated Starter Generator) and engine downsizing.

This paper introduces the technology trends and products of NTN for the accessory drive belt system corresponding to the change of the engine.

1. Introduction

Various expectations have been given to automobiles throughout their history of 100+ years. They must be capable of transporting people and cargo quickly and securely to distant places, as well as providing pleasure and relaxation in our daily lives. Automobiles have been responding to these expectations by adding more and more complex equipment with greater functionality. In addition to these continually growing expectations, the next generation of vehicles is further required to deal with protecting the environment and saving resources.

NTN has been developing and marketing light and compact auto tensioners and pulleys for accessory drive belt systems to respond to these requirements¹⁾.

Fig. 1 shows an engine overview and examples of NTN products for engine accessory applications. The focus of this paper is to introduce the structure and features of NTN's auto tensioners and pulleys.

2. Current status of accessory drive belt systems

2.1 Configuration of accessory drive belt system

Vehicle engines drive each accessory system such as water pump, A/C compressor and alternator by transmitting the rotation of the crankshaft through pulleys and belts. The belt setting method has

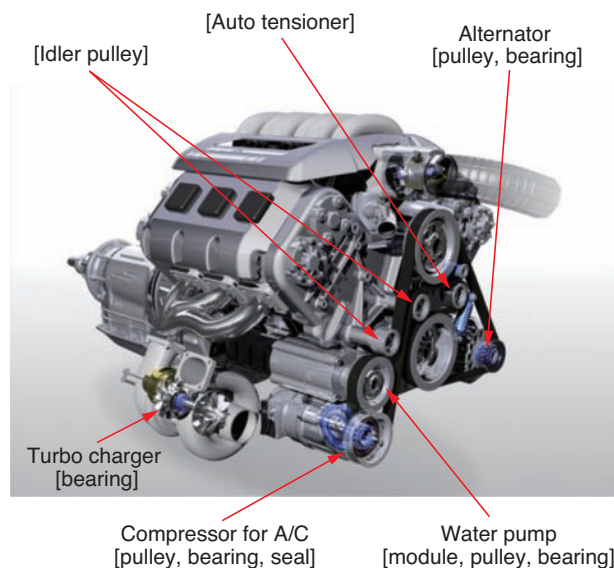


Fig. 1 The view of automotive engine with NTN products

transitioned from a multiple belt-setting, where individual belts drive each accessory pulley from the crank pulley, to a single belt-setting (serpentine method) which reduces the total length of the engine. This transition caused a large variation of accessory belt tension due to thermal expansion/compression of the entire engine and degradation of belt over time. An auto tensioner is adopted to absorb this variation of tension and extend the belt life.

*Application Engineering Dept. Automotive Business HQ

**Automotive Product Design Dept. Automotive Business HQ

2.2 Fuel saving technology for the accessory drive belt system

Today, adoption of an idling stop system is increasing as a fuel saving technology. Traditionally, the starter motor was used to restart the engine after idling stop. However, to reduce the time required to restart the engine, and to reduce the noise and vibration, the belt drive ISG (Integrated Starter Generator) method is being adopted, using the alternator as the starter motor (Fig. 2). The ISG method is characterized by compatibility with the conventional accessory system layout, superb quiet operation due to the friction-belt transmission mechanism, and short engine restarting time.

The ISG method does present a challenge for the auto tensioner, in that the area of high tension and low tension of the belt switches when changing between restarting the engine and steady driving (Fig. 3). Typically, the auto tensioner is set at a position where the belt is in low tension during steady driving. When the engine restarts with the ISG, the area of high tension and low tension switches, and the tension at the belt position where auto tensioner is set is instantly increased. The conventional auto tensioner

used today is deeply pushed in by this increased belt tension, creating slippage between the pulley and belt. This can not only cause a squeaking sound and reduced belt life, but also may result in failure to restart the engine. If the initial tension is set higher in order to prevent slippage during the high transmission torque needed to restart the engine, friction loss during steady driving becomes high, resulting in adverse fuel economy effects.

In general, loads on accessory drive belt systems are expected to continually increase. For example, with the recent trend of downsizing engines and adding turbochargers, the variation of crankshaft rotational speed will be larger due to the reduced number of engine cylinders. Furthermore, with the adoption of a 48V battery in progress in Europe, it is expected that loads on the alternator (generator) will increase along with larger battery capacity. Therefore, accessory belts and pulleys, will be required to have increased durability and higher load capacity. It is the auto tensioner that reduces these loads on accessory drive belt system, and unprecedented new functions will be required to balance these loads.

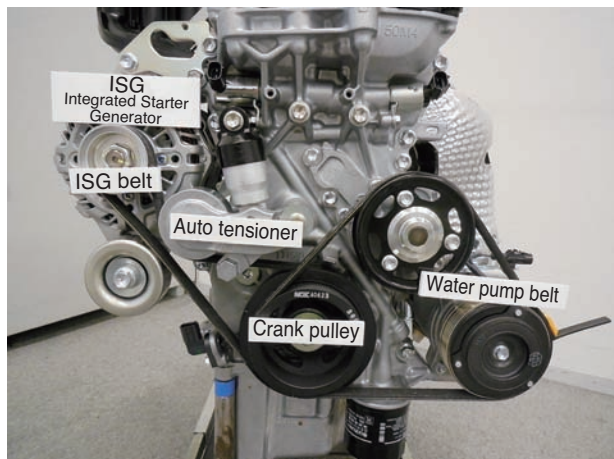


Fig. 2 Engine equipped with ISG²⁾

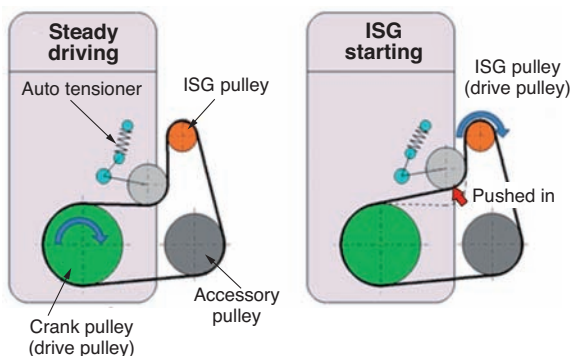


Fig. 3 Modes of belt span at the time of steady driving and engine starting

3. NTN's auto tensioners and pulleys for accessory drive belt systems

The following is an overview of NTN's auto tensioner as well as steel and resin pulley options for use in engine accessory drive belt systems.

1) Auto tensioners

The accessory drive belt system transmits driving power from the crank pulley to each accessory component pulley through friction of the drive belt. The auto tensioner for the accessory system belt functions to guarantee a minimum tension, as well as to reduce any excessive tension in the system.

Auto tensioners for accessory system belts can be broadly classified into mechanical auto tensioners and hydraulic auto tensioners, depending on the damper method used to absorb the variations in belt tension. The mechanical system provides damper effect through friction resistance with material such as resin, along with compression/torsion springs. Therefore, the damper properties are significantly changed by variation of the friction coefficient. In addition, the maximum load capacity is limited by the property of the adopted spring. It is not suitable to use this type of auto tensioner for engines with an ISG system, because they cannot withstand the instant high loads. On the other hand, the hydraulic auto tensioner provides damper effect by the resistance of oil passing through the internal oil channel. Therefore, it is possible for the hydraulic tensioner to cope better with

the sudden change of belt tension and high load compared with the mechanical system.

NTN has developed and launched highly reliable hydraulic auto tensioners with advanced functions. Our compact and high load short type auto tensioners have been adopted for use on the aforementioned engines equipped with ISG systems. Fig. 4 shows the structure of NTN's short type auto tensioner for high load. This product can sufficiently address the sudden increase of belt tension when restarting an engine with an ISG.

Since the hydraulic auto tensioner follows variation of belt tension very closely, when used on an engine with a large variation of tension, the tensioner reaction force may increase more than necessary resulting in excessive belt tension. In order to prevent this excessive belt tension, NTN has developed a new auto tensioner with a relief mechanism, improving on the short type auto tensioner. Fig. 5 shows the structure of the hydraulic auto tensioner with relief mechanism.

Currently, short type auto tensioners for high loads are applied to engines with ISG systems. However, they require a higher setting for belt tension compared with ordinary (non-ISG) engines, which results in slightly higher belt friction losses. As the competition

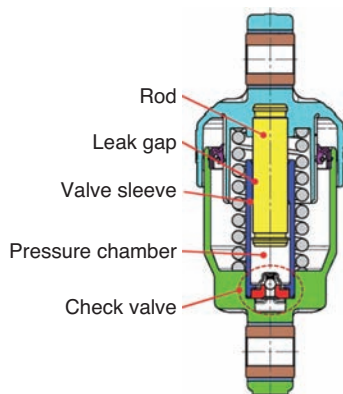


Fig. 4 Short type auto tensioner for high-load

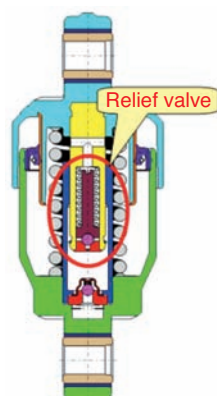


Fig. 5 Auto tensioner with relief valve

for lower fuel use intensifies, NTN has developed the variable damper type auto tensioner. This new auto tensioner automatically changes the damper properties such that the belt tension is maintained low during normal driving and high belt tension is generated when starting the engine to prevent slippage. This product is introduced in "Auto Tensioner with the Variable Damper Mechanism for ISG-equipped Engine" in this issue of the Technical Review.

2) Steel pulleys

Steel pulleys for accessory systems combine steel pulley material and dedicated bearings in one unit. These can be broadly classified into pulleys made by machining the pulley material and pulleys manufactured by press forming. The machined pulleys are characterized by high load carrying capacity and reliability; however, they may become costly in volume production due to the machining process.

On the other hand, pressed pulleys can be made at low cost and are suitable for volume production; however they have a lower degree of freedom in their design compared with machined pulleys. Pressed pulleys are limited in producible section geometries, and as a result, it has been difficult to use them for high load applications. Accordingly, NTN has developed the "Low cross-section high strength pressed pulley" which has a strength equivalent to machined pulleys, yet is producible with the highly productive press forming process. Fig. 6 shows the comparison of cross-sections between the conventional pressed pulley and the low cross-section high strength pressed pulley.

As shown in Fig. 6, the new design has proportionally less cross section area against the total height compared with the conventional product. Due to this smaller cross-section, the size of the bearing

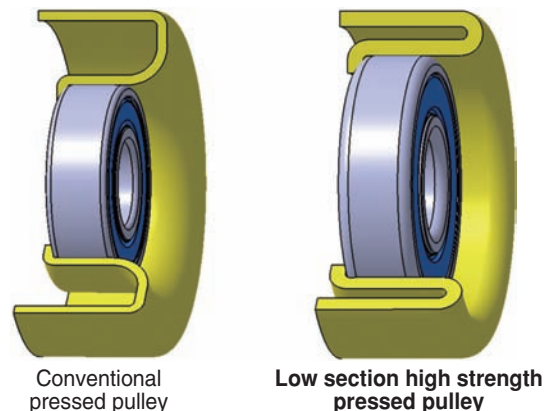


Fig. 6 Cross-section of conventional pulley and developed product with press forming

can be made larger without changing the outer diameter of the pulley. In addition, by making the pulley material thicker, the load carrying capacity of the pulley and bearing can be increased with the same installation size.

On the other hand, recently, Additionally, due to the recent improvement of accessory belt bending durability, smaller pulleys are being adopted. In this case, it is also possible to maintain the bearing size and make the pressed pulley outer diameter smaller through use of this new low cross section high strength design.

3) Resin pulleys

Resin pulleys can be used for a significant reduction of weight compared with steel pulleys. However, because of their lower load capacity, in addition to challenges with wear and environment tolerance, they were not typically selected for use in real world applications.

However, since the requirement for improvement of fuel economy has increased, adoption of resin pulleys is now expanding by both European and North American auto manufacturers. The lightweight and low inertia properties of resin pulleys lead to improved fuel economy. The material mainly used for resin pulleys is thermoplastic polyamide resin. For improvement of mechanical properties, PA66+ organic reinforcement material is now being adopted instead of PA6+ inorganic reinforcement material.

NTN is introducing a “high load resin pulley” with increased load tolerance. A phenol resin has been adopted, which is thermosetting resin instead of the conventional thermoplastic resin. With this material, these new resin pulleys are able to withstand an equivalent load to a steel pulley, which was not possible with the conventional resin pulleys. Phenol resin is generally considered as hard and brittle, but with recent progress in technologies for various additives, materials with improved toughness have been developed. In addition, the manufacturing process has recently evolved, enabling injection molding with this new material that is equivalent to the process used with thermoplastic resin. Also, the cost and productivity of compression molding, which used to be the mainstream process, has been improved.

Fig. 7 shows the appearance of a steel pulley and a resin pulley. Through adoption of the thermoplastic resin, these pulleys can be used in a relatively high temperature environment, achieve 1/3 of the weight and equivalent load capacity as the steel pulley of the same installation size.

In addition, it is expected that this material will be used to make various types of pulleys, leveraging the

properties of the resin to form complex shapes and be insert molded with other components.

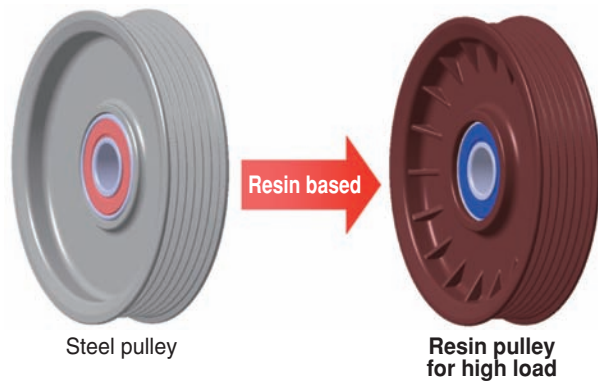


Fig. 7 Steel pulley and resin pulley

4. Future trends of accessory drive belt systems

Fig. 8 shows the fuel consumption regulations in key regions. The EU has the strictest target of reducing the CO2 emission to 95 g/km by 2021. To achieve this target, the EU focused on mild hybrid vehicles using a 48V power supply.

The EU auto manufacturers are aiming at further fuel efficiency improvement by not only by restarting the engine after an idling stop but also by regeneration, assist, and driving with an electric motor depending on the conditions, lengthening the time the engine is not in use.

Downsizing of engines, along with the adoption of turbochargers and idling stop mechanisms are being increasingly used in many vehicle models as an effective means for improving fuel economy. On the

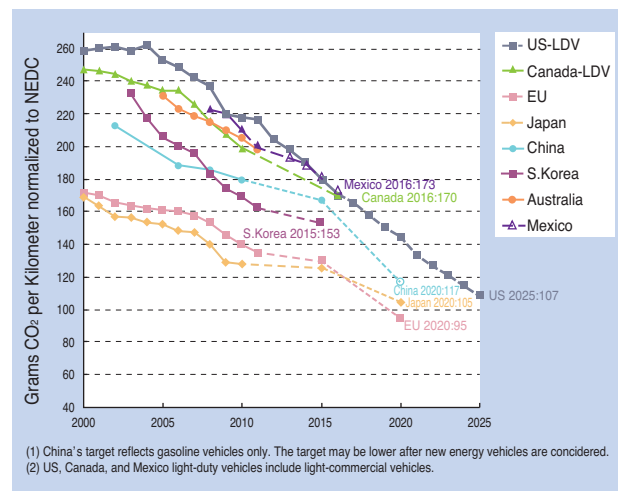


Fig. 8 Mileage regulation of key regions (CO2 emissions, g/km)³⁾

other hand, it is expected that the load on the belts, pulleys (bearings) and auto tensioners of accessory drive belt system will increase because of the increase in variation of crank rotation and accessory belt tension as the number of engine cylinders is reduced.

With the continuing technology development for lower fuel consumption, a comprehensive optimization of the entire accessory belt drive system will become critical. This is especially the case when applying associated technologies such as hybrid systems, downsized turbocharged engines, and a 48V power supply.

5. Conclusion

In this paper, we have discussed the technological trends of accessory drive belt systems and introduced the **NTN** products to be used with those systems; auto tensioners and various pulleys.

Since the regulations for fuel consumption are becoming stricter in key regions, the demand for lower fuel consumption will further increase. In order to respond to these requirements, **NTN** will address the diversified market needs, based on the desirable form of the entire accessory drive belt system through continued development of our auto tensioners and pulleys.

Reference

- 1) Seiji SATO, Technology Trends in Auto Tensioners, NTN TECHNICAL REVIEW, 79 (2011) 83-89
- 2) For example, Auto Prove Web home page
- 3) ICCT (International Council on Clean Transportation), 2013

Photo of authors



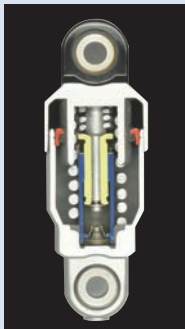
Ayumi AKIYAMA
Application Engineering Dept.
Automotive Business HQ



Hiroo MORIMOTO
Automotive Product Design Dept.
Automotive Business HQ

Auto Tensioner with Variable Damper Mechanism for ISG-equipped Engines

Hiroo MORIMOTO*
Yuta MOCHIZUKI**



It is necessary to set the belt tension rather higher than usual to prevent the belt from slipping at the time of the engine restarting when we applied a conventional auto tensioner to the accessory drive belt of the engine equipping with ISG and it causes harm for millage improvement.

This paper introduces the new developed variable damper auto tensioner which contributes to the mileage improvement of the ISG-equipped car.

1. Introduction

Currently, all motor vehicles are being required to address a number of environment protection and resource saving concerns. An increased number of vehicles are being equipped with an idling stop mechanism as one of the means for improving fuel economy of the conventional internal combustion engine vehicle (Fig. 1). This trend is expected to continue, and the method of restarting the engine is shifting to the integrated starter generator (ISG). This is a belt driven method where the crankshaft is driven by the accessory belt from the alternator. This engine restarting method is characterized by quick engine restarting time and quiet operation, compared with using the traditional starter motor.

For the accessory drive belt system of most vehicles (Fig. 2), an auto tensioner is used to maintain an adequate belt tension. This prolongs the life of the belt and accessory systems and also prevents vibration and noise due to belt slippage¹⁾. To effectively reduce vibration of belt, the auto tensioner is usually placed at the lower tensioned area of the belt when the engine is operating, namely, after the crank pulley (driving side). However, when using the ISG method for idle stop, the auto tensioner must be set at the area where the belt is in high tension when the engine restarts, namely, before the ISG pulley. Since the areas of high tension and low tension switch

between steady driving and engine restarting, auto tensioners used with ISG systems are required to have new functions.

In order to respond to these requirements, NTN has developed a new “variable damper auto tensioner for ISG-equipped engines” for the accessory drive belts of vehicles with this feature.

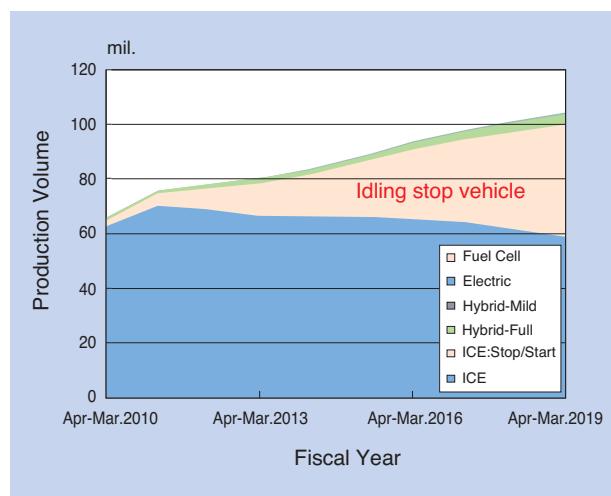


Fig. 1 Trend of automotive propulsion system²⁾

*Automotive Product Design Dept. Automotive Business HQ

**Functional Experiment Dept. Automotive Business HQ

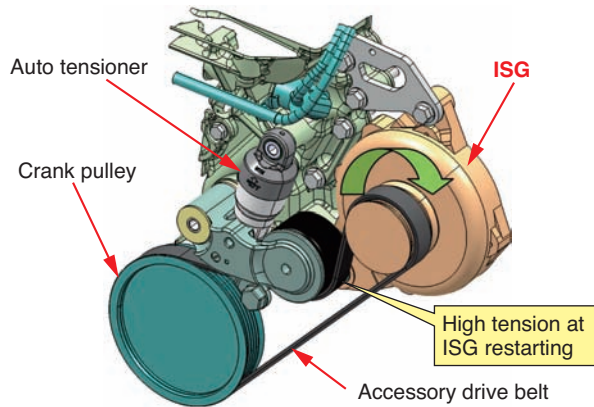


Fig. 2 Accessory belt drive system

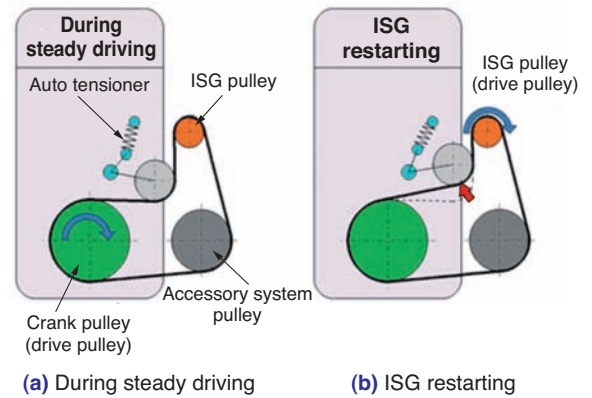


Fig. 3 Figure of FEAD layout

2. Characteristics of engines adopting the belt driven ISG method

Fig. 3 shows a diagram of a typical accessory system layout of a vehicle engine. Fig. 3 (a) shows the system status under steady driving conditions. During this state, the crank pulley is the driving pulley. Since the crank rotation speed changes due to the combustion process of each cylinder, the belt tension fluctuates at the frequency of engine rotation $\times (1/2) \times$ number of cylinders. By minimizing the reaction force generated with this fluctuation of the belt tension (hereinafter, tensioner reaction force), we can reduce the average belt tension, increasing the life of the belt and accessory systems, as well as, improving fuel economy by reduction of friction losses. In other words, the smaller the tensioner reaction force to the belt, the more desirable.

On the other hand, Fig. 3 (b) shows the system status when the engine is restarting (hereinafter, ISG restarting). The ISG pulley acts as the driving pulley to turn the stopped crank pulley through the belt. At the moment of ISG restart, the belt tension between the ISG pulley and the crank pulley suddenly increases. As a result, the auto tensioner is deeply pushed in, creating lower tension. Therefore, the tensioner reaction force must typically be set at a higher set value to avoid belt slippage.

It seems then, that auto tensioners in engines equipped with an ISG are required to provide conflicting functions; low tensioner reaction force during steady driving and sufficient tensioner reaction force to avoid slip during ISG restarting.

3. Variable damper auto tensioner for ISG equipped engines

3.1 Structure

Fig. 4 and 5 show the cross-sections of the conventional product and the new variable damper auto tensioner for ISG equipped engines (hereinafter, developed product), respectively. The main feature of the developed product is the ability to switch the tensioner reaction force according to driving conditions with a simple mechanism and without use of electrical control, etc.

The conventional product creates a pressure chamber and leak gap with the valve sleeve and rod. Along with the extension/compression of the auto tensioner, the rod is pushed in/out against the valve sleeve.

For the conventional product, the hydraulic tensioner reaction force is generated by elastic deformation of oil in the pressure chamber and flow resistance as oil passes this leak gap.

The developed product has a pressure chamber and two leak gaps created by the valve sleeve, plunger and rod. We can describe the radial gap between the outer diameter of the rod and the inner diameter of the plunger as the first leak gap. The radial gap between the outer diameter of the plunger and the inner diameter of the valve sleeve is the second leak gap. In addition, a second check valve is formed by the rod, plunger, retaining ring and switch spring. The second check valve is open when the pressure in the pressure chamber is low, since the plunger is pushed toward the pressure chamber by the switch spring. The tensioner reaction force generated is adjusted by the opening/closing and the size of two leak gaps.

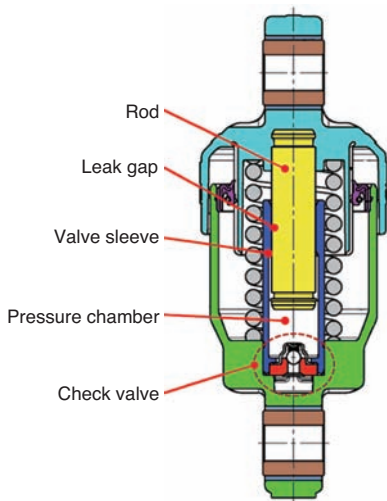


Fig. 4 Structure of conventional product

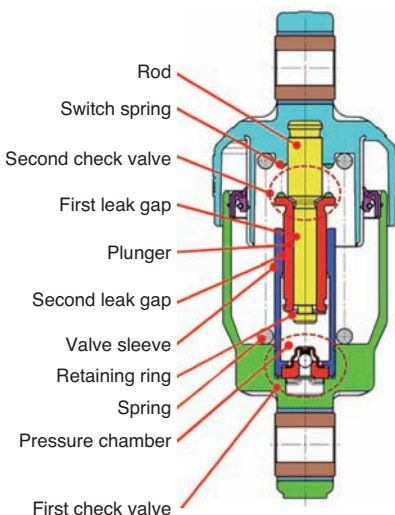


Fig. 5 Structure of development product

3.2 Operation principle

Fig. 6-8 illustrate the relationship between the change in length of the auto tensioner and the resulting tensioner reaction force when the developed product is extended/shrunk at an amplitude equivalent to that of ISG restarting conditions. The graphs shown in the right side of each diagram are called Lissajous patterns. The Lissajous patterns of the developed product can be divided into three regions according to the operational conditions. The following is the description of the internal operation of the auto tensioner for each region:

(1) Region where the auto tensioner shrinks and the reaction force increases (Fig. 6)

In this region, the auto tensioner starts shrinking from its most extended condition. As the auto tensioner shrinks, the rod and plunger move into the

valve sleeve. As the plunger is pushed by the switch spring, it is fixed to the tip of the rod contacting the retaining ring, moving with the rod. The pressure of the pressure chamber increases as the oil in the pressure chamber is compressed, and the oil leaks from the pressure chamber via the first leak gap between the outer diameter of the rod and the inner diameter of plunger, and through the second check valve. The second check valve remains open as the pressure in the pressure chamber is still lower than the force of the switch spring pushing the plunger.

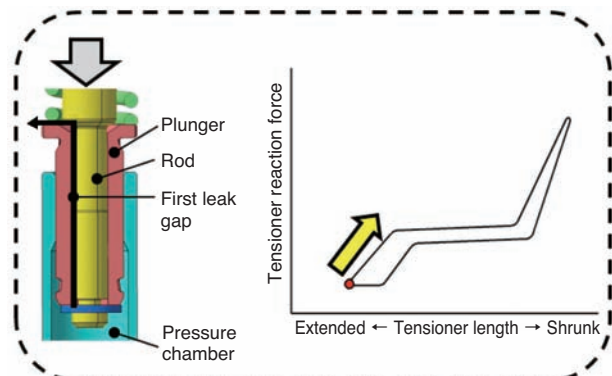


Fig. 6 Region where auto tensioner shrinks and reaction force increases

(2) Region where the auto tensioner shrinks, yet the reaction force remains mostly unchanged (Fig. 7)

In this region, the force of the switch spring pushing the plunger is balanced with the pressure in the pressure chamber. Therefore, only the rod moves, into the valve sleeve as the auto tensioner shrinks, and the change in the pressure chamber volume is smaller. As the pressure continues to increase, the switch spring gradually shrinks, maintaining the balanced condition. When the compression of the switch spring reaches the stroke of the second check valve, the second check valve closes.

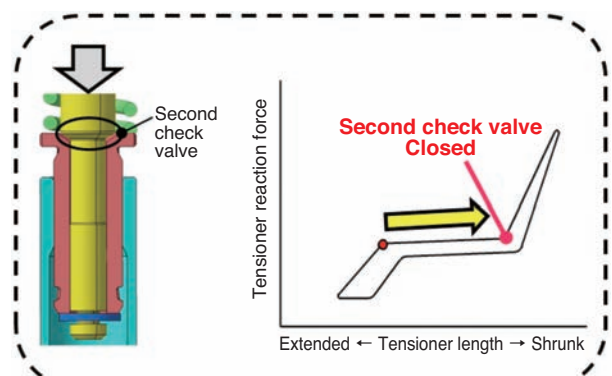


Fig. 7 Region where auto tensioner shrinks but reaction force remains unchanged

(3) Region where the auto tensioner shrinks and the reaction force increases again (Fig. 8)

In this region, the pressure in the pressure chamber exceeds the force of the switch spring pushing the plunger. Therefore, the second check valve closes and the plunger moves into the valve sleeve with the rod. At the same time, the pressure of the pressure chamber is increasing and the oil leaks from the second leak gap formed by the outer diameter of the plunger and the inner diameter of the valve sleeve.

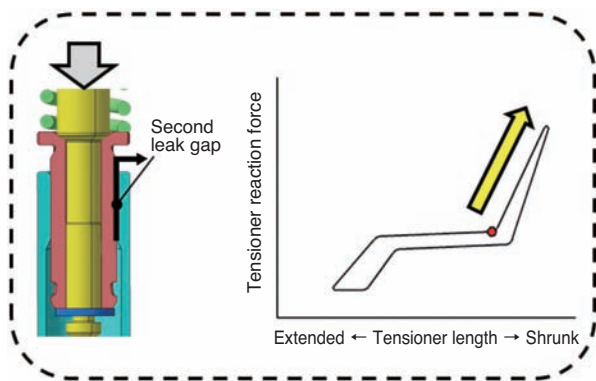


Fig. 8 Region where auto tensioner shrinks and reaction force increases again

4. Achieving the ideal damper property

4.1 Comparison of properties between the conventional and developed products

With the conventional product, the conflicting properties, that is, the reduction of belt tension during steady driving and addition of relatively large belt tension at ISG restarting, cannot be simultaneously achieved.

(1) Belt tension adjustment by the conventional product during the steady driving

Fig. 9 shows the Lissajous pattern considering steady driving conditions. During steady driving conditions, since the fluctuation of the belt tension is small, the extension range of the auto tensioner is also small. Therefore, the tensioner reaction force generated by the extension/shrinkage is small with the conventional product designed for low belt tension (low reaction force spec.). On the other hand, with the conventional product designed for high belt tension required for ISG restarting (high reaction force spec.), the tensioner reaction force becomes large even if the amplitude of the auto tensioner is small. Therefore, the belt tension becomes unnecessarily large,

resulting in adverse fuel economy effects due to increased friction.

(2) Belt tension adjustment with the conventional product during ISG restart

Fig. 10 shows the Lissajous pattern considering the amplitude that occurs during ISG restarting. At ISG restart, since the belt tension instantly increases, a large tensioner reaction force is required.

The conventional product with high reaction force specifications can ensure the belt tension required for ISG restarting, not allowing any belt slippage. However, the conventional product with low reaction force spec. cannot ensure the belt tension required for ISG restart, as the tensioner reaction force is insufficient, likely leading to slippage between the belt and pulleys.

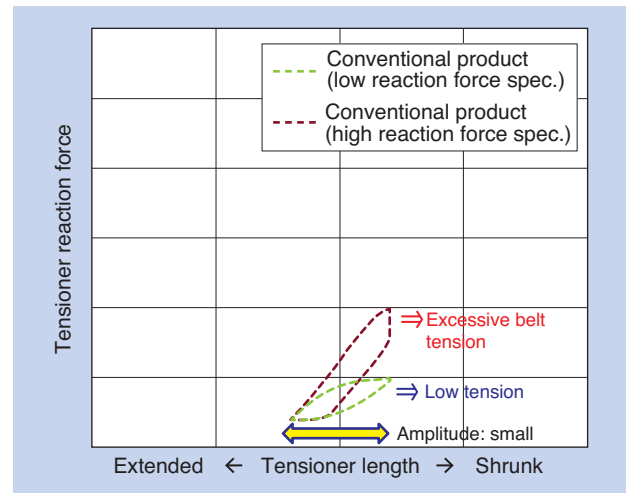


Fig. 9 Lissajous pattern during steady driving (conventional product)

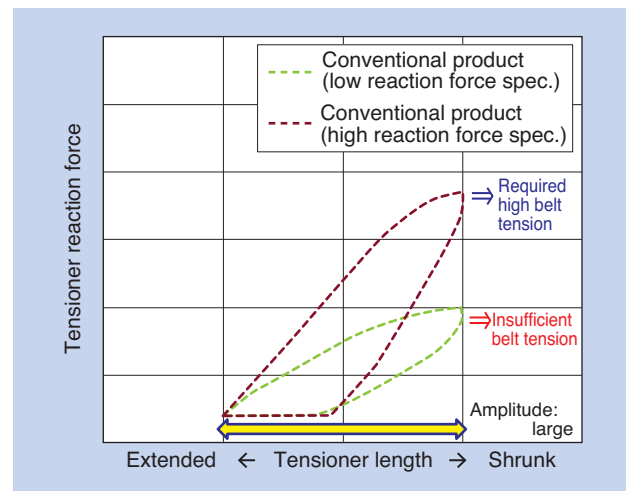


Fig. 10 Lissajous pattern at ISG restarting (conventional product)

(3) Belt tension adjustment with the developed product

Fig. 11 shows the Lissajous pattern of the developed product. The tensioner reaction force can be maintained low during steady driving, similar to the conventional product with low reaction force spec. However, during ISG restarting, a large tensioner reaction force can be instantly generated similar to the conventional product with high reaction force spec.

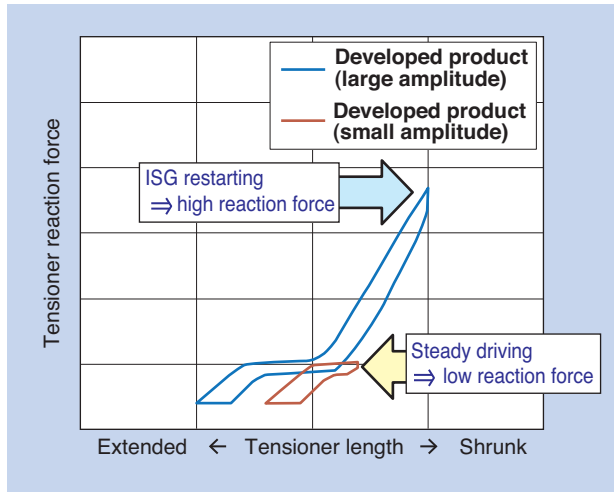


Fig. 11 Lissajous pattern of developed product

4.2 Verification of the effect with the actual vehicle

NTN has installed the developed product on an actual vehicle and measured; (1) pulley rotation speed when restarting the engine with the ISG, and (2) tensioner reaction force during steady driving. As a comparison, the conventional product (high reaction force spec.) was also measured.

(1) Restarting the engine with the ISG

Fig. 12 (a) and **(b)** show the measurement results of the developed product and the conventional product (high reaction force spec.), respectively. We have defined the engine restarting point as the moment when the crank pulley rotation speed starts stabilizing, and we compared the time from the moment the ISG pulley rotation started until the engine restarting point.

From the test, the time until the engine restarting point was not later than the conventional product with high reaction force spec. and the correct ISG restarting was verified. During the measurement, no belt slippage occurred.

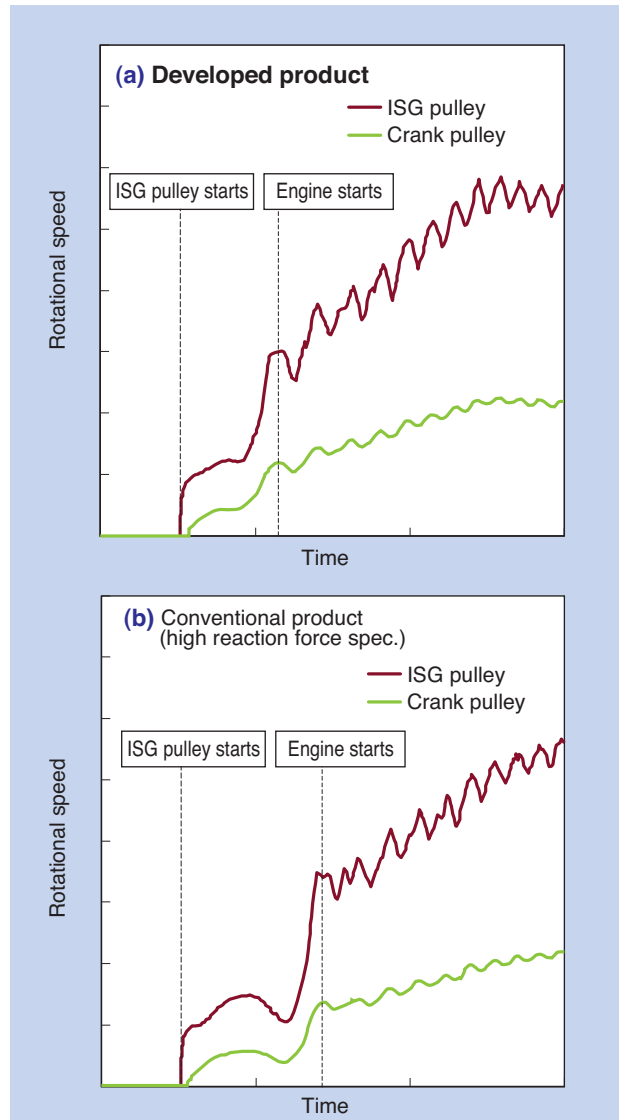


Fig. 12 Measurement results of pulley rotational speed at ISG restarting

(2) Auto tensioner reaction force during steady driving

Fig. 13 shows an example of the auto tensioner reaction force measurement results at a certain rotation speed of the engine. Graph **(a)** shows the results of the developed product when installed on an actual vehicle and **(b)** shows the results of the conventional product (high reaction force spec.). The developed product reduced the maximum value of the tensioner reaction force by around 50% compared with the conventional product. From this, we can expect an improvement of fuel economy through reduction of tension on the accessory belt.

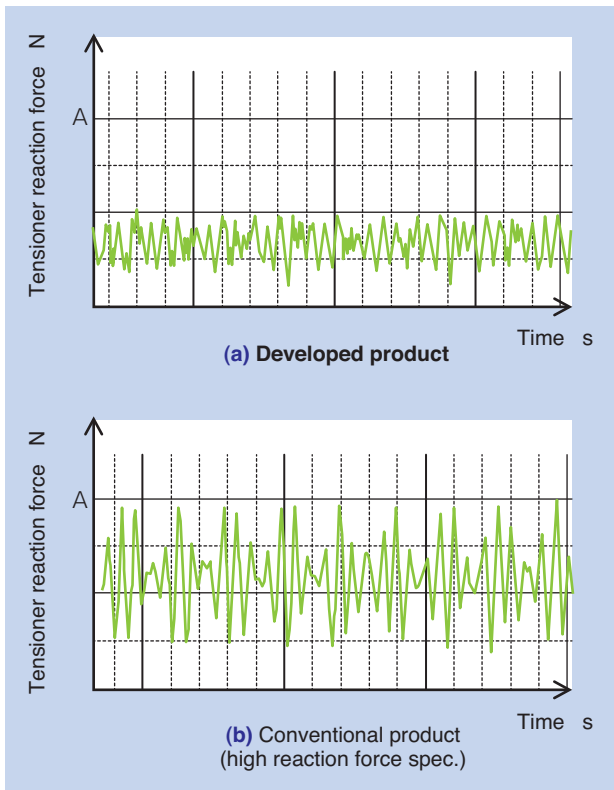


Fig. 13 Measurement results of tensioner reaction force during steady driving

5. Conclusion

NTN has developed a variable damper auto tensioner for use on ISG equipped engines that can automatically adjust the accessory belt tension according to the driving conditions. NTN has verified the developed product’s effectiveness by testing it on an ISG equipped engine. When the developed product is installed, the starting time of the crank pulley is about the same as the conventional product with high reaction force spec. At the same time, the tension of the accessory belt can be reduced up to 50% during steady driving, with which an improvement of fuel economy can be expected.

As the requirement for improving fuel economy further increases, NTN aims to contribute to global environmental protection by marketing this developed product worldwide.

Reference

- 1) Seiji SATO, Technology Trends in Auto Tensioners, NTN TECHNICAL REVIEW, No. 79 (2011) 83-89
- 2) HIS Data (2014)

Photo of authors



Hiroo MORIMOTO
Automotive Product Design Dept.
Automotive Business HQ



Yuta MOCHIZUKI
Automotive Product Design Dept.
Automotive Business HQ

Products Introduction of Composite Material for Automotive



Kayo SAKAI*

Eiichirou SHIMAZU*

Takahiro GOTOU**

Hajime ASADA**

Takuya ISHII***

NTN group produces sliding bearings, sliding parts and magnetic components, which are manufactured from the composite materials. They are blended powder metal or resin with additives to impart various functions according to our own formula. This article introduces various products made of such composite material used in automotive applications for high mileage and light-weighting.

1. Introduction

NTN is developing/manufacturing composite material products. The products are made by blending various powder additives with resins and metallic powders according to our proprietary blending formula. These products have required characteristics desired by the companies shown in Fig. 1. The composite material products can be made for many applications by combining material powders and blending them. In addition, the powder material can be molded into complex shapes, allowing efficient manufacturing. Because of these properties, NTN is proposing composite material products to a broad range of applications and fields and manufacturers. Examples are sliding bearings made of resin and sintered metal, including fluid hydrodynamic bearings, sliding

components, machine parts such as gears and cams, magnetic components used for sensors, and coil components for electrical noise removal and voltage regulation. In this paper, we introduce composite material products contributing to low fuel consumption, compact size and electrification of vehicles.

2. Low torque seal ring for transmission

Automatic and continuously variable transmissions in vehicles use hydraulic mechanisms to change the velocity of the vehicle. Seal rings are used in the hydraulic circuits of transmissions, installed between the rotating shaft and housing. These are the components that seal oil and maintain pressure within the hydraulic circuit. Then seal rings are pressed to both the housing and shaft by hydraulic pressure and slide against the rotating shaft. Around 4 to 10 resin oil seal rings (hereinafter, seal rings) of 15 – 60 mm outer diameter are used per transmission for sealing oil in the sliding area.

Reduction of the torque of the seal ring means improvement of the transmission efficiency, and reduction of oil leakage means a more efficient and compact hydraulic pump. Both contribute positively to the fuel economy of vehicles. In order to maintain low torque and low oil leakage for a long time, it is necessary to minimize wear of the seal rings and the rotational shafts, which are the mating components on which the seal rings slide.

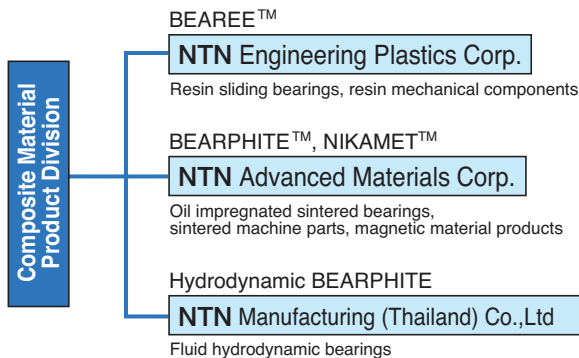


Fig. 1 Composite material products of NTN group

*Composite Material Product Division, Composite Material Product Division

**Engineering Department, NTN Advanced Materials Corp.

***Engineering Department, NTN Engineering Plastics Corp.

NTN has developed “low torque seal rings” which have reduced torque by 60% compared with conventional products. The seal rings have superb properties such as low wear and low oil leakage due to newly developed V-shaped lubrication grooves on the side wall of the PEEK (Polyetheretherketone) resin seal rings^{1), 2)} as shown in Fig. 2. These parts are in mass production..

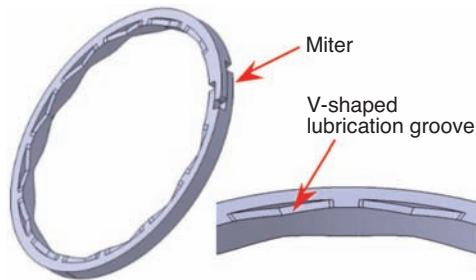


Fig. 2 Groove shape of low torque seal ring

2.1 Features

Typical seal rings have rectangular or trapezoidal cross-sections. Their respective operations are illustrated in Fig. 3. A comparison of the properties of these seal rings with the respective cross section geometries and the developed low torque seal ring are shown in Table 1.

As the rectangular seal rings contact the rotational shaft along the entire side wall, they exhibit low oil leakage and large torque. Conversely, the trapezoidal seal rings have line contact with the shaft resulting in low torque and high oil leakage. Also, they tend to wear faster due to the line contact, resulting in unstable properties.

The low torque seal rings were developed to maintain a superb low oil leakage property, and

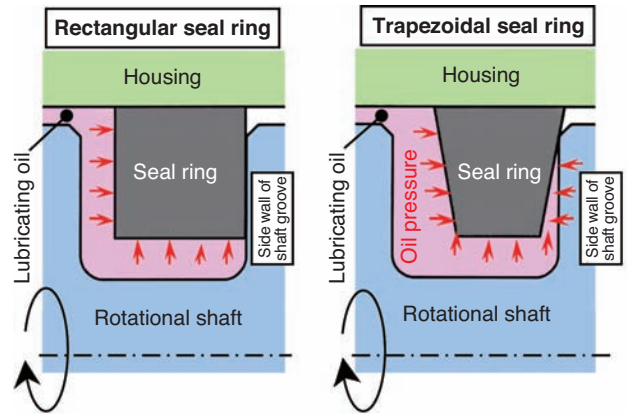


Fig. 3 Operating of seal ring

reduced torque by newly forming the V-shaped grooves on the rectangular seal rings. The low torque seal rings exhibit a balanced performance, providing the following features, compared to the conventional rectangular seal rings.

[Features]

- (1) 60% lower torque
- (2) 10 times better wear resistance
- (3) Equivalent low oil leakage property

The material used is our proprietary material, BEAREE PK5301, which is the PEEK resin blended with special filler, with a long proven track record in this application.

2.2 Performance

Fig. 4 shows the relation between oil pressure and torque. The low torque seal rings have approximately 60 to 70% lower torque than the rectangular seal rings. Dependency on the hydraulic pressure is also relatively low.

Providing V-shaped lubrication grooves on the side

Table 1 Comparison of features of various seal rings

Item	Rectangular seal ring	Trapezoidal seal ring	Low torque seal ring
Cross section	Rectangular	Trapezoidal	Rectangular
Diagram of cross section			
Lubrication groove on side wall	No	No	V-shape
Contact with side wall of shaft groove	Full contact	Line contact	Full contact other than groove
Torque	△	◎~△	○
Oil leakage	◎	△	◎
Wear resistance	○	△	◎
Performance balance	○	△	◎

◎ : Excellent ○ : Good △ : Fair

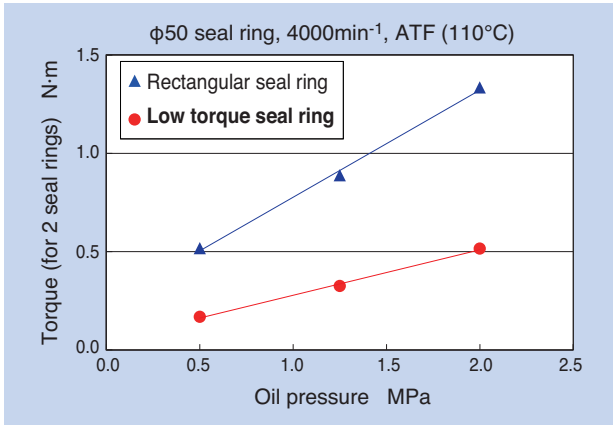


Fig. 4 Torque versus oil pressure

wall of the rectangular seal rings makes the contact area with the shaft groove side wall smaller than the rectangular seal rings. The hydrodynamic effect, where oil pressure increases at the end of the V-shaped grooves, reduces the contact pressure and improves lubrication on the sliding area, achieving low-torque properties. The higher the hydraulic pressure, the more oil enters onto the sliding surface from the lubrication groove; therefore, the torque dependency on hydraulic pressure is considered to be smaller.

In addition, since the lubrication condition on the sliding surface is improved by the V-shaped lubrication grooves, the wear resistance of the low torque seal rings is about 10 times better than the rectangular seal rings.

3. Self-lubricating sliding components

In order to increase visibility of night driving, the adoption of Adaptive Front-lighting Systems (AFS), which directs the headlights axis to the traveling direction, is becoming more popular³⁾. Fig. 5 shows an example of the sliding components for AFS.

With the AFS, sliding materials (bearings) are required for the supporting components of the headlamps. The area inside the headlamp cover becomes very hot due to the heat from the lamp and liquid lubricant or grease on the sliding materials may



Fig. 5 Self-lubricating slide material (for AFS)

evaporate. This leads to contamination in the surroundings, and therefore lubricant and grease cannot be used in this application. New sliding materials that can be used in such dry environment where lubricant cannot be used are needed. NTN is developing self-lubricating, sintered sliding material with improved lubrication by adding a large amount of graphite, which is a solid lubricant.

3.1 Features

Since the bulk density of graphite powder is low, if a large amount is added, the fluidity of the material powder decreases, limiting the shape and size that can be molded. Also, even if the shape can be molded, the processing cycle could become longer, incurring relatively higher cost. The developed self-lubricating sliding material ensures high degree of freedom of shapes and productivity even with the increased level of graphite by increasing fluidity of graphite powder with a special process. This developed material exhibits a superior low friction property and wear resistance, even in the environment where lubricating oil cannot be used.

[Features]

- (1) Superior low friction and wear property in the dry environment
- (2) High degree of freedom for the shape is ensured by the special graphite

The chemical composition of the developed product is shown in Table 2. This product has more than twice the amount of graphite compared with the ordinary bronze based material.

Table 2 Chemical components of developed product

Material	Chemical composition %		
	Cu (copper)	Sn (tin)	C (graphite)
Ordinary bronze base material	Remained	7~11	1~2
Developed product	Remained	7~11	4~7

3.2 Performance

The test conditions for friction and wear properties of the self-lubricating sliding material are shown in Table 3, and the test results are shown in Table 4. The friction coefficient of the developed product is about half of the ordinary bronze based material without oil content, and the wear resistance is increased up to about 40 times of the ordinary bronze based material.

Table 3 Test conditions for friction and wear property

	(1) Friction test	(2) Wear test
Load N	98	15
Rotational speed min ⁻¹	1000	450
Test piece size (mm) (ID x OD x width)	φ6×φ12×6	←
Mating material	SUJ2	SUS420
Test time min	90	60
Lubrication condition	No oil content (dry)	←

Table 4 Specific wear rate and friction coefficient

	Developed product	Ordinary bronze based material
(1) Friction coefficient	0.2~0.3	0.45
(2) Specific wear rate m ³ / (N·m) × 10 ⁻¹²	0.08	3.56

4. Choke coil for high frequency application

In recently produced electrified vehicles, many power supply systems, such as DC/DC converters and inverters, are installed. Choke coils are used to reduce the noise content, added mainly to the direct current, for higher efficiency of these power supply systems. Choke coils are also a measure against radio frequency interference to the peripheral equipment. The vehicle systems tend to be driven by higher frequencies for the purpose of achieving higher efficiency and more compact power supplies; therefore, choke coils are required to maintain stable properties for high frequency bandwidth with low loss.

Fig. 6 shows a toroidal choke coil as an example of choke coils. Choke coils are composed of soft magnetic material, called the core, and conductor wire wound around the core. Choke coils store electrical energy as magnetic energy and prevent current flow of increasing frequencies as stored energy increases⁴. Choke coils use these properties to filter high frequency noise. NTN develops choke coils of various shapes.

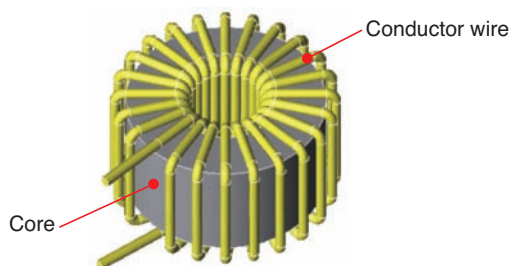


Fig. 6 Toroidal choke coil

4.1 Features and performance

Fig. 7 shows the choke coils made with amorphous alloy powder developed by NTN. NTN's AL60 compression molding core⁵ and AS10 injection molding core⁵ can be used in various shapes not only for toroidal type but also pot type and EER type.

Fig. 8 shows the relation between frequency and permeability of various soft magnetic materials used in choke coils. Permeability is an index that indicates the conversion capability between electrical power and magnetic power. If permeability decreases, noise reduction effect decreases. Therefore, it is desirable that permeability remain the same with increasing frequency. Comparing the frequency at which permeability reduces 10% for each material, an ordinary ferrite core is around 6 kHz and a Fe-Si compression molded core is around 2 MHz. NTN's AL60 compression molded core is around 5 MHz, and NTN's AS10 injection molded core is around 10 MHz, exhibiting a stable noise reduction effect in a high frequency bandwidth more than twice that of the conventional material.

The magnetic energy which can be stored in the core is determined by the saturation magnetic flux density, which is dependent on the material of the core and the core volume. Therefore, for designing the core, material

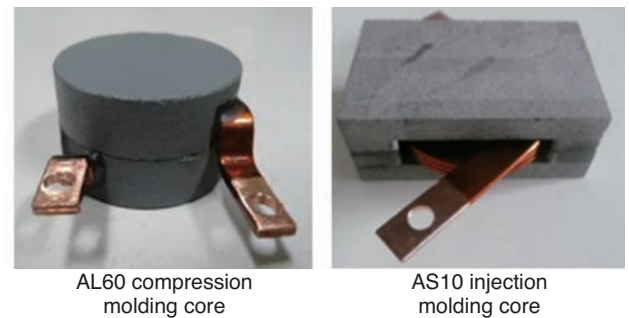


Fig. 7 Various choke coils

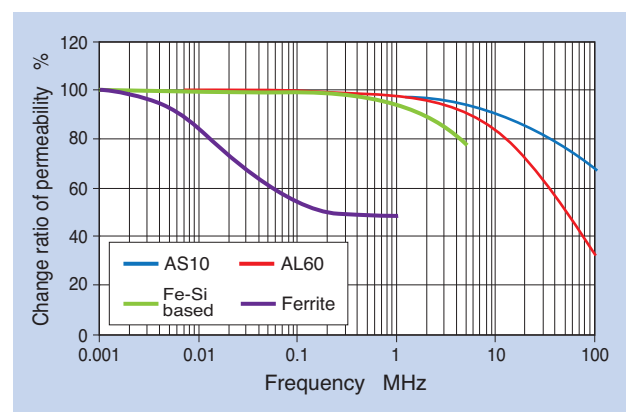


Fig. 8 Frequency response of magnetic permeability

and shape must be determined so that the operating condition does not exceed the energy that can be stored. The condition that exceeds the energy that can be stored in the core is called magnetic saturation, and when magnetic saturation occurs the coils do not function as choke coils. Fig. 9 shows the relationship between magnetizing force and magnetic flux density (B-H curve). When saturation magnetic flux density is high, storage capacity of magnetic energy is high, and the core can be made to have a small volume. Fe-Si based compression molded core, which has a large saturation magnetic flux density, is often used for applications with large current.

Fig. 10 shows energy losses in different cores during electrical energy to magnetic energy conversion. Fe-Si based compression molded cores have larger core losses than the ferrite core and the efficiency is inferior to the ferrite core. NTN's AL60 compression molded core and AS10 injection molded core have small core losses. Particularly the AL60 compression molded core has an excellent low core loss property equivalent to the ferrite core.

Based on these points, AL60 compression molding core and AS10 injection molding core have excellent

frequency response, large saturation magnetic flux density and low core losses; therefore, they can make compact and low-loss high frequency choke coils.

4.2 Composite core

NTN's AL60 compression molded core has a large saturation magnetic flux density and particularly small core losses. On the other hand, the AS10 injection molded core has highly stable permeability in high frequencies and a high degree of freedom for design because it is injection molded. By taking advantage of these properties, cores using either of the two types of materials, or composite cores combining both materials, are designed. The cores are designed depending on parameters like current value and size, as shown in Fig. 11. By this approach, more efficient and compact power supplies can be expected.

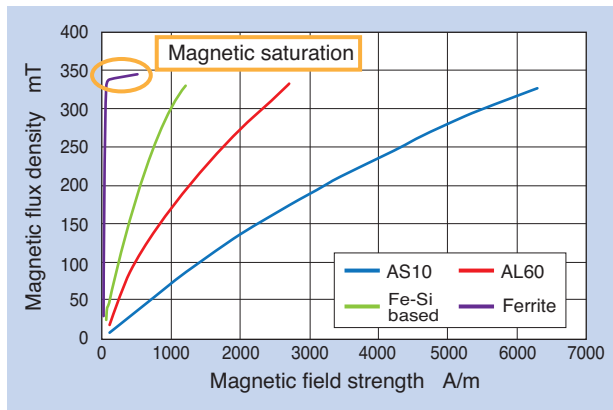


Fig. 9 B-H curve

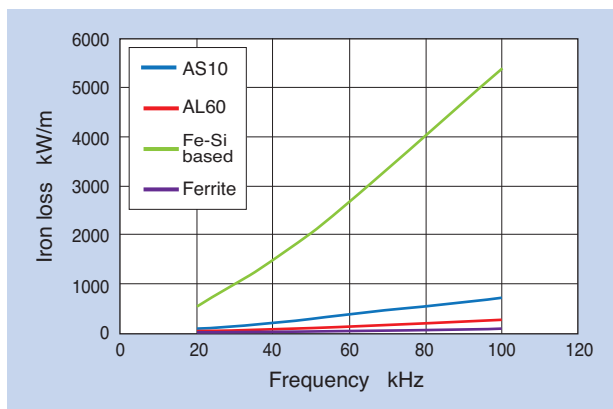


Fig. 10 Core loss characteristics (50 mT)

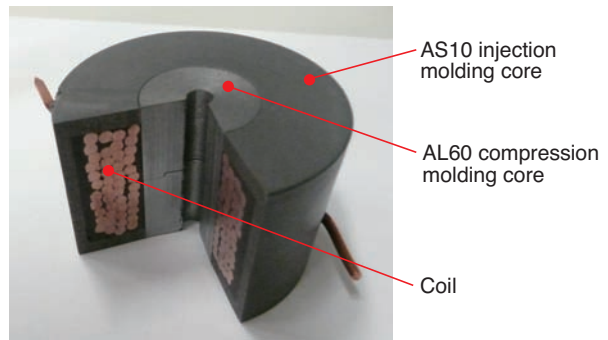


Fig. 11 Composite core

5. Conclusion

In this paper, we have introduced recent composite material products contributing particularly to higher fuel economy, compact size and electrification of vehicles.

Various new technologies are being rapidly developed and proposed in the automobile industry, in addition to electrification, compactivity and high fuel economy. We are aiming for continuous product development and propositions responding to the new requirements in the automotive industry, by advancing and integrating composite material technologies.

Reference

- 1) Yutaka HAYASHI, Jiro MATSUMOTO, Noboru UMEMOTO: Introduction of Engineering Plastic Seals, NTN TECHNICAL REVIEW No. 65 (1996) 54.
- 2) Yoshio OKI, Takumi HAYASHI, Takuya ISHII: Characteristics and Applications of Super Engineering Plastics, Journal of Japanese Society of Tribologists 49 (7), (2004) 31
- 3) Automotive Technology Handbook Editing Committee Planned/Edited: Automotive Technology Handbook 2.
- 4) Jiro TOGAWA, Coil/Transformer Design of Switching Power Supply
- 5) Takayuki ODA, Shinji MIYAZAKI, Eiichiro SHIMAZU: The Reactor Core for HEV Boost Converter, NTN TECHNICAL REVIEW No. 81 (2013) 46-51.

Photo of authors



Kayo SAKAI
Composite Material
Engineering Dept.
Composite Material Product Division



Eiichirou SHIMAZU
Composite Material
Engineering Dept.
Composite Material Product Division



Takahiro GOTOU
Engineering Department
NTN Advanced Materials Corp.

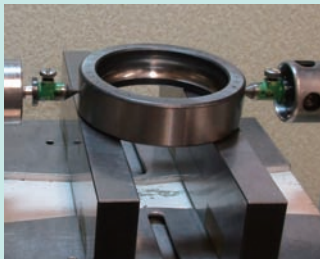


Hajime ASADA
Engineering Department
NTN Advanced Materials Corp.



Takuya ISHII
Engineering Department
NTN Engineering Plastics Corp.

Modeling of Retained Austenite Transformation in Bearing Steels



Christine SIDOROFF*
Pierre DIERICKX*
Pr. Michel PEREZ**

Bearing steels are heat treated to obtain martensitic microstructures providing high hardness necessary for good rolling contact fatigue performance. If specific actions are not taken, austenite is generally retained after heat treatment in the final component with a more or less important content. Depending on the requirements of each application, retained austenite can be desired because of beneficial effects such as improvement of rolling contact fatigue performance, mostly in contaminated lubricating conditions, or can be avoided if dimensional stability is needed for example in cases of bearings operating for long durations at high temperatures. This paper discusses the modeling of retained austenite transformation and its dimensional consequences in SUJ2, taking into account all the phase evolutions occurring during tempering and in service.

1. Introduction

To attain long service lives, bearing ring materials are selected to provide a minimum hardness of 58 HRC for rolling contact fatigue (RCF) resistance (in conjunction with the appropriate inclusion cleanliness), and a good wear resistance by choosing the appropriate steel grade, steelmaking process, and heat treatment.

If no specific requirements such as structural fatigue or impact resistance are expressed, through-hardened steels are used, such as SUJ2 steel in the case of standard temperature conditions (hereafter mentioned as standard bearing steels).

Another important feature that bearing steels must retain in service through the life of the mechanical component is the initial internal clearance of the bearing, and its interference with the surrounding parts. Therefore, the dimensional change must be limited at the service temperature for standard bearing steels by selecting the appropriate heat treatment.

Steels such as SUJ2 are easily hardened to the required level, by austenitizing at temperatures above AC_1 , quenching and tempering. The metallurgical structures obtained after hardening are not stable and will evolve in service towards more stable states, resulting in size changes or dimensional instability.

The main non-stable phase often associated to these evolutions is retained austenite, remaining in high-carbon alloyed steels' microstructure after quench.

These phenomena have been extensively described in existing publications, but the purpose of this paper is to explain the complex metallurgical mechanisms behind the dimensional instability, and to present work realized in NTN-SNR to estimate the relative contributions of the different individual phenomena in order to build a model to predict dimensional variations occurring during service.

*NTN-SNR Roulements, Technology and Innovation Department

**Institut National des Sciences Appliquées de Lyon, MATEIS Laboratory

2. Metallurgical phenomena and their dimensional consequences

2.1 Metallurgical phenomena

After austenitizing and quenching, the microstructure of SUJ2 is mainly martensitic, and composed of the following constituents:

- Martensite, with a high carbon concentration above the equilibrium carbon content in ferrite;
- Retained austenite, not transformed at room temperature after quench because of the alloying elements and carbon concentration,
- Undissolved carbides, not fully dissolved during austenitizing.

These two first constituents, martensite and retained austenite, are metastable and evolve in service towards a more stable state.

Martensite tempering is often described using the following stages associated with temperature ranges in which they are likely to take place^{1, 2)}. These phenomena can happen at lower temperatures, provided time is left for these transformations to occur.

Stage 0 ($T < 100^\circ\text{C}$)

Carbon atoms segregate to dislocations (it can represent up to 0.2 wt.%C).

Stage 1 ($100 < T < 200^\circ\text{C}$) $\alpha' \rightarrow \alpha'' + \varepsilon$

Carbon leaves the oversaturated martensite ($\alpha' \rightarrow \alpha''$), and creates metastable ε -carbides ($\text{Fe}_{2.4}\text{C}$).

Stage 2 ($200 < T < 300^\circ\text{C}$) $\gamma_R \rightarrow \alpha + \text{Fe}_3\text{C}$

Retained austenite (γ_R), also a metastable phase, decomposes into a mix of ferrite (α) and cementite (Fe_3C).

Stage 3 ($250 < T < 350^\circ\text{C}$) $\alpha'' + \varepsilon \rightarrow \alpha + \text{Fe}_3\text{C}$

Carbon leaves the impoverished martensite ($\alpha'' \rightarrow \alpha$) to form cementite carbides (Fe_3C) to the detriment of ε -carbides.

Stage 4 ($T > 350^\circ\text{C}$)

Carbides coarsen and spheroidize. The structure is subjected to recovery, and then recrystallization.

To summarize, two different phenomena occur during the first stages of tempering: precipitation of carbides from martensite (stage 0 + stage 1 + stage 3), and transformation of retained austenite (stage 2).

2.2 Dimensional consequences

These phase evolutions and transformations produce macroscopic dimensional variations^{3, 4)}.

Precipitation from martensite

Martensite has a tetragonal lattice, and its parameters are dependent on carbon concentration⁵⁾.

- When carbon is rejected from martensite and carbides precipitate, two opposite effects take place:
- Contraction of the martensite because of lattice size reduction (tetragonal loss and volume reduction of lattice cell);
 - Slight expansion because of carbide formation, not high enough to compensate for the contraction previously mentioned.

These two effects result in a continuous contraction, as long as carbon precipitates into ε -carbides, and Fe_3C carbides.

Transformation of austenite

Austenite has a face-centered cubic (fcc) structure, which is the densest existing structure. When it transforms into ferrite and cementite, the volume increases.

Fourth stage

Carbide coarsening and spheroidizing, recovery and recrystallization result in a macroscopic contraction, rarely referred to in technical publications.

For as-quenched martensitic microstructures, during thermal aging, the dimensional evolution shows a succession of contraction (carbon rejection and ε -carbide precipitation), expansion (austenite decomposition) partially compensated by cementite precipitation, contraction (end of cementite precipitation), and again contraction with a slight change in slope (structure evolutions during the fourth stage). This succession of events is represented in **Fig. 1** for an anisothermal aging of SUJ2 steel obtained by differential dilatometry with a heating speed of $5^\circ\text{C}/\text{min}$. The same succession can be observed for isothermal aging, if tested times are long enough.

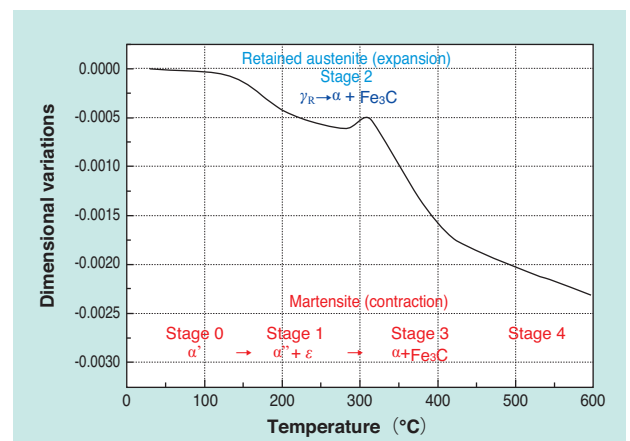


Fig. 1 Anisothermal aging of as quenched SUJ2

3. Analysis and modeling of the dimensional evolutions during isothermal aging of SUJ2

An original approach to the study of dimensional stability of SUJ2 has been conducted by NTN-SNR⁽⁶⁻⁸⁾ using Thermoelectric Power (TEP) measurements. The aim of the study was to predict the macroscopic dimensional variations as a function of a thermal aging, based on calculations of each microstructural contribution. This work comprises two stages:

- Quantification of volume fraction and carbon content of each microstructural constituents through TEP measurements as a function of aging time and temperature,
- Use of these data as input for calculations of dimensional variations of each contribution, and an average calculation to obtain the macroscopic dimensional variation.

3.1 Thermal treatments studied

The study was conducted on samples heat treated according to the cycles of Table 1. A standard as-quenched martensitic heat treatment (referred to as H) was studied as well as a similar state followed by a subzero treatment (referred to as HF) to destabilize a part of the retained austenite (F as ‘freeze’ was added to the name of the sample).

X-Ray Diffraction (XRD) was used to determine the initial retained austenite contents, on cylinder-shaped samples (according to Fig. 2).

Table 1 Thermal treatments performed on SUJ2⁽⁶⁾

	Martensitic thermal treatment	
	H	HF
Austenitizing	850°C / 15min	850°C / 15min
Quench / isothermal holding	Oil	Oil
Water rinsing	60°C / 5min	60°C / 5min
Subzero treatment	–	-80°C / 1h
Initial retained austenite content (vol.%)	10.3	4.7

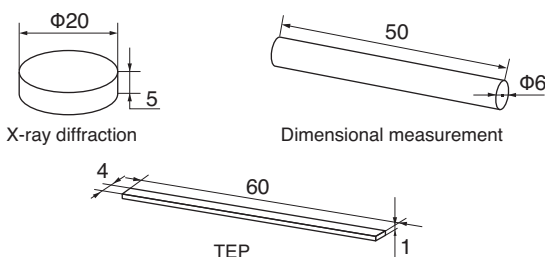


Fig. 2 Samples used for X-Ray diffraction, TEP and Dimensional measurements

3.2 Use of TEP to the study of phase evolutions during aging of SUJ2

Thermoelectric power measurements have been used to follow the kinetics of carbon precipitation from martensite. The principle of TEP is to apply to the studied steel specimen a temperature gradient between its two extremities by contact with two pure copper blocks, and to measure the resulting voltage induced by the Seebeck effect between the two junctions. TEP is sensitive to the crystal defects influencing electron diffusion and phonon propagation, such as atoms in solid solution, and is therefore an interesting tool to characterize and quantify precipitation of carbides from oversaturated martensite during thermal aging.

Samples of rectangular shape according to Fig. 2 treated according to Table 1 were aged at different temperatures from 110°C to 505°C to durations up to 300h. Aging was interrupted at logarithmic increasing time steps to obtain the TEP evolution for each sample at room temperature, expressed as the TEP variation ΔS between the initial state (as quenched) and aged at considered time (Fig. 3).

ΔS increases in two consecutive sigmoidal steps, identified in Fig. 3 as A and B, associated to the precipitation of carbon from oversaturated martensite, into metastable ϵ -carbides, and Fe₃C (to the detriment of ϵ -carbides), respectively. These stages occur sooner when temperature increases, based on the time-temperature equivalence presented later. At high temperature and times, ΔS continues to increase linearly, in step C, and is assumed to be caused by the phenomena occurring during the fourth stage of tempering: recovery of the dislocation structure,

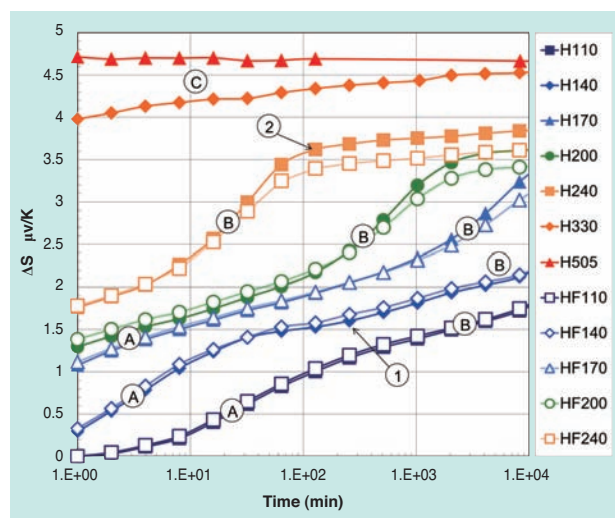


Fig. 3 TEP evolution of the martensitic heat treatment as a function of time at different aging temperatures, with (HF) and without (H) subzero treatment – H110 stands for H treatment⁽⁶⁻⁸⁾

recrystallization, and the coarsening of carbides.

Subzero treated HF samples, with a lower initial retained austenite content compared to H samples, present during stage B a slightly lower ΔS . This difference is assumed to be linked to the decomposition of retained austenite that seems to occur simultaneously to the precipitation of Fe_3C carbides.

As increasing temperature seems to shift the curves towards shorter times, the results were treated with a time-temperature equivalence according to an **Arrhenius law**⁷⁾, to transfer measurements of all times and temperatures to equivalent times at 110°C, the lower aging temperature investigated, using activation energies of 120 kJ/mol for temperatures between 110 and 240°C, and 190 kJ/mol for higher temperatures (close respectively to the values for carbon precipitation during tempering of martensite, and for recovery in α -iron).

These master curves (given for H samples in **Fig. 4**) were then used to estimate the **evolution of volume fraction and carbon content** of the different constituents of the microstructure, through their individual contribution to TEP evolution, according to the following scenario:

- Stage A: ε -carbides are precipitated from the carbon rejected from the oversaturated martensite.
- Stage B: Fe_3C carbides precipitate using the carbon segregated on dislocations, the carbon remaining in solid solution in martensite, and released from the decomposition of ε -carbides that dissolve because they are less stable than Fe_3C . Simultaneously,

retained austenite decomposes into a mix of ferrite and cementite.

- Stage C: Recovery of dislocation structure and coarsening of martensite laths occur.

Based on these assumptions and scenarios, an analytical approach was built, using Johnson-Mehl-Avrami-Kolmogorov⁷⁾ (JMAK) empirical formulae for the kinetics of the precipitation of ε -carbides and Fe_3C , and for the recovery of dislocations and lath coarsening.

The macroscopic TEP is considered to be the volume average of the two individual contributions to TEP of the martensitic phase (the variation of carbon in solid solution in the martensite, and the recovery), and of the retained austenite. The TEP master curves of H and HF heat treatments as a function of equivalent time at 110°C were then used to adjust a number of parameters while others were measured or gathered from publications⁷⁾. The interpolated parameters were all confronted to values available in the literature and found to be in agreement with them⁷⁾, and the interpolated TEP curves fit quite well with the experimental data (**Fig. 4**).

3. 3 Estimation of macroscopic dimensional variations

The macroscopic dimensional variations can be calculated from the individual contributions of each phase, as far as the microstructure of SUJ2 can be understood as a composite material. This can be achieved either through the use of simple models, where the minimal and maximal value of dimensional variations were estimated by averaging the stresses (uniform strain – Voigt) or the strains (uniform stress – Reuss) in the volume, either with more complex approaches such as self-consistent model or Ponte Castaneda-Willis (also called homogenization techniques), that take into account the morphology and relative layout of the phases, and their mechanical interactions.

For a given time and temperature, it was then possible to estimate the macroscopic dimensional variation limits (here using Voigt and Reuss models for ease of understanding). Carbon concentrations in the different phases and the fraction of decomposed retained austenite are the main input parameters of this model (for detailed expressions, see⁷⁻⁸⁾). The experimental measurements, realized on long cylinder-shaped samples (according to **Fig. 2**), are in good agreement with the estimations (**Fig. 5**).

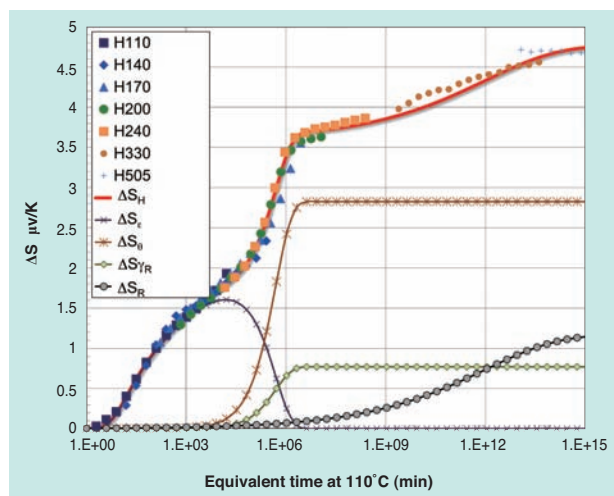


Fig. 4 Experimental (dots) and modeled (curves) TEP evolution for martensitic heat treatment H: macroscopic TEP evolution (ΔS_H) and individual contributions to TEP evolution (ΔS_ε , ΔS_θ , ΔS_{γ_R} , ΔS_R) as a function of equivalent time at 110°C⁶⁻⁸⁾ – H110 stands for H treatment aged at 110°C, ε for ε -carbides, θ for cementite, γ_R for retained austenite, R for Recovery

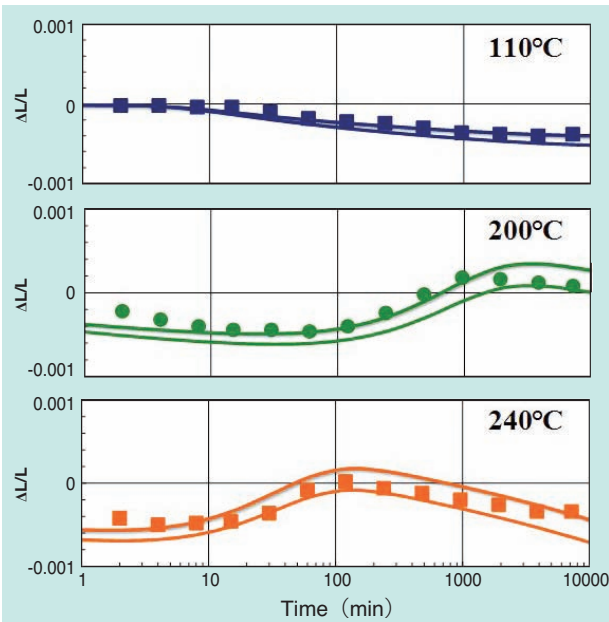


Fig. 5 Experimental (dots) and modeled (curves for Voigt and Reuss estimations) dimensional variations of martensitic H heat treatment at experimental temperatures ^{6,7}

As example of use, the estimation of dimensional variations for equivalent time at 110°C are represented in Fig. 6 for H and HF martensitic heat treatments, with two different initial retained austenite contents ⁷⁻⁸. It is possible to compare the influence of retained austenite content for similar austenitizing temperature and quench.

It is interesting to compare the relative order of magnitude of the different phenomena, displayed in Fig. 6. The contraction of the martensite lattice is large and is the only contraction contribution; it is largely

compensated by the expansion associated to the carbides formation (ϵ and Fe_3C), so that the overall contraction of the evolution of the martensitic phase is not so high. The expansion induced by retained austenite decomposition is of the same order of magnitude to that of Fe_3C precipitation (superimposed curves in Fig 6.b), but is enough to lead in total to a macroscopic expansion.

4. Industrial practice

4.1 Selection of tempering

In industrial practice, hardened bearing steels are never used as quenched, but tempered, in order to reduce the inherent brittleness of quenched high carbon steels.

Tempering after quenching is the beginning of the aging process described in § 2 and § 3 and characterized in § 3, and will be more or less advanced depending on the tempering conditions. Depending on the extent of the tempering i.e. temperature and duration, stage A and possibly stage B described in § 3 occur during tempering.

In service, the material will undergo an additional thermal aging, similar to tempering, during which the phase transformations initiated during tempering continue.

Depending on tempering conditions, the component will present an expansion in service if only stage A occurred during tempering, or a contraction if stages A and B (total decomposition of retained austenite) occurred. It is to be reminded that dimensional evolutions can occur even at low temperatures given that enough time has passed.

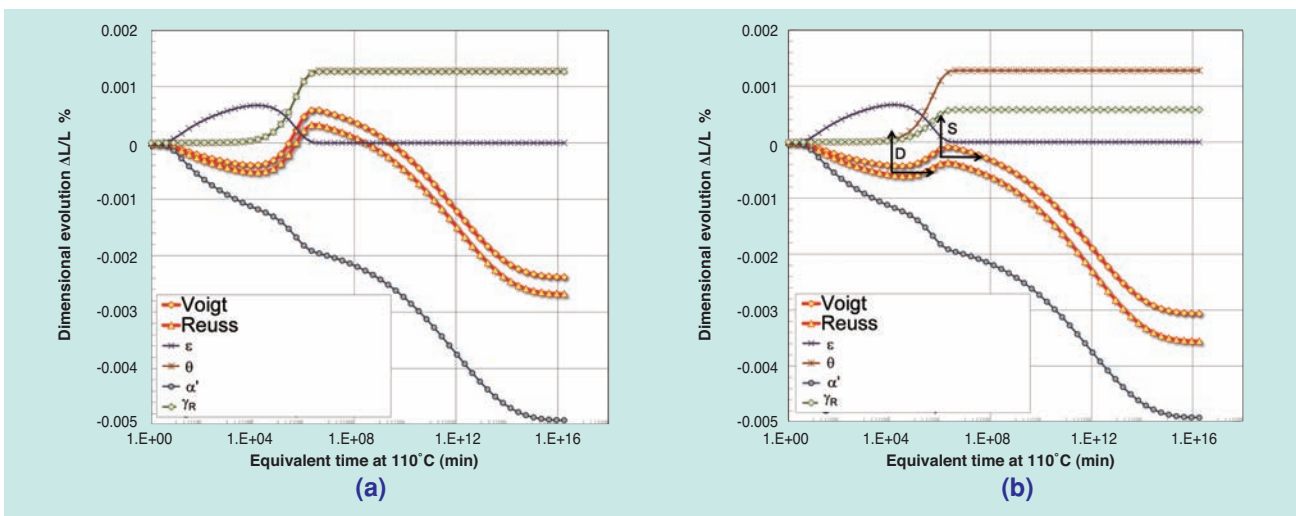


Fig. 6 Estimated macroscopic dimensional variations (Voigt, Reuss) and individual contributions of phases to macroscopic dimensional variations (ϵ , θ , α' , γ_R) for equivalent times at 110°C - (a) H martensitic treatment with 10.7 vol.% retained austenite, (b) HF martensitic heat treatment with 4.7 vol.% retained austenite ⁷⁻⁸ - ϵ stands for ϵ -carbides, θ for cementite, γ_R for retained austenite, R for Recovery

Finally, in the case of SUJ2, depending on the application, different temperings are used, resulting in different properties and advantages/shortcomings:

- ‘Low temperature’ or standard tempering (only stage A occurs during tempering, 1 to 2h at 170-180°C): the hardness obtained is high for good RCF performance and no dimensional stability is guaranteed.
- ‘Higher temperature’ tempering or stabilizing temperings (stages A and B occur during tempering, for example 2h at 230°C): the hardness obtained is lower than that of standard temperings, but a higher dimensional stability is obtained, as no expansion due to retained austenite decomposition will occur, but contraction at long operating times, or high temperatures, or combinations thereof. These temperings are used for bearings subjected to higher temperatures.

The actual temperature/times of NTN-SNR existing standard tempering (D treatment), and stabilizing tempering (S) were used to calculate the equivalent times of aging at 110°C for a SUJ2 steel, so that the time corresponding to the beginning of service for D and S temperings are reported in [Fig. 6](#).

4. 2 Influence of heat treatment conditions on retained austenite

In the previous paragraph, it is shown that it is possible to obtain different hardness/dimensional stability compromises depending on heat treatment parameters.

It is also important to add that heat treatment solutions are in practice also selected for other considerations, for example to minimize distortions, to avoid quench cracking or depending on furnace technology available, and that many criteria are accounted for to design the heat treatment.

Many studies have been carried out on the influence of heat treatment conditions of classical bearing steel on the amount of retained austenite⁹⁻¹²), and its thermal stability, through its practical consequences on dimensional stability.

Pearson⁹⁾ has illustrated for a variability of industrial heat treatment conditions and facilities, the dispersion of size change that can be found for standard treated SUJ2: for an aging of 3000h at 150°C, the size expansion can vary from 7×10^{-4} to 11×10^{-4} , illustrating the influence of the different heat treatment conditions used depending on the bearing manufacturer and facilities.

Franklin¹²⁾ performed an extensive study in the 1970s on the effect of all these parameters on retained austenite content (without measuring its resultant dimensional size change). His main

conclusions and the ones also obtained by other authors are summarized in the following:

- An increase of austenitizing temperature and time increases the amount of retained austenite after quench;
- A quicker cooling rate produces lower retained austenite contents;
- Interrupted quenching (martempering or marquenching), commonly used for SUJ2 to reduce heat treatment distortions and quench cracking likelihood, increases the amount of retained austenite;
- Higher tempering temperature and times will lead to lower retained austenite contents, even if temperatures lower than 200°C will not lead to significant lowering of retained austenite content in SUJ2.

4. 3 Reducing retained austenite content by heat treatment

Different methods can be used to reduce retained austenite content:

- **Subzero treatment** consists in an additional subzero quenching after the standard quenching to room temperature, but small amounts of retained austenite are always retained. It generally consists in an isothermal holding between -100 and -70°C.
- **Water rinsing** consists in submitting the components to a soaking in a water tank at 15-20°C, after oil quench usually realized between 40 and 60°C. It has been shown that this step can reduce a portion of the retained austenite, and resultant dimensional variations.
- **Tempering** (stabilizing heat treatment) is to date the most effective way to suppress retained austenite. For SUJ2 and other low alloyed steels, tempering must be performed at temperatures higher than 200°C for a significant reduction of retained austenite content, and at least 230°C for efficient removal of retained austenite⁹⁾.

5. Conclusions

The issue of dimensional stability cannot be simplified to the content of retained austenite present in the bearing ring, and complex microstructural evolution mechanisms modelled in this paper are responsible for the observed macroscopic dimensional variations.

The model presented here takes into account one initial heat treatment. Other NTN-SNR studies on the evolution of this model enable the evaluation of dimensional variations for other heat treatment conditions.

Nevertheless, the only efficient way to improve dimensional stability in service when needed (if service time and temperatures are high enough to create dimensional changes modifying the internal clearance or loss of fit with mating components) is to select the tempering with an appropriate temperature that will bring the microstructure closer to equilibrium and remove the remaining retained austenite.

References

- 1) Speich, G.R., Taylor, K.A. "Tempering of Ferrous Martensites. Martensite : a Tribute to Morris Cohen", Edited by Olson G.B. and Owen W.S. United States of America, ASM International, 1992. pp. 243-275.
- 2) Porter, D.A., Easterling, K.E. "Phase Transformations in Metals and Alloys", London : Chapman and Hall, 1992, 514p.
- 3) Roberts, C.S., Averbach, B.L., Cohen M. Trans. ASM, 1953, Vol. 45, pp. 576.
- 4) Bhadeshia, H.K.D.H. "Steels for Bearings", Progress in Materials Science, 2012, Vol. 57, pp. 268–435.
- 5) Cheng, L., Brakman, C.M., Korevaar, B.M., Mittemeijer, E. "The tempering of iron-carbon martensite; dilatometric and calorimetric analysis", Metall. Trans. A, 1988, Vol. 19A, pp. 2415-2426.
- 6) Sidoroff, C. "Analyse Microstructurale et Modélisation des Evolutions Dimensionnelles de l'Acier 100Cr6 : Structures Martensitique et Bainitique". PhD Thesis INSA Lyon, 2002.
- 7) Perez, M., Sidoroff, C., Vincent A., Esnouf C. "Microstructural Evolution of Martensitic 100Cr6 Bearing Steel During Tempering: From Thermoelectric Power Measurements to the Prediction of Dimensional Changes", Acta Materialia, 2009, Vol. 57, pp. 3170–3181.
- 8) Sidoroff, C., Perez, M., Dierickx, P., Girodin, D. "Advantages and Shortcomings of Retained Austenite in Bearing Steels : a Review", Bearing Steel Technology, ASTM STP 1580, J. M. Beswick, Ed. American Society for Testing and Materials International, West Conshohocken, PA, 2015, pp. 312-348.
- 9) Pearson, P.K. "Size Change of Through Hardened Bearing Steels at Application Temperatures", SAE Transactions A, 1997, Vol.106, N°.2, pp. 170-175
- 10) Duval, P., Murry, G., Constant, A. "Stabilité Dimensionnelle dans le Temps. Contribution à l'Etude des Facteurs Métallurgiques Affectant la Stabilité Dimensionnelle des Aciers", Mécanique-Electricité, 1968, Novembre, pp. 28-37.
- 11) Hengerer, F., Nierlich, W., Volkmuth, J., Nutz, H. "Dimensional Stability of High Carbon Bearing Steels", Ball Bearing Journal, 1988, Vol. 231, pp. 26–31.
- 12) Franklin, J., Hill, P., Allen, C. "The Effect of Heat Treatment on Retained Austenite in a 1% Carbon / Chromium Steel", Heat Treatment of Metals, 1979, Vol. 6, pp. 46-50.

Photo of authors



Christine SIDOROFF
NTN-SNR Roulements
Technology and Innovation
Department



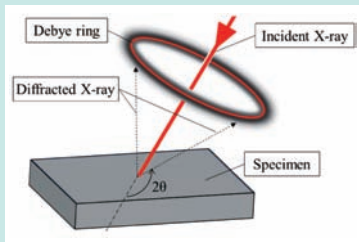
Pierre DIERICKX
NTN-SNR Roulements
Technology and Innovation
Department



Pr. Michel PEREZ
Institut National des Sciences
Appliquées de Lyon
MATEIS Laboratory

Evaluation of Rolling Contact Fatigue by X-ray Diffraction Ring

Naoya KAMURA*
 Takumi FUJITA*
 Toshihiko SASAKI**



In this report, a novel approach for evaluating the progression of rolling contact fatigue (RCF) is introduced. The progression of RCF is evaluated based on tri-axial stress state and the degree of martensite grain orientation which are characterized by two parameters: σ_{eq} and S/S_0 , respectively.

From the behavior of the σ_{eq} and S/S_0 during RCF, it is found that the progression of RCF can be divided into three stages as follows. First, σ_{eq} approaches the yield stress of SUJ2 in the early loading stage; about 10^3 cycles. The S/S_0 does not change in this stage. After drastically increasing the σ_{eq} up to 10^3 cycles, the S/S_0 increases. This shows that the martensite grain orientation on the RCF surface begins to be formed after the 10^3 cycles. Finally, σ_{eq} gradually decreased while developing peeling on the raceway although the orientation of texture continues to progress.

This is a new finding obtained by applying the Debye ring analyzer to the evaluation of RCF. The evaluation of RCF by Debye ring is a promising method, not only to investigate mechanism of RCF, but also to allow for quantitative estimation of the progression of RCF.

1. Introduction

It has been well documented (within many reports) that fatigue associated with microstructural changes, hardness changes, and the formation of residual stress can be observed under the raceway of rolling bearings), ^{1), 2)}.

This is an attempt to estimate the residual life of rolling bearings, to determine the risk of damage to rolling bearings. Previously, three parameters (residual stress, half width and retained austenite assuming plane stress condition) obtained by X-ray stress measurement device were used in the research. However, since the fatigue of rolling bearings varies depending on the operation conditions, it is difficult to accurately estimate the remaining life.

Recently, an analytical device (which can detect Debye rings) was developed and is currently being studied for use in material evaluation ³⁾. Specifically, Debye rings can be used for measuring stress with a single incident angle ($\cos \alpha$ method ⁴⁾). With the $\cos \alpha$ method, the stress can be obtained quickly compared with the conventional methods. In addition, if Sasaki-Hirose method ⁵⁾, which is an extension of $\cos \alpha$

method, tri-axial stress measurement is also possible. Furthermore, information on the orientation of crystal grains can be obtained from the intensity distribution of the Debye rings (obtained on the detector). By using this information obtained by unconventional methods, it should be possible to accurately estimate residual life from the complex mechanism of rolling contact fatigue.

In this paper, we will study the relation between the crystal orientation of martensite (obtained from the Debye rings) and tri-axial residual stress (obtained by Sasaki-Hirose method) in the progression of rolling-contact fatigue of two cylindrical specimens.

2. Theory of Tri-Axial Stress Measurement by X-ray

2.1 Stress Measurement Method with Debye rings

When an X-ray is incident to an object of crystalline structure, a diffraction phenomenon occurs within the crystal that satisfies Bragg conditions, as indicated by the following equation (1).

$$2d \cdot \sin \theta = n \lambda \dots\dots\dots (1)$$

*Advanced Technology R&D Center
 **Faculty of Human Sciences, Kanazawa University

Where,

- d : Lattice spacing
- θ : Bragg angle
- n : Integer
- λ : Wavelength of X-ray

In general, metallic materials (for industrial use) are often poly-crystalline possessing a random crystalline orientation. When tensile stress is applied to these types of materials, the lattice spacing of the crystal grains vary (as shown in Fig. 1) as well as the diffraction angle of each crystal grain changes. Therefore, X-ray stress measurement is accomplished by calculating stress using the difference between the diffraction angles (due to the orientation of crystals⁶).

If the specimen has a crystal grain suitable for X-ray stress measurement (the diameter of crystal grain is 30 μm or less in the state without orientation or aggregate structure⁷), diffraction X-ray is generated within a conical shape centered around incident X-ray (shown in Fig. 2). The diffraction X-ray is measured by a two-dimensional "Debye Rings" detector (as cross-sections of a cone).

For the X-ray stress measurement theory using whole Debye rings, the $\cos \alpha$ method (proposed by Taira, etc.) and a method using a imaging plate (IP) as a detector (proposed by Yoshioka, etc.⁸), and Sasaki, etc.⁹). The $\cos \alpha$ method is an analysis method that assumes a plane stress condition; the Sasaki-Hirose method is a tri-axial stress measurement method,

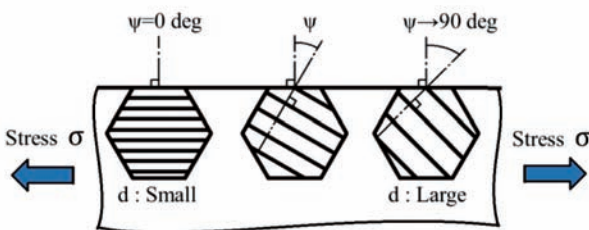


Fig. 1 Changes of lattice spacing by applying tensile stress

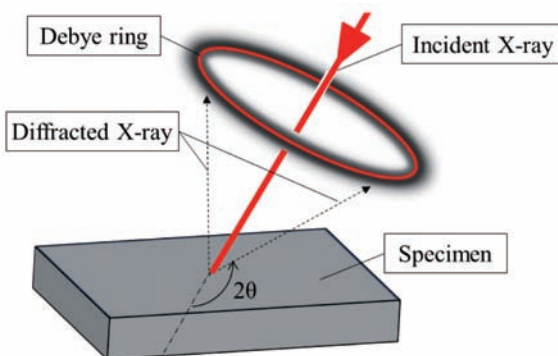


Fig. 2 Schematic drawing of incident X-ray and Debye ring

which is an extension of the $\cos \alpha$ method. The following is a description of the Sasaki-Hirose method.

2.2 Sasaki-Hirose Method

The strain ϵ_α to the central angle α of Debye ring can be expressed as the equation (2) using the radius of Debye ring R_α .

$$\epsilon_\alpha = \frac{1}{2} \left[2\theta_0 - \pi + \tan^{-1} \left(\frac{R_\alpha}{C_L} \right) \right] \cot \theta_0 \dots \dots \dots (2)$$

Where,

- θ_0 : Bragg angle without strain
- R_α : Radius of Debye ring at the position α
- C_L : Distance of X-ray from the radiation point to the detector

The relation between ϵ_α and stress can be expressed by the following equation in the coordinate system in Fig. 3.

$$\begin{aligned} \epsilon_\alpha = & \sigma_x \frac{1}{E} [n_1^2 - \nu (n_2^2 + n_3^2)] \\ & + \sigma_y \frac{1}{E} [n_2^2 - \nu (n_3^2 + n_1^2)] \\ & + \sigma_z \frac{1}{E} [n_3^2 - \nu (n_1^2 + n_2^2)] \\ & + \tau_{xy} \frac{2(1+\nu)}{E} n_1 n_2 + \tau_{yz} \frac{2(1+\nu)}{E} n_2 n_3 \\ & + \tau_{xz} \frac{2(1+\nu)}{E} n_3 n_1 \dots \dots \dots (3) \end{aligned}$$

Where,

- E : Young's modulus of X-ray
- ν : Poisson's ratio

In addition, n_1 to n_3 are direction cosine of ϵ_α and can be expressed by the following equations:

$$\begin{aligned} n_1 = & \cos \eta \sin \psi_0 \cos \phi_0 \\ & - \sin \eta \cos \psi_0 \cos \phi_0 \cos \alpha \dots \dots \dots (4) \end{aligned}$$

$$\begin{aligned} n_2 = & \cos \eta \sin \psi_0 \sin \phi_0 \\ & - \sin \eta \cos \psi_0 \sin \phi_0 \cos \alpha \dots \dots \dots (5) \end{aligned}$$

$$n_3 = \cos \eta \cos \psi_0 + \sin \eta \sin \psi_0 \cos \alpha \dots \dots \dots (6)$$

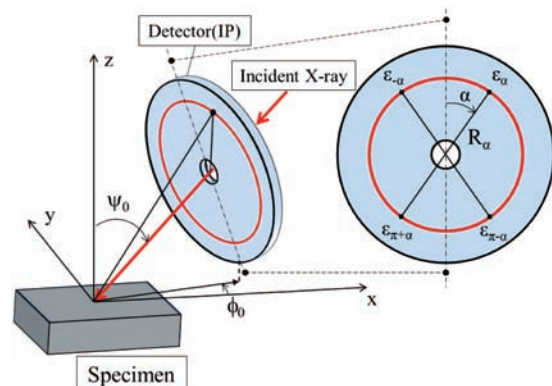


Fig. 3 Relationship between Debye ring on Imaging Plate (IP) and strain ϵ_α

Where,

η : Supplementary angle of Bragg angle
($\eta = \pi/2 - \theta$)

ψ_0 : X-ray incident angle

ϕ_0 : Angle made by incident X-ray and X-axis

Then, to obtain each stress component from the equation (3), strains at the central angles $\pi + \alpha$, $\pi - \alpha$ and $-\alpha$ are expressed as $\varepsilon_{\pi + \alpha}$, $\varepsilon_{\pi - \alpha}$ and $\varepsilon_{-\alpha}$, respectively, with the following parameters newly defined.

$$a_{1(\phi_0)} \equiv \frac{1}{2} [(\varepsilon_{\alpha} - \varepsilon_{\pi + \alpha}) + (\varepsilon_{-\alpha} - \varepsilon_{\pi - \alpha})] \dots\dots(7)$$

$$a_{2(\phi_0)} \equiv \frac{1}{2} [(\varepsilon_{\alpha} - \varepsilon_{\pi + \alpha}) - (\varepsilon_{-\alpha} - \varepsilon_{\pi - \alpha})] \dots\dots(8)$$

From equations (3) to (8), a_1 and a_2 at $\phi_0=0$ are expressed as follows:

$$a_{1(0)} = - \frac{1+\nu}{E} [(\sigma_x - \sigma_z) \sin 2\psi_0 + 2\tau_{xz} \cos 2\psi_0] \times \sin 2\eta \cos \alpha \dots\dots(9)$$

$$a_{2(0)} = \frac{2(1+\nu)}{E} [\tau_{xy} \sin \psi_0 + \tau_{yz} \cos \psi_0] \times \sin 2\eta \sin \alpha \dots\dots(10)$$

When $\psi_0=0$ in equations (9) and (10), namely, when X-ray is incident perpendicularly onto the specimen (perpendicular incident), the following equations can be obtained with the shear stresses τ_{xz} and τ_{yz} :

$$\tau_{xz} = - \frac{E}{2(1+\nu)} \frac{1}{\sin 2\eta} \frac{\partial a_{1(0)}}{\partial \cos \alpha} \dots\dots(11)$$

$$\tau_{yz} = \frac{E}{2(1+\nu)} \frac{1}{\sin 2\eta} \frac{\partial a_{2(0)}}{\partial \sin \alpha} \dots\dots(12)$$

In addition, equations (9) and (10) indicate that a_1 and a_2 are linear to $\cos \alpha$ and $\sin \alpha$, respectively with the slope to be expressed in the following equations:

$$\left(\frac{\partial a_{1(0)}}{\partial \cos \alpha} \right) = - \frac{1+\nu}{E} [(\sigma_x - \sigma_z) \sin 2\psi_0 + 2\tau_{xz} \cos 2\psi_0] \times \sin 2\eta \dots\dots(13)$$

$$\left(\frac{\partial a_{2(0)}}{\partial \sin \alpha} \right) = \frac{2(1+\nu)}{E} [\tau_{xy} \sin \psi_0 + \tau_{yz} \cos \psi_0] \times \sin 2\eta \dots\dots(14)$$

In equations (13) and (14), since τ_{xz} and τ_{yz} are already obtained by equations (11) and (12), when $\psi_0 \neq 0$, $\sigma_x - \sigma_z$ and τ_{xy} can be obtained by the following equations:

$$\sigma_x - \sigma_z = - \frac{E}{1+\nu} \frac{1}{\sin 2\eta} \frac{1}{\sin 2\psi_0} \left(\frac{\partial a_{1(0)}}{\partial \cos \alpha} \right) - 2\tau_{xz} \cot 2\psi_0 \dots\dots(15)$$

$$\tau_{xy} = \frac{E}{2(1+\nu)} \frac{1}{\sin 2\eta} \frac{1}{\cos \psi_0} \left(\frac{\partial a_{2(0)}}{\partial \sin \alpha} \right) - \tau_{yz} \cot \psi_0 \dots\dots(16)$$

$\sigma_y - \sigma_z$ can be calculated when the relation of equation (15) at $\phi_0 = \pi/2$ rad (90°) is used.

σ_z is obtained from the following equation.

$$\sigma_z = \frac{E}{1-2\nu} (\varepsilon_{\alpha} - X) \dots\dots(17)$$

X can be expressed by the following equation.

$$X = \frac{2(1+\nu)}{E} (\tau_{xy} n_1 n_2 + \tau_{yz} n_2 n_3 + \tau_{xz} n_3 n_1) + \frac{1}{E} (\sigma_x - \sigma_z) [n_1^2 - \nu(n_2^2 + n_3^2)] + \frac{1}{E} (\sigma_y - \sigma_z) [n_2^2 - \nu(n_3^2 + n_1^2)] \dots\dots(18)$$

Since each stress component and direction cosine are already known in equation (18), the value of σ_z can be obtained. In addition, equation (17) includes a term of ε_{α} , and since σ_z can be obtained for each central angle of Debye ring, σ_z is determined as their average.

The above is the tri-axial stress analysis method by the Sasaki-Hirose method and 6 stress components can be obtained by three X-ray irradiations indicated by Fig. 5.

3. Experiment Conditions

3.1 Two-Cylinder Test Conditions

Fig. 4 shows the schematic overview of the two-cylinder testing machine and Table 1 shows the test conditions. The test was conducted under the pure rolling conditions. No. 1 to No. 3 are conducted under the conditions of using a specimen of small surface roughness for the driving side (mirror surface drive), No. 4 is conducted under the condition of using a specimen of large surface roughness for the driving side (rough surface drive). In the two-cylinder test, it is known that the damage progression of the cylinder in the mirror side is faster with rough surface drive rather than mirror surface drive^{10), 11)}, and we have investigated its effect on the evaluation of fatigue by X-ray.

The two-cylinder test specimens are made of JIS SUJ2 with standard heat treatment. The shape is cylindrical of $\phi 40 \times 12$ mm and the radii of curvature in the axial direction are indicated in Table 1. No. 1 is a boundary lubricating condition with the maximum contact stress (P_{max}) of 2.77 GPa and the oil film parameter (Λ) of 0.3. No. 2 has mirror surface finish for both specimens (driving/following sides) to comply with the elastohydrodynamic lubrication condition ($\Lambda > 3$). No. 3 uses mirror surface finish for the driving side specimen and ground surface for the following side specimen, similar to No. 1, however, P_{max} is 2.20 GPa, which is a lower surface pressure than No. 1.

Lubrication oil was supplied by contacting a felt pad

Table 1 Two-cylinder type test conditions

No.	Load kN	P_{max} GPa	Curvature in the axial direction		R_q μm		Λ
			Driving	Driven	Driving	Driven	
1	3.92	2.77	∞	60	0.022	0.987	0.3
2	\uparrow	\uparrow			0.025	0.010	10
3	1.96	2.20			0.030	0.945	0.3
4	3.92	2.77	60	∞	0.985	0.029	0.3

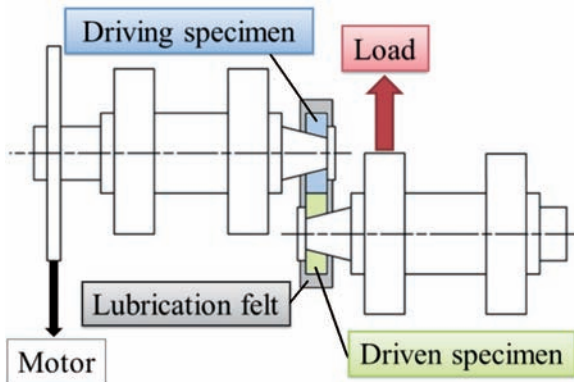


Fig. 4 Schematic drawing of two-cylinder type test

Table 2 X-ray measurement condition

Characteristic X-ray	Cr- K_{α}
Diffraction (hkl)	α -Fe (211)
Tube condition	30kV, 1mA
X-ray irradiated area	$\phi 2$
Incident angle ψ_0 rad (deg)	0, 0.524 (0, 30)
Exposure time s	72

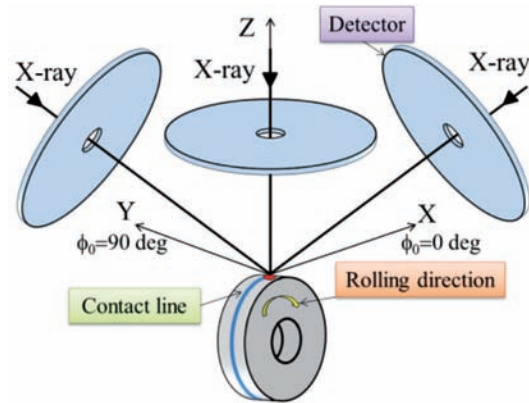


Fig. 5 Relationship between coordinating system in measuring object and location of IP

containing additive-free turbine oil (ISO VG32) to the specimens. The rotational speed of the driving side specimen was set at 500 min⁻¹.

3.2 X-ray Measurement Conditions

We used μ -X360 (made by Pulstec Industrial Co., Ltd.) as the X-ray diffraction ring analyzer. This equipment can analyze the Debye rings (as the diffraction X-ray is detected in two dimensions).

Table 2 shows the X-ray measurement conditions. We used the coordinate system (shown in **Fig. 5**) for the measurement, and the Sasaki-Hirose method described in Chapter 2 for the stress analysis. The irradiation range of the X-ray is $\phi 2$, which is smaller than the major axis of the contact ellipse (2.96 mm) calculated from the test conditions, therefore, only the rolling contact area can be evaluated.

The depth that the X-ray can penetrate in the material (X-ray penetration depth) is given by the following equation ¹²⁾.

$$T_{\alpha} = \frac{1}{\mu} \cdot \frac{\cos 2\eta \cos^2 \psi_0 + \cos \psi_0 \sin 2\eta \sin \psi_0 \cos \alpha}{(1 + \cos 2\eta) \cos \psi_0 + \sin 2\eta \sin \psi_0 \cos \alpha} \quad (19)$$

Where,

T_{α} : Penetration depth of diffraction ray at the position α
 μ : Ray absorption coefficient of iron against Cr- K_{α} ray ¹³⁾
 (889.76 cm⁻¹)

By using equation (19), the relationship between the incident angle ψ_0 and the average penetration depth

is depicted in **Fig. 6**. In this paper, as we set the incident angle of X-ray as 0 rad (0°) and 0.524 rad (30°), the average penetration depths of X-ray are 5.4 μm and 4.6 μm , respectively. Therefore, the X-ray measurement results that we describe later indicate information on the organization and stress variation up to approx. 5 μm from the surface of the specimens.

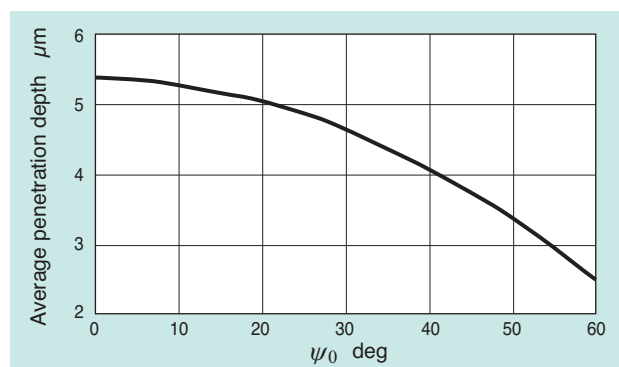
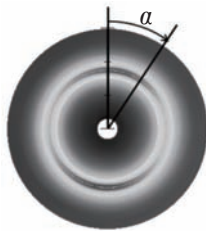


Fig. 6 Relationship between X-ray incident angle and average penetration depth

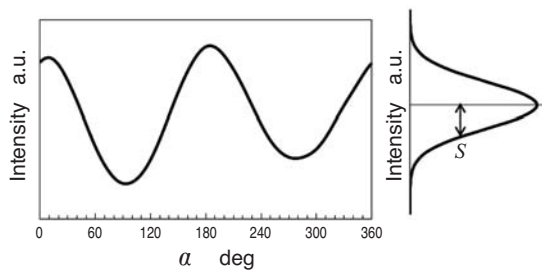
3.3 Evaluation Indices

As the evaluation indices for rolling contact fatigue, parameter S/S_0 , which is defined for the purpose of quantifying change of Debye rings caused by the equivalent stress (Mises stress) σ_{eq} and the crystal orientation, is used. S is the standard deviation of diffraction intensity to the central angle of Debye ring and S_0 is the value of S before the test. With the Debye ring with heterogeneous intensity distribution as shown in Fig. 7 (a), the peak intensity against α is shown in Fig 7 (b) and its standard deviation is indicated by S in the right diagram. On the other hand, σ_{eq} is expressed by equation (20).

$$\sigma_{eq} = \sqrt{\frac{1}{2} \left\{ (\sigma_x - \sigma_y)^2 + (\sigma_y - \sigma_z)^2 + (\sigma_z - \sigma_x)^2 + 6(\tau_{xy}^2 + \tau_{yz}^2 + \tau_{xz}^2) \right\}} \dots (20)$$



(a) Example of Debye ring



(b) Intensities at diffraction peak for central angle and its standard deviation

Fig. 7 Definition of parameter S

4. Results and Observations

4.1 Effect of the Oil Film Parameter

Fig. 8 shows the relation between σ_{eq} and the number of cycles for driving specimens of No. 1 and No. 2. σ_{eq} of No. 2, which is the elastohydrodynamic lubrication condition, exhibits almost no change even when the number of cycles becomes large; however, σ_{eq} of No. 1 exhibits the maximum value at the beginning of the rolling contact, increasing to 1134 MPa, which is close to the yield stress of SUJ2. Then, σ_{eq} gradually decreased along with peeling. Fig. 9 shows the condition of the raceway at the end of the test. This peeling effect was already observed from the early stage (driving cycle: 12×10^4).

Fig. 10 shows the Debye rings obtained from the specimens before and after the test. With No. 1, heterogeneous Debye rings were observed after the test. Fig. 11 shows the relation between the driving cycles and S/S_0 of No. 1 and No. 2. S/S_0 of No. 2 did not change until the end of the test, however, S/S_0 of No. 1 increased as the driving cycle increased. This indicates that the rolling contact fatigue (under the boundary lubrication condition) is a phenomenon with orientation of martensite crystal grains.

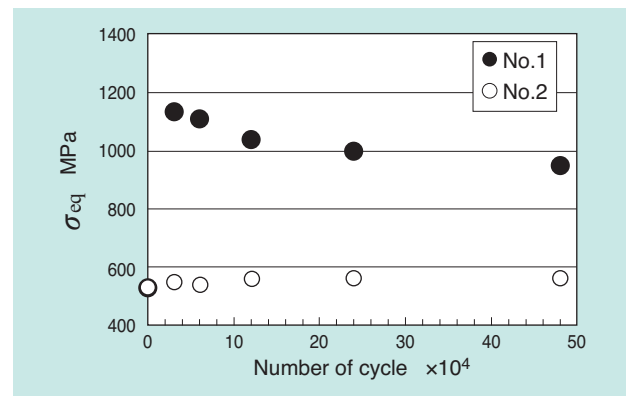


Fig. 8 Relationship between von Mises stress σ_{eq} and number of cycles for driving specimens of No.1 and No.2 tests

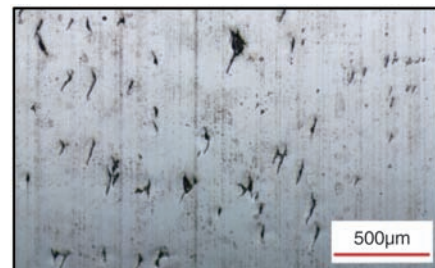


Fig. 9 Peeling for driving specimens of No.1 test after RCF of 48×10^4 cycles

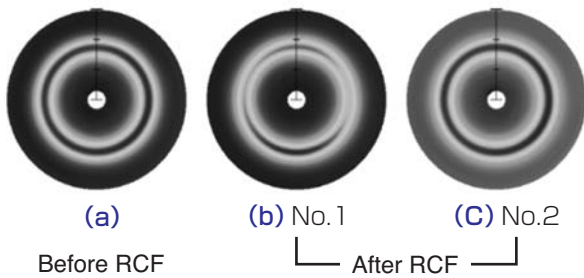


Fig. 10 Debye rings for before and after RCF tests of No.1 and No.2 tests at 48×10^4 cycles

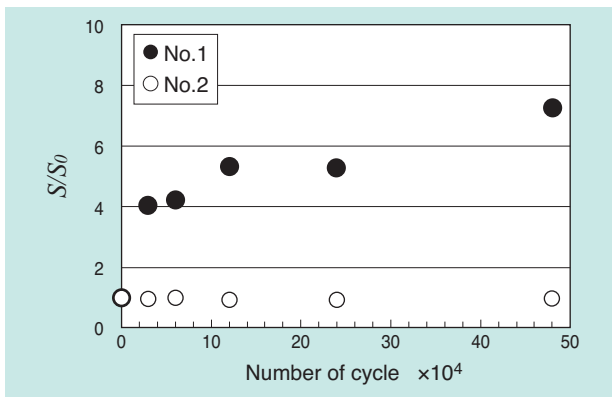


Fig. 11 Relationship between S/S_0 and number of cycles for driving specimens of No.1 and No.2 tests

4.2 Impact of Load

Fig. 12 shows the change of σ_{eq} and S/S_0 against driving cycles of No. 1 and No. 3. The behavior of σ_{eq} and S/S_0 was almost the same between No. 1 and 3, with peeling observed almost at the same time.

The reason why there was no difference in formation of σ_{eq} , behavior of crystal orientation and timing of peeling (even with different loads) is because there was no difference in severity of asperity contact between the two. Rd_q ¹⁴⁾, which indicates severity of asperity contact, exceeds 0.175 rad (10°) before the test for following side cylinder in No. 1 and 3. This value is much higher than Rd_q of the regular bearings ($0.017 \sim 0.070 \text{ rad}$). Contact pressure generated at the asperity contact area of on the surface of large Rd_q is estimated to exceed the limit that the SUJ2 materials can support in any load conditions. Therefore, increase of load does not affect the local contact pressure but only to the increase of real contact area. This is also verified by the X-ray analysis. This is the reason why the load did not affect the formation of σ_{eq} and behavior of crystal orientation.

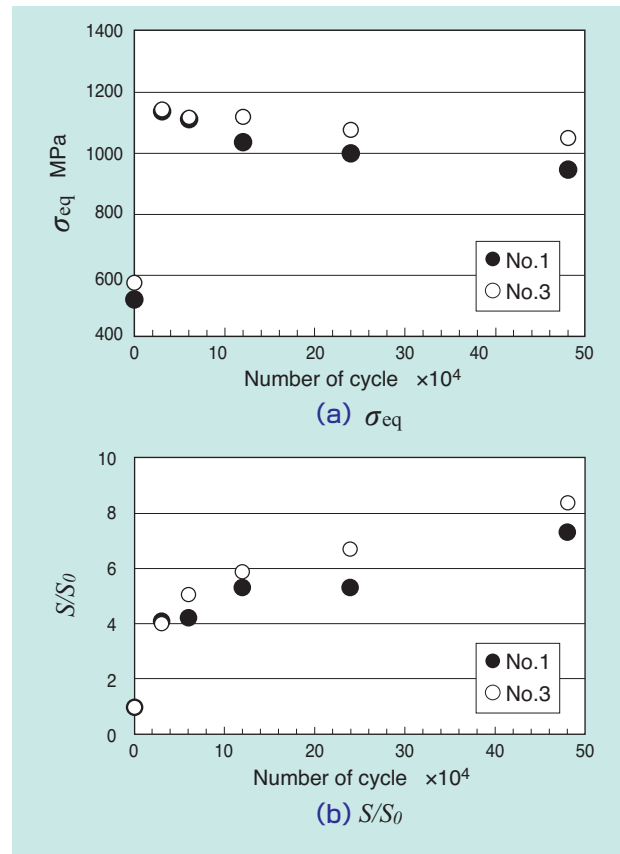


Fig. 12 σ_{eq} and S/S_0 depending on number of cycles for driving specimen of No.1 and No.3 tests

4.3 Change of X-ray Measured Values within the Low-Driving Cycle Range

The fact that σ_{eq} and the shape of the Debye rings in the boundary lubrication condition quickly change in the driving cycle range up to 10^5 has been shown above. In the following, we describe the analysis results of driving cycle range up to 10^5 .

Fig. 13 shows change of σ_{eq} and S/S_0 when rolling contact test was conducted up to 5×10^4 under the same conditions as No. 1. σ_{eq} increased from 533 MPa of before the test to 1084 MPa at 10^3 driving cycles and stayed mostly constant in the range of 1080 to 1200 MPa up to 5×10^4 . On the other hand, S/S_0 showed little change up to 10^3 and then increased after 10^3 revealing the fact that the rolling contact fatigue progresses with generation of residual stress then crystal orientation.

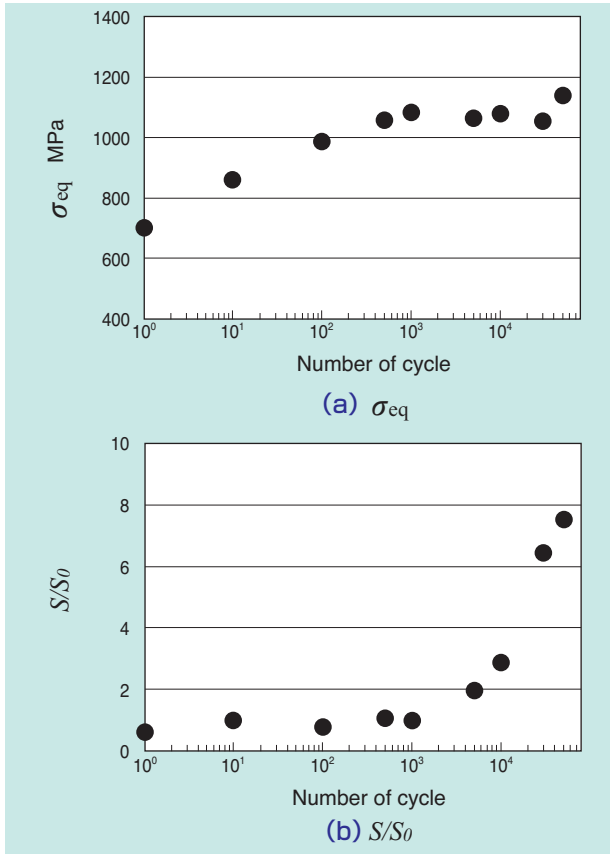


Fig. 13 σ_{eq} and S/S_0 depending on number of cycles up to 5×10^4 for No.1 test

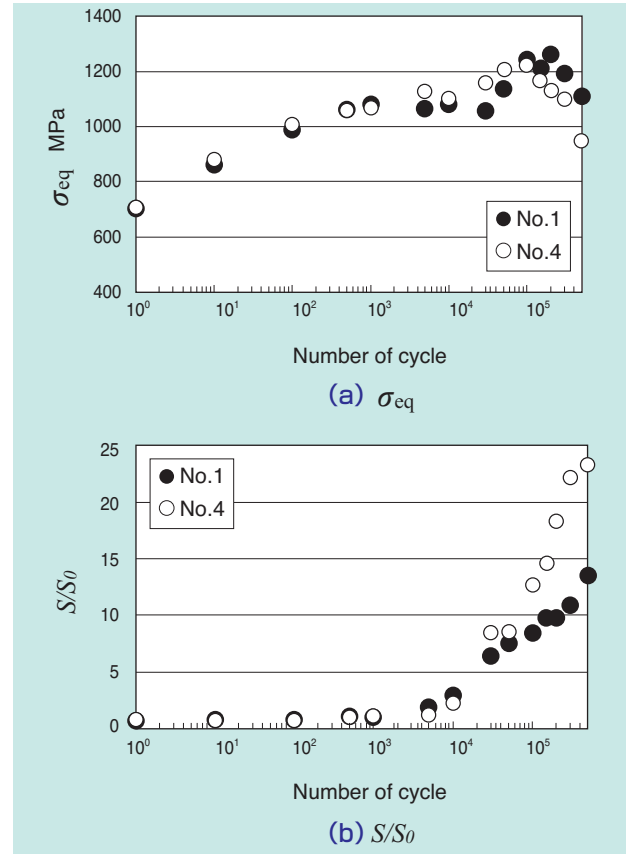


Fig. 14 σ_{eq} and S/S_0 depending on number of cycles for the driving specimen of No.1 and No.4 tests

4.4 Impact of Rough Surface Drive

Fig. 14 shows the change of σ_{eq} and S/S_0 for mirror surface drive cycle of No. 1 and rough surface drive cycle of No. 4. σ_{eq} and S/S_0 exhibited similar behavior in No. 1 and 4 up to the cycles 5×10^4 , then No. 4 showed larger increase of S/S_0 thereafter. In addition, peeling was observed from around 5×10^4 both for No. 1 and 4; however, the progress was faster for No 4 showing significant difference at the cycles of 5×10^5 in the number and magnitude of damages on the raceway as shown in Fig. 15. That is, rough surface drive promotes significant crystal orientation after peeling starts and the progress of peeling was also faster.

These results show that the progressions of rolling contact fatigue for No. 1 and 4 are different after cracking occurs. Kaneta *et al.*¹¹⁾ indicate that the behavior of crack opening can vary between the driving side and following side when cracks and lubricating oil are present on the raceway and this is considered to be the reason why the progressions of peeling in No. 1 and 4 are different. We will study the mechanism of generation and growth of cracks, as well as the mechanism of the formation of crystal orientation, in more detail.

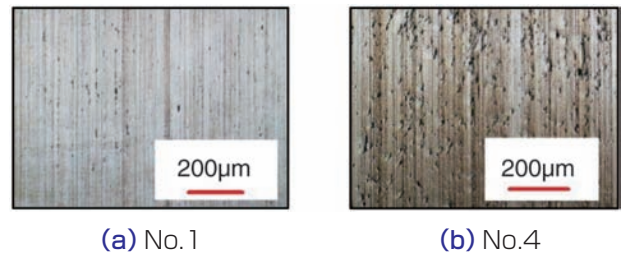


Fig. 15 Peeling on raceway at 5×10^5 cycles

5. Conclusion

We have evaluated the progression of the rolling contact fatigue (under boundary lubrication and fluid lubrication conditions) by the equivalent stress (Mises stress) σ_{eq} obtained by X-ray diffraction ring analyzer and S/S_0 , which indicates the heterogeneity of the Debye rings. The following is the summary of the results:

- 1) σ_{eq} of the rolling contact surface increases closer to the elastic limit of SUJ2 in early stage of around 10^3 .
- 2) After a rapid increase up to the cycles around 10^3 , σ_{eq} remained almost constant until small peeling started.
- 3) In this experiment, the crystal orientation started after the end of the significant increase of σ_{eq} , around the point of 10^3 .
- 4) As the peeling grows, σ_{eq} decreases; however, the crystal orientation continues to progress.
- 5) σ_{eq} and crystal orientation behavior did not change, even if the specimens of driving and following sides are switched up to the point peeling started; however, crystal orientation was more significant with the rough driving after peeling started.

This paper has been edited based on the original manuscripts^{15) and 16)}. We thank Japanese Society of Tribologists and the Society of Materials Science, Japan, who gave us the permission for publishing it.

Reference

- 1) For example, Hiroshi Muro, Noriyuki Tsushima and Masatoshi Tokuda, Changes of Residual Stress due to Rolling Contact, Journal of the Society of Materials Science, Japan, 18, 190, (1969) 615-619.
- 2) Noriyasu Oguma, Prediction of Residual Fatigue Life of Bearings, Part 1: Application of X-ray Diffraction Method, KOYO Engineering Journal, 161, (2002) 26-31.
- 3) For example, Makoto Tominaga, Yoshiaki Akiniwa, Influence of Measurement Area on the X-ray Stress Measurement Using 2D Detector, The Society of Materials Science, Japan, Proceedings of the 47th Symposium on X-ray Studies on Mechanical Behavior of Materials, (2013) 1-6.
- 4) Shuji Taira, Keisuke Tanaka and Toshiharu Yamasaki, A Method of X-Ray Microbeam Measurement of Local Stress and Its Application to Fatigue Crack Growth Problems, Journal of the Society of Materials Science, Japan, 27, 294, (1978) 251-256
- 5) Toshihiko Sasaki, Shunichi Takahashi, Katsunari Sasaki and Yuuichi Kobayashi, A Study on Improvements in Multiaxial Stress Analysis with Area Detector Type Diffraction Method, Transactions of the Japan Society of Mechanical Engineers. A, Vol. 75, No. 750 (2009), 219-227.
- 6) Keisuke Tanaka, Kenji Suzuki and Yoshiaki Akiniwa, Evaluation of residual stress by X-ray diffraction –Foundation and application, 1st edition, Yokendo Ltd. (2002) 99-105.
- 7) X-ray Stress Measurement Standard, The Society of Materials Science, Japan, (1982), 79-84.
- 8) Yasuo Yoshioka, Takeshi Shinkai and Shinichi Ohya, Application of imaging plate to micro-beam X-ray diffraction, Proceedings of the 26th Symposium on X-ray Studies on Mechanical Behavior of Materials, The Society of Materials Science, Japan, (1989) 122-127.
- 9) Toshihiko Sasaki and Yukio Hirose, Stress measurement from one diffraction ring using imaging plate, Proceedings of the 30th Symposium on X-ray Studies on Mechanical Behavior of Materials, The Society of Materials Science, Japan, (1994) 22-27.
- 10) S. Way, Pitting Due to Rolling Contact, Journal of Applied Mechanics, 2, 2, (1935) A49-A58.
- 11) Motohiro Kaneta, Yukitaka Murakami and Hirohiko Yatsuzuka, Fracture mechanics considerations of Way's hypothesis on crack growth in lubricated rolling/sliding contact, Lubrication, 30, 10, (1985) 739-744.
- 12) Toshihiko Sasaki and Yukio Hirose, A method of neutron stress measurement using the $\cos \alpha$ method, Transactions of the Japan Society of Mechanical Engineers. A, Vol. 71, 704, (2005) 670-676.
- 13) Rigaku Corporation, X-ray diffraction handbook, Edition 6, (1998) appendix 4.
- 14) E. Ioannides, G. Bergling & A. Gabelli, An Analytical Formulation for the Life of Rolling Bearings, Acta Polytechnica Scandinavica, Mechanical Engineering Series, 137, (1999).
- 15) Naoya Kamura, Takumi Fujita, Toshihiko Sasaki and Yoichi Maruyama, Tribology Conference Spring 2015, Tokyo (2015) Himeji Proceedings, Evaluation of Rolling Contact Fatigue by X-ray Diffraction Ring, Conference Number F12 (2015).
- 16) Naoya Kamura, Takumi Fujita, Yoichi Maruyama and Toshihiko Sasaki, Evaluation of Rolling Contact Fatigue by X-ray Diffraction Ring, Proceedings of the 49th Symposium on X-ray Studies on Mechanical Behavior of Materials, (2015) 58-61.

Photo of authors



Naoya KAMURA
Advanced Technology
R & D Center



Takumi FUJITA
Advanced Technology
R & D Center



Toshihiko SASAKI
Faculty of Human Sciences
Kanazawa University

Influence of Induction Heating Conditions on Bearing Steel Characteristics

Hiroshi YUKI*
Miyu SATO*



In order to evaluate the characteristics of SUJ2 bearing rings hardened by induction heating (IH) in comparison to those heat treated in a furnace, we researched suitable IH conditions that achieve the same properties as furnace heating. Dimensional change ratio, static load capacity, fracture strength, and shear fatigue strength were evaluated with specimens that were induction hardened with varying temperatures and carbide area ratios. Suitable conditions were determined. Basic rating lives of ball bearings made with the suitable IH conditions were found to be 4 times longer than their calculated fatigue life.

1. Introduction

Changing the heat source of the overall heat hardening of high carbon chromium bearing steel type 2 (hereinafter, SUJ2) from furnace to induction heating (hereinafter, IH) makes it possible to save energy, labor and lowering the environmental load.

On the other hand, IH has disadvantages in productivity compared with the furnace heating and therefore, high temperature heating is often adopted to reduce the processing time per work. When high temperature heating is adopted, hardening starts from the austenite single phase region of the SUJ2 material, which may bring properties different from the products hardened from two-phase regions of austenite phase and cementite phase in furnace heating.

Therefore, in this research, we have explored the optimum induction heating process condition and compared the resulting product with the furnace heated products.

lost and the pinning effect cannot be obtained, which leads to reduced strength due to grain coarsening. Conversely, shortage in solid-solution results in unsatisfactory hardening. Therefore, in this study, we have targeted the carbide area ratios of 4%, 8% and 12%, and the heating temperatures of 900°C, 950°C and 1000°C, which are higher than the furnace heating, in order to investigate the relationship of solid-solution carbon concentration and various properties. For tempering, we have set 3 levels, namely, ordinary tempering condition of atmosphere furnace, 180°C x 2h and 240°C x 43 s targeting 62 HRC, and 310°C x 37s targeting 60 HRC, assuming high-temperature and short-time tempering of IH. As such, we considered 27 levels of 3x3x3 for evaluation. The processing conditions are marked with the heating temperature, carbide area ratio and tempering condition connected by hyphens in this order, such as "900-4-180". **Table 1** indicates the relationship between the heating temperature and heating time for

2. Test method

2.1 IH thermal process conditions

Although knowing solid-solution carbon concentration in the base material is important since it affects various properties, it is difficult to directly measure the concentration.

Therefore, we have controlled the carbide area ratio instead of the solid-solution carbon concentration. When carbon solid-solution is excessive, carbide is

Table 1 IH test conditions

Quenching			
Temperature °C	Target carbide area ratio		
	4%	8%	12%
900	316.0s	57.5s	11.0s
950	65.0s	14.5s	3.0s
1000	10.3s	4.0s	0.7s
Tempering			
Target hardness HRC	Temperature °C		
62	180	2h	
62	240	43.2s	
60	310	36.8s	

*Advanced Technology R&D Center

each carbide area ratio and the relationship between the heating temperature and heating time for each targeted hardness after tempering.

2.2 IH thermal process methods

The test specimens are SUJ2 materials from the same lot.

Table 2 shows the chemical composition of the test specimens.

Table 2 Chemical composition of used SUJ2 (mass %)

C	Si	Mn	P	S	Ni	Cr	Mo	Cu
0.98	0.27	0.42	0.011	0.007	0.06	1.47	0.03	0.08

We have used a high frequency induction heater for heating the test specimens.

With the feedback control using the temperature of the central area of the outer diameter of the test specimens, the temperature of the test specimens were maintained constant. After heating is completed, the test specimens were cooled for quenching in the cold oil of 70°C until the specimens become around 100°C.

2.3 Basic property of each IH thermal processing condition

We have used the ring-shaped test specimens of $\phi 60 \times \phi 54 \times 15$ for investigating the material properties of IH heated-quenched products. Fig. 1 shows the carbide distribution of the IH products. The photos A, B and C in the figure are the IH products processed under the conditions of 950°Cx65.0 s, 1000°C x 4.0 s and 900°C x 11.0 s, respectively. It can be observed that the microstructures are different by the heating conditions. Table 3 indicates hardness, retained austenite after tempering and prior γ grain size.

3. Determination of the optimum condition

3.1 Investigation of dimensional variation ratio

3.1.1 Test method

We have used the ring-shaped test specimens of $\phi 60 \times \phi 54 \times 15$.

Thermally treated rings were maintained at 230°C for 2 hours and the dimensional change ratios before and after heating were determined. The number of tests was set to n=3 for each level. The specimens with the dimensional change ratio of less than 0.050% were regarded as passed.

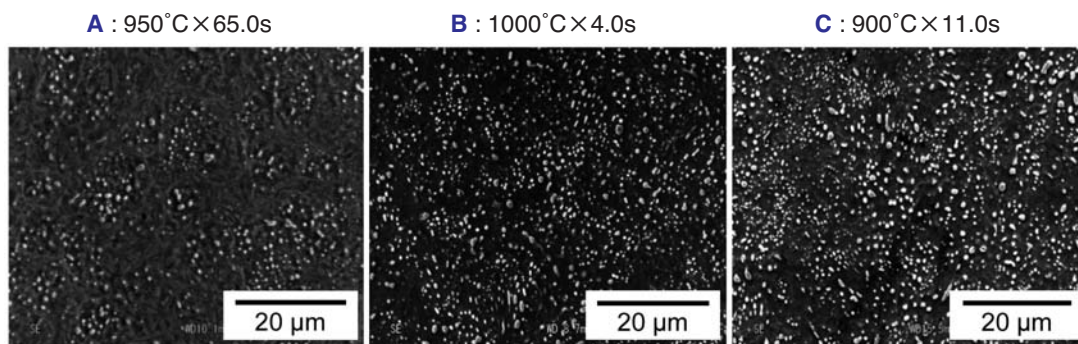


Fig. 1 Cementite distributions

Table 3 Hardness, amount of retained austenite and prior γ grain size after tempering ¹⁾

Heating temperature °C		Tempering temperature °C		Target carbide area ratio								
				4%			8%			12%		
				Hardness HRC	Retained γ amount %	Prior γ crystal grain Grain number	Hardness HRC	Retained γ amount %	Prior γ crystal grain Grain number	Hardness HRC	Retained γ amount %	Prior γ crystal grain Grain number
900	180	62.8	14.6	11.0	62.1	10.5	11.0	61.0	7.9	11.0		
	240	62.5	14.5		62.4	11.2		60.2	8.6			
	310	60.2	7.3		60.9	5.7		57.9	5.4			
950	180	62.5	17.0	9.4	62.3	13.0	10.8	61.3	10.2	11.0		
	240	62.8	17.9		62.3	13.1		61.4	10.7			
	310	60.2	9.8		60.0	7.8		59.1	6.0			
1000	180	62.0	17.2	10.0	62.1	17.3	10.2	62.4	14.6	11.0		
	240	62.3	16.9		62.2	16.5		62.2	14.8			
	310	60.2	11.1		60.1	9.6		60.2	7.8			

3.1.2 Evaluation results

Table 4 shows the dimensional change ratios. The dimensional change ratio tends to become large when the carbide area ratio is 4%. Under the tempering conditions of heating temperature of 1000°C targeting 62 HRC (180°C and 240°C), all the specimens with any carbide area ratio failed. **Fig. 2** shows the relationship between retained austenite amount and dimensional change ratio. There was a strong correlation between the retained austenite amount and dimensional change ratio for the same hardness.

Table 4 Dimensional change ratio ($\times 10^{-5}$)

Heating temperature °C	Tempering temperature °C	Target carbide area ratio		
		4%	8%	12%
900	180	71	36	19
	240	65	38	40
	310	45	25	24
950	180	78	47	35
	240	75	47	39
	310	60	38	26
1000	180	82	77	59
	240	51	62	55
	310	54	48	41

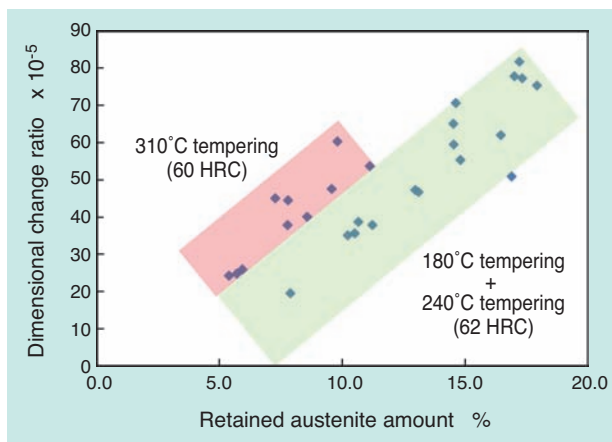


Fig. 2 Relationship between amount of retained γ and dimensional change ratio

3.2 Investigation of static load-carrying capacity

3.2.1 Test method

We have used flat plates of $6 \times 15 \times 3$ which were cut out from the rings of $\phi 60 \times \phi 52 \times 15$ thermally treated under various conditions as the test specimens.

The most broad surface was processed with mirror finish and applied loads of 421.3, 599.9 and 822.9 N which are equivalent to the maximum contact surface pressure $P_{max} = 4.0, 4.5$ and 5.0 GPa with a 3/8 inch bearing made of silicon nitride ceramics on the surface. The load velocity was 3 N/s and the load holding time was 120 s. After removing the load, the

depths of the remaining impressions were measured using a three dimensional surface structure analyzing microscope. The number of tests were set to $n=3$ for each level.

The following is how we organized the test results. It is known that there is a linear relation between logarithm of the maximum contact surface pressure P_{max} and logarithm of δ / D_w , which is depth of impression δ divided by the diameter of the ceramic ball D_w . In addition, the static rated load is known to be the load where the sum of total permanent deformation of the rolling element and that of the raceway becomes 1/10000 of the diameter of rolling element³⁾. The permanent deformation generated by this test is only on the test specimen equivalent to the raceway, however, since the ratio of permanent deformations on the raceway and rolling element is almost the same⁴⁾, we have defined P_{max} when $2 \delta / D_w$ becomes 1/10000 as the static load-carrying capacity. P_{max} , where $2 \delta / D_w = 1/10000$ was calculated from linear approximation, was obtained by the least-squares method from the plotting of $\log(P_{max}) - \log(\delta / D_w)$.

3.2.2 Test results

Fig. 3 shows the static load-carrying capacities. The static load-carrying capacities of the products in the red areas of the figure are lower than those of the furnace heated products with the risk factor of 5%.

That means that the static load-carrying capacities are less when heated with 1000°C.

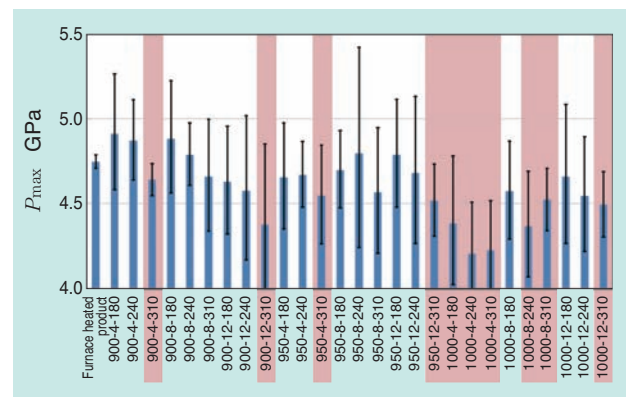


Fig. 3 Static load-carrying capacities

3.3 Investigation of static fracture strength

3.3.1 Test method

We have used the ring-shaped test specimens of $\phi 60 \times \phi 54 \times 15$. We have defined the static fracture strength as the stress converted from the load when the rings were broken by applying load of 1 mm/min using a commercially available tensile/compression testing machine. The number of tests were set to $n=5$ for each level.

3.3.2 Test results

Fig. 4 shows the static fracture strength. The specimens from the heating temperature of 1000°C were excluded from the test as they failed the test for the dimensional change ratio and the static load-carrying capacity was low, as described in 3.1 and 3.2. The static fracture strengths of the products in the red areas of the figure are lower than those of the furnace heated products with the risk factor of 1%. It was determined that the strengths of the products with the carbide area ratio of 4% were lower under the tempering conditions targeting 62 HRC in the heating temperature of 900°C and all the tempering conditions in the heating temperature of 950°C.

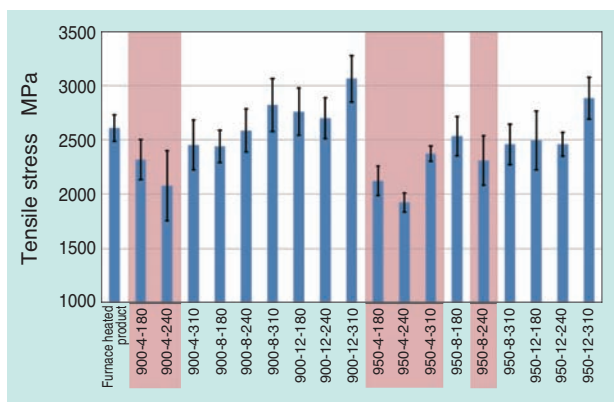


Fig. 4 Static fracture strength

3.4 Evaluation of shear fatigue strength

For rolling bearings, it is known that the shear fatigue is dominant⁵⁾. Therefore, we have evaluated the shear fatigue strength using an ultrasonic torsional fatigue tester⁶⁾.

3.4.1 Test method

Fig. 5 shows the appearance of the test specimen. The area of evaluation was mirror treated to eliminate impact from surface roughness. The intermittent load method was applied alternating loads and pauses with resonance frequency of 20 kHz and stress ratio of R=1 (perfectly reversed loading). When there was no damage up to 10¹⁰ times, the test was terminated.

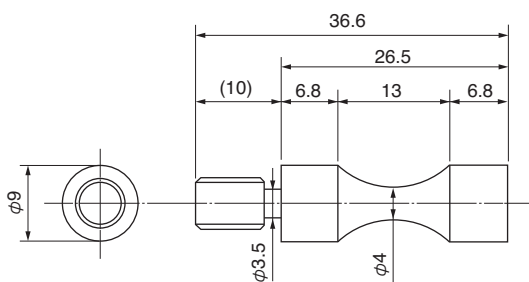


Fig. 5 Schematic drawing of test specimen

3.4.2 Test results

Fig. 6 shows the shear fatigue strength. The specimens from heating temperature of 1000°C were excluded similar to 3.3.

The tempered products with 310°C targeting 60 HRC tend to have lower fatigue strength; however, the other IH heated products had almost the same strength. For detailed comparison, Fig. 7 shows the stress amplitude where the load cycle is 3 × 10⁹. The load cycle of 3 × 10⁹ causes exfoliation in the bearing life test under the maximum contact surface pressure of P_{max} = 2.5GPa. Assuming that the standard deviation of fatigue strength is constant regardless of stress, detection of significant difference with the significance level of 5% revealed that the fatigue strengths after 3 × 10⁹ cycles of all the IH heated products were equivalent or better compared with the furnace heated products.

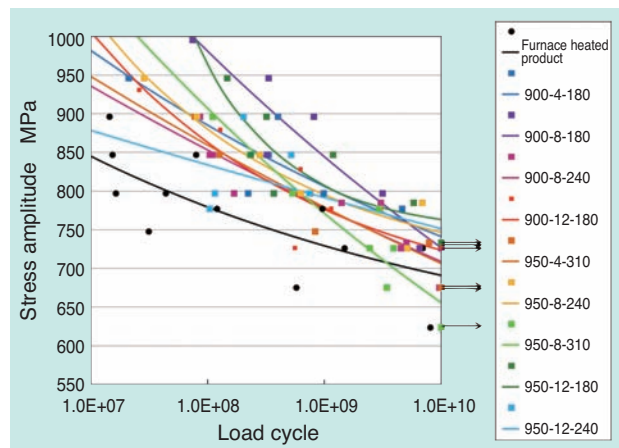


Fig. 6 Shear fatigue properties

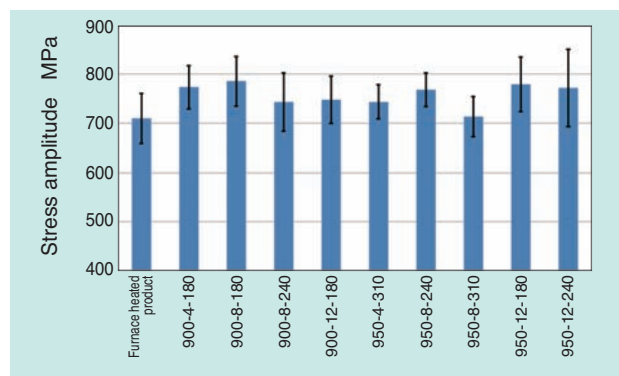


Fig. 7 3 × 10⁹ fatigue strength

3.5 Summary of the test for determining suitable conditions

Table 5 is a list of the dimensional change ratio and results from strength evaluation.

The products with properties equivalent to or better than the furnace heated products are marked with “○” and those with lower strengths are marked with “×”. Those not tested are marked with “—”.

Table 5 Experimental results

Heating temperature °C	Tempering temperature °C	Aging dimensional change ratio			Static load-carrying capacity			Static fracture strength			Shear fatigue strength		
		Target carbide area ratio											
		4%	8%	12%	4%	8%	12%	4%	8%	12%	4%	8%	12%
900	180	×	○	○	○	○	○	○	×	○	○	○	○
	240	×	○	○	○	○	○	○	×	○	○	—	○
	310	○	○	○	×	○	×	○	○	○	—	—	—
950	180	×	○	○	○	○	○	○	×	○	○	—	○
	240	×	○	○	○	○	○	○	×	×	○	—	○
	310	×	○	○	×	○	×	×	○	○	○	○	—
1000	180	×	×	×	×	○	○	—	—	—	—	—	—
	240	×	×	×	×	×	○	—	—	—	—	—	—
	310	×	○	○	×	×	×	—	—	—	—	—	—

3.6 Observation

From the results of this test, we considered the practical range of IH thermal processing conditions that can obtain equivalent performance as the furnace heated products.

First, we take the 310°C tempering. The 310°C tempering is the tempering condition targeting reduced dimensional change ratio by reducing retained austenite volume, with sacrifice of hardness. Because of this, while the dimensional change ratio of 180°C tempering and 240°C tempering resulted in “×” for 1000°C -8% and 1000°C -12%, that of 310°C tempering resulted in “○”. However, because of lower hardness, while the static load-carrying capacity for the 180°C tempering and 240°C tempering resulted in “○”, that of 310°C tempering resulted in “×”, and the overall evaluation also resulted in “×”.

Although the static load-carrying capacities of 900°C-8% and 950°C-8% are “○” even with the 310°C tempering, since the 180°C tempering and 240°C tempering conditions also resulted in “○”, it is not necessary to select 310°C tempering with lower hardness. From the above, we have determined that the 310°C tempering condition is practically unnecessary.

Next, we take the shear fatigue strength of “950-8-180”, which test was not conducted. The results from 900°C-8% and 950°C-12% show that the strength of 180°C tempered products are equivalent to or higher than the 240°C tempered products. From this fact, it is possible to predict that 180°C ≥ 240°C, and since “950-8-240” is marked with “○”, “950-8-180” should also be “○”. Therefore, we have determined that the overall evaluation of “950-8-180” is also “○”.

Since the condition of carbide area ratio of 12% has reduced hardening property, there is a concern in insufficient hardness for thick works. **Table 6** shows the thickness of the test rings and the actual measurement of hardness immediately below the

surface after hardening. The data for the carbide area ratio of 8% is also listed for comparison. Under the condition of the carbide area ratio of 8%, 62 HRC was secured regardless of the heating temperature or thickness. On the other hand, under the condition of the carbide area ratio of 12%, the hardness was about 61 HRC and with the heating temperature of 900°C and thickness of 4.0 mm, the hardness was 60 HRC, since the solid-solution carbon content is lower. This should be caused by partially incomplete quenching with slower cooling speed due to thickness. Since the 900°C-12% product has large insoluble carbide content and less amount of elements which improve quenching property such as carbon and chromium in the base material, in addition to unstable austenite due to low heating temperature⁷⁾, hardness is reduced even by slight reduction of cooling speed. Therefore, the 900°C-12% condition is determined to be unpractical.

Accordingly, **Table 7** shows the suitable conditions where all properties are equivalent or better than the furnace heated products.

Table 6 Hardness of each sample thickness

Heating temperature °C	Carbide area ratio °C	Thickness 4.0mm	Thickness 3.4mm
900	12	60.1	61.0
	8	62.1	62.1
950	12	61.2	61.3
	8	62.1	62.3

Table 7 Suitable IH conditions for JIS-SUJ2

Heating temperature °C	Carbide area ratio °C	Tempering conditions
900	8	180°C × 120min or 240°C × 43.2s
950	8	

4. Bearing life test under the suitable IH thermal treating conditions

We have created raceways for deep groove ball bearings under the suitable conditions mentioned in the previous Chapter and conducted bearing life test.

4.1 Test method

The bearing life test was conducted with clean oil lubrication. Fig. 8 shows the overview of the tester and Table 8 shows the test conditions. The test specimens were from furnace heated products and IH thermal processed products under suitable conditions. The bearing model type of 6206 and the steel balls of SUJ2 were used.

Table 8 Test conditions of the ball bearing RCF life test

Bearing	6206C3
Radial load	6.86kN
Contact stress P_{max}	Inner ring/steel ball = 3.11GPa Outer ring/steel ball = 3.21GPa
Rotational speed of inner ring	3000min ⁻¹
Lubrication	Turbine oil VG56 circulating oil supply
Basic rated life	126h
Termination	1000h

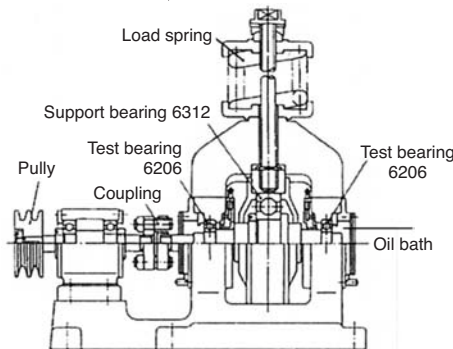


Fig. 8 Schematic drawing of rolling contact fatigue life tester for ball bearings

4.2 Test results

Table 9 shows the test results. The entire eight tested furnace heated products and the entire eight tested “900-8-240” products, as well as the entire seven tested “950-8-240” products exceeded 1000 hours and the test was terminated. The bearing life made from IH thermally treated products can secure product life of more than 4 times of the basic rated life of 126 hours, equivalent to the furnace heated products (930 hours when n is 7)⁸⁾.

Table 9 Life Test Results

Condition	n	Time
Furnace heated product	8	>1015 ~ 1303 h all terminated
「900-8-240」	8	>1207 ~ 1901 h all terminated
「950-8-240」	7	>1075 ~ 1159 h all terminated

Note: Basic rated life: 126 h

5. Conclusion

We have explored IH thermal processing conditions that can obtain the equivalent performance as the furnace heated products for the purpose of changing the heat source of the overall heating of SUJ2 materials for quenching from furnace heating to induction heating and obtained the following insights:

1) The thermal treatment conditions that can secure equivalent performance as the furnace heated products under the test conditions described above are as shown in Table below:

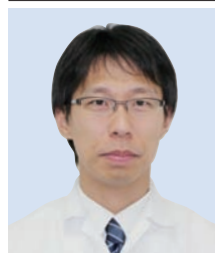
Uniform temperature C	Carbide area ratio %	Tempering condition
900	8	180°C × 120min
950	12	or
	8	240°C × 43.2s

- 2) We have conducted the bearing life test using the raceways made under the above suitable conditions. The result showed that the life of the created bearings was more than 4 times the basic rated life.
- 3) When the heating temperature is raised up to 1000°C under the conditions described in this paper, the dimensional change ratio is degraded. If tempered in high temperature to improve the dimensional change ratio, hardness is reduced and static load-carrying capacity is lowered.

Reference

- 1) JIS Handbook 2007 Ferrous Materials and Metallurgy 1G0551 p. 665 Appendix C Table 1.
- 2) Eschmann, Hasbargen, Weigand: Ball and Roller Bearings—Their Theory, Design and Application—, London, (1958).
- 3) JIS B 1519:2009 “Rolling bearings – Static load rating”.
- 4) Tedric A. Harris: Rolling Bearing Analysis Fourth Edition, John Wiley & Sons, Inc., (2001) 824.
- 5) Junzo Okamoto: Dynamic Load Capacity of the Rolling Bearings, Roller Bearings – Lundberg-Palmgren Theoretical Discussion -, Seibunsha, (1990) 1.
- 6) Sakanaka, Matsubara, Shimamura and Ishii: NTN TECHNICAL REVIEW, 79 (2011) 104.
- 7) Zenji Nishiyama: Martensitic transformation, Maruzen, (1971) 219.
- 8) Takumi Fujita: Rolling Contact Fatigue Life Test Design and Result Interpretation Methods Maintaining Compatibility of Efficiency and Reliability, Journal of ASTM International, Vol. 7, No. 6, (2010).

Photo of authors



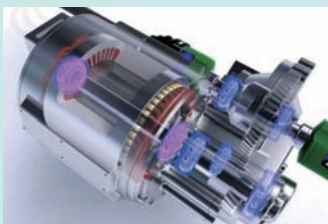
Hiroshi YUKI
Advanced Technology
R&D Center



Miyu SATO
Advanced Technology
R&D Center

Grease Lubricated High-speed Deep Groove Ball Bearing for EV and HEV Motor

Masahiko SATODA*
Goro NAKAO*



EV and HEV are tending to increase the output by increasing the rotational speed to compensate for the output torque reduction by miniaturization of the motor. Therefore, there is an increasing high-speed rotation request also for deep groove ball bearings are used for the motor support.

This paper introduces NTN grease lubricated high-speed deep groove ball bearing for EV and HEV motor, and explains its features and performances.

1. Introduction

The motor drive section of EV/HEV consists of a motor and reducer unit. One of the development trends of EVs and HEVs is smaller drive unit, which requires higher speed of rotation to maintain the output torque.

Bearings that support motor rotation are generally used of grease lubrication, and higher rotation speed increases the temperature of the bearings by centrifugal force of the cage and diffusion of grease. In this paper, we introduce a grease lubricated high-speed deep groove ball bearings for motors of higher speed rotation for EVs and HEVs, which was made possible by reviewing the materials/shapes of cages and blending properties of grease of the conventional bearings.

2. Grease lubricated high-speed deep groove ball bearings for EVs and HEVs

2.1 Challenges for the bearings with higher rotation speed for EVs and HEVs and their measures

In order to achieve higher rotation speed it is necessary to maintain lubricant on the rolling contact surface between the raceway and rolling elements (rolling contact surface) and between the contact surface of the cage and rolling elements (pocket surface). In case of grease lubrication particularly grease diffuses with centrifugal force, which is different from oil lubrication. This causes a shortage of grease on the rolling contact surface and pocket surface resulting in poor lubrication.

Fig. 1 shows the damage process during in life of bearings in high-speed rotation. Poor lubrication on

rolling contact surface ⇒ Rise of temperature and increase of load on the cage ⇒ Seizure and damage on cage.

Fig. 2 shows the resin cage and grease condition immediately before the damage occurred, when the conventional grease lubricating deep groove ball bearings were placed in high speed rotation.

A trace of hard contact of the rolling elements can be observed inside the cage pocket surface of the resin cage. In addition, it is assumed that the cage is deformed by the centrifugal force leaving no space between the cage pocket surface and rolling elements.

Furthermore, degraded grease is attached inside the cage pocket surface indicating that lubrication was poor.

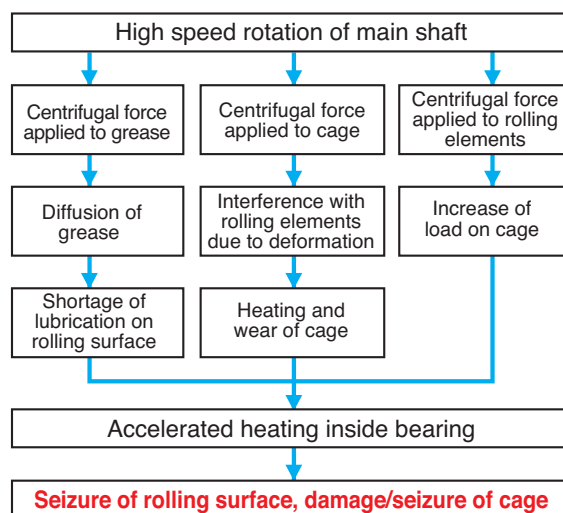


Fig. 1 Bearing damage process in high-speed operation

*Automotive Product Design Dept. Automotive Business HQ

Fig. 3 shows the condition of the grease just before the damage occurred.

Large amount of grease was attached to the side of the seal including grease with no discoloration.

From the above observations, we presumed that the quick damage in high speed rotation was caused by locally insufficient lubrication due to the shortage of necessary lubricant supply. The grease was scraped off from the rolling elements because the pocket space was reduced by the deformation of the cage from the centrifugal force, therefore we developed a cage to cope with.

We also developed grease that is retained in the neighborhood of the rolling element surface so that the base oil is sufficiently supplied in high speed rotation.

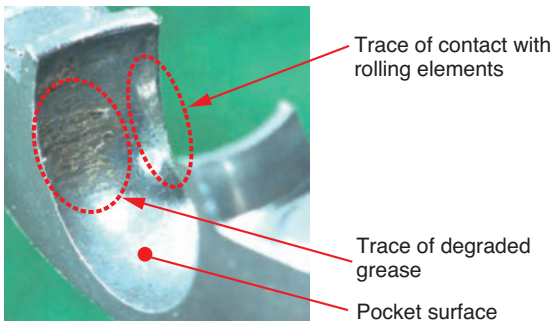


Fig. 2 Cage condition immediately before damage occurred

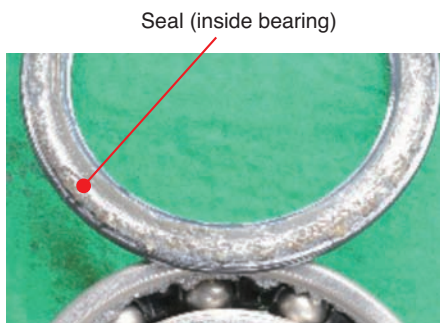


Fig. 3 Grease situation on damage verge

2.2 Structure and features of the developed bearings

By solving the issues described in the previous section, the developed bearings achieved more than twice the high speed performance over the conventional bearings.

● High speed performance

Developed bearings d_{mN} value*1 1.08×10^6
(Conventional bearings d_{mN} value: 0.40×10^6)

*1 Product of the diameter of bearing rolling element pitch circle diameter and rotational speed

In order to achieve the above high speed performance, we focused on the following for development of the new bearings:

- Shape and material of the cage to reduce deformation in high speed
- Strength of the cage against damage
- Improvement of lubricating ability of the grease in high speed rotation

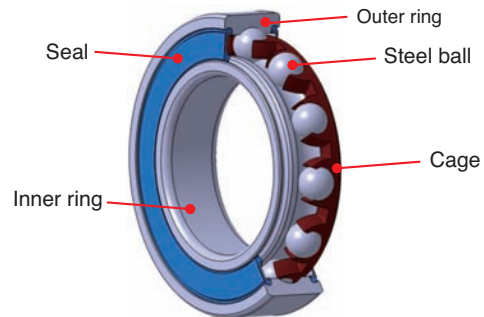


Fig. 4 Grease lubricated high-speed deep groove ball bearing for EV/HEV motor

2.3 Developed cage

(1) Shape and material of cage

We made the following three improvements for reduction of deformation in high speed rotation conditions:

- Adoption of high-strength material
⇒Improvement of rigidity of the cage
- Thicker bottom of pocket to reduce deformation
⇒Improvement of rigidity of the cage
- Reduction of wall thickness between the cage pockets
⇒Reduction of centrifugal force

Fig. 5 shows the difference between the conventional product and developed product. In addition, the difference between the materials of the current product and the developed product is shown in Table 1.

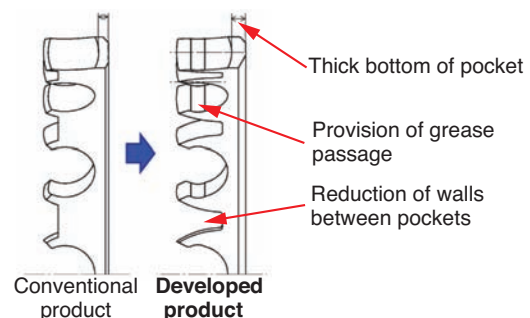


Fig. 5 Shape comparison of current and developed cage

Table 1 Material comparison of current and developed cage

Item	Conventional material	Developed material
Melting point	260°C	>300°C
Specific weight	1.32	1.28
Tensile strength	170MPa	274MPa
Bending strength	260MPa	410MPa
Bending elastic modulus (23°C)	7.6GPa	22.3GPa
Bending elastic modulus (120°C)	3.5GPa	14.1GPa

(2) Strength of cage

We verified static fracture strength of the cage using the strength tester shown in Fig. 6. Fig. 7 shows the comparison of the cage static fracture strength of the conventional product and the developed product. As shown, the cage fracture strength was improved by approximately 1.5 times.

Fig. 8 and 9 indicate the analysis results of the cage deformation and cage stress of the conventional products and developed products at the d_{mn} value of 1.08×10^6 and 120°C . In addition, Fig. 10 and 11 show the relationship of rotation speed and the maximum cage deformation, and the relationship of rotation speed and the maximum cage stress. With the conventional products, the phenomenon as explained in Fig. 2 may occur at the d_{mn} value of around 0.60×10^6 as the cage and the rolling elements interfere. The deformation of the developed products is about 1/10 of the conventional product, leaving enough space between the cage and rolling elements even in the high speed rotation range. In addition, the

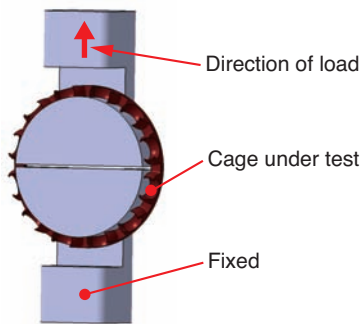


Fig. 6 Cage strength tester

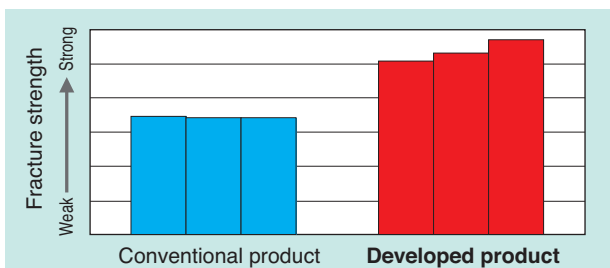


Fig. 7 Static fracture strength of cage

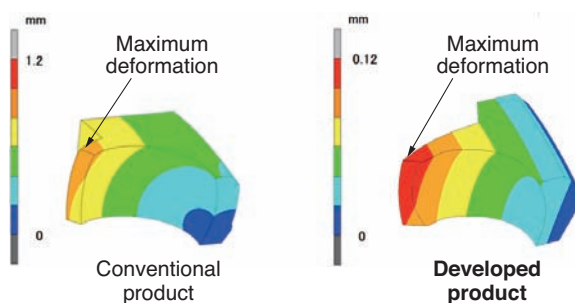


Fig. 8 Analysis result of cage deformation

maximum stress of the developed product is 1/2 or less than the conventional product, resulting in an improvement of endurance as the resin cage.

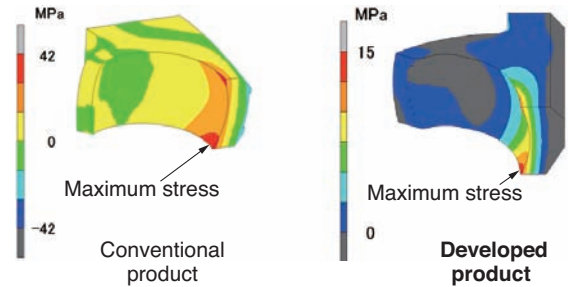


Fig. 9 Analysis result of cage stress

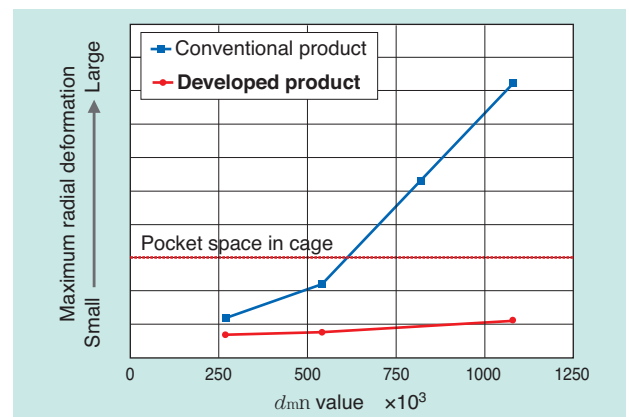


Fig. 10 Relationship between speed and cage deformation

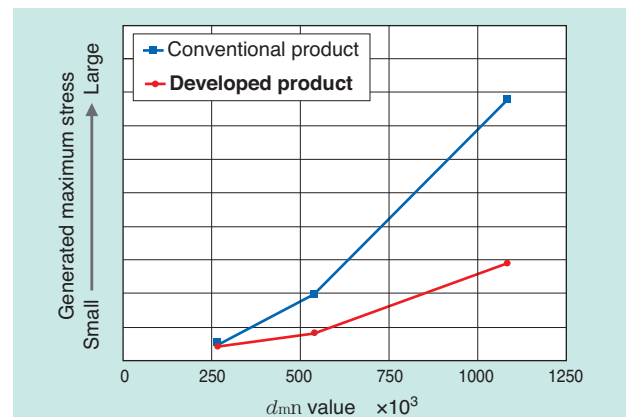


Fig. 11 Relationship between speed and cage stress

(3) Improvement of lubricating property in high speed rotation

The resin cages can reduce heat generation by self lubrication and their wear particles and do not promote oxidative degradation of grease, different from the metallic cages. Furthermore, by providing grooves for oil passage, as shown in Fig. 5, the grease scraping effect is reduced and favorable lubricating property is maintained even in high speed rotation.

2.4 Developed grease

(1) Specification

Table 2 shows the properties of the greases. The developed grease is changed to synthetic oil so that the base oil can better penetrate onto the rolling surface even in high speed rotation of bearings, even with relatively low base oil viscosity.

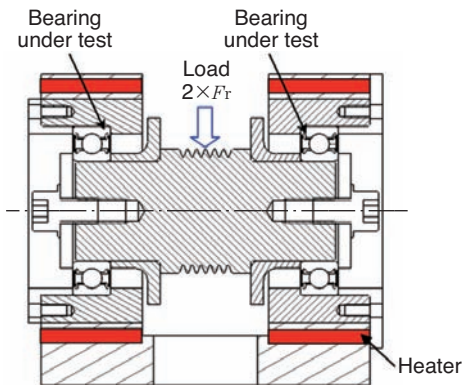
For thickener diurea was adopted and exhibits superior high temperature life. The consistency was set low (hard) to reduce diffusion of grease by centrifugal force to retain the grease close to the rolling element surface.

Table 2 Grease properties

Item	Conventional grease	Developed grease
Base oil	Ester oil	Synthetic hydrocarbon oil
Viscosity of base oil (40°C)	33mm ² /s	48mm ² /s
Thickener	Diurea	Diurea
Consistency	280	220

(2) Performance

Grease life test was conducted with the test machine and test conditions shown in Fig. 12. The evaluation results of high temperature grease life are shown in Fig. 13. The developed grease exhibited around 1.2 times longer life than the conventional grease.



Bearing under evaluation	6204LLB (Steel plate cage)
Rotation speed	10,000min ⁻¹
Load	2,000N
Temperature	150°C

Fig. 12 Grease life evaluation tester / test conditions

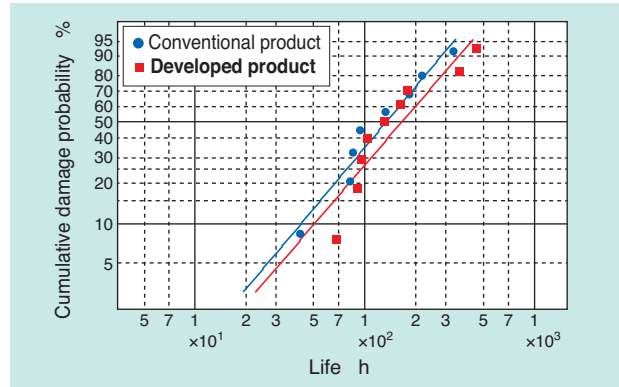


Fig. 13 Grease life evaluation results

2.5 Endurance performance of the developed bearings

(1) High speed endurance test

The endurance test was conducted with three types of samples, labelled A, B and C, including the conventional bearings and developed products. Table 3 shows the test conditions and Fig. 14 shows the high-speed endurance test results. With the conventional bearings (sample A), lubrication on the rolling surface was not sufficient in high speed rotation as most grease was not used causing poor lubrication and seizure/damage (Fig. 3). Sample B, where grooves were provided as oil passage to the sample A, exhibited a longer life with improved oil passage.

Even though the sample B exhibited sufficiently improved life, we adopted new grease with reduced diffusion while retaining supply capability of lubricating oil in high speed rotation to create the developed bearing (sample C). The developed bearing achieved a significant improvement of life, effectively using the grease in bearing.

Table 3 Test conditions and sample specification

Rotational speed	d_{mn} value: 1.08×10^6
Load	0.05C (C : Basic dynamic load rating)
Temperature	120°C
Sample A	Conventional bearing
Sample B	Conventional bearing+developed cage
Sample C	Developed bearing (B+developed grease)

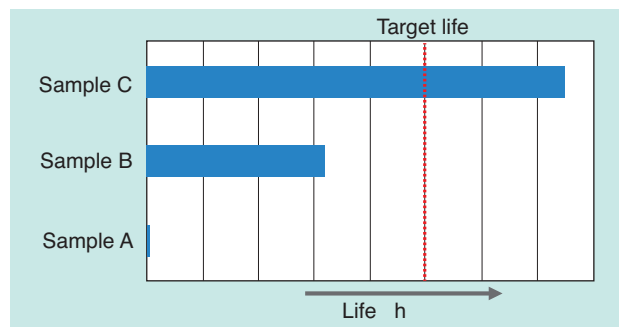


Fig. 14 High-speed endurance test results

(2) Temperature rise test

Fig. 15 shows the results of the temperature rise test under the conditions listed in Table 4. With the conventional bearings, abnormal temperature rise was shown in high speed rotation, and contact of the cage and rolling elements was observed. However, with the newly developed bearings, no abnormal temperature rise was observed, maintaining a favorable condition.

Table 4 Test conditions

Rotational speed	d_{mn} value: $0.135 \sim 1.08 \times 10^6$
Load	$0.05C$ (C : Basic dynamic load rating)
Temperature	Room temperature
Holding time	2 hours for each rotational speed

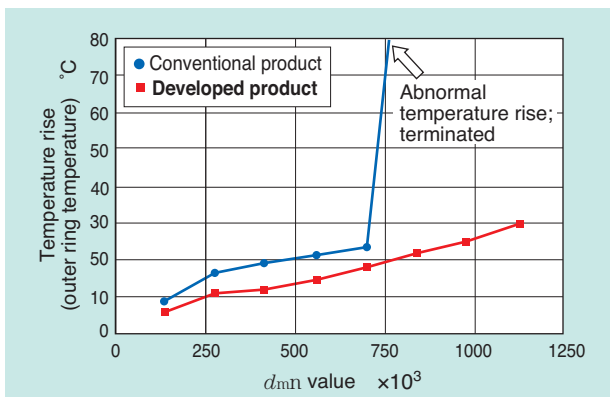


Fig. 15 Temperature rise test results

(3) Rapid acceleration/deceleration test

We conducted rapid acceleration/deceleration test of the developed product under the test conditions listed in Table 5. The conventional bearing failed in less than 100 hours; however, the developed bearing continued to function more than 1000 hours with no issues and no abnormalities.

Table 5 Test conditions

Rotational speed	d_{mn} value $0 \Leftrightarrow 0.70 \times 10^6$ (Rapid acceleration/deceleration test: Fig. 16)
Load	$0.1C$ (C : Basic dynamic load rating)
Temperature	120°C

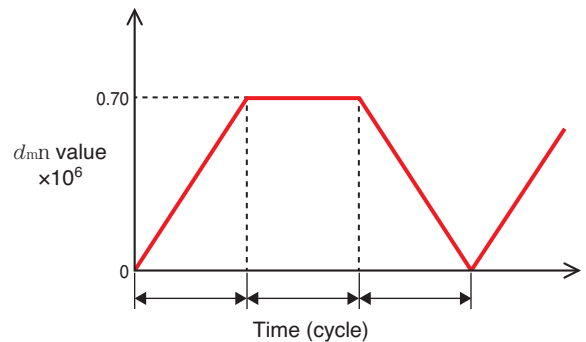


Fig. 16 Rapid acceleration/deceleration test

3. Conclusion

The developed bearing introduced in this article has the following characteristics.

High speed rotation: Can be used under the condition with the d_{mn} value of 1.08×10^6

[Equivalent to the rotation speed of $20,000 \text{ min}^{-1}$,]
 [in case of bearings with inner diameter of 40 mm]

- Limit rotation speed: Twice or more than the conventional bearings

The developed grease lubricating high speed deep groove ball bearings for EVs and HEVs are promising for high speed performance required for EVs and HEVs; therefore, we will actively promote it in the market. In addition, we will continue developing products to help EVs and HEVs evolve further with higher performance.

Photo of authors



Masahiko SATODA
Automotive Product Design Dept.
Automotive Business HQ



Goro NAKAO
Automotive Product Design Dept.
Automotive Business HQ

Deep Groove Ball Bearing for Alternator Corresponding to 200°C

Tomoyoshi IZUTSU*
Goro NAKAO*



According to electrification of automotive auxiliary equipment progresses, electric power consumption of vehicle will increase. As enhanced power generation is required and usage environment tends to become high temperature, alternator bearing is also required to support high temperature.

This article introduces the feature and the performance of the 200°C capable bearing for automotive alternator.

1. Introduction

Requirements on vehicle components are broad including improvement of reliability, lighter weight, compactness and electrification demands. These requirements continue to become more severe.

In addition, today as significant progress has been made in electrification of vehicles for improved comfort, safety and fuel economy, further increases in the generating capability of alternators is required. Among other specifications, the bearings for alternators are required to have high temperature resistance, brittle flaking resistance, anti-corrosive properties, and low temperature properties.

Along with the increase of power generation capability, bearings are also required to have specifications with resistance to high temperature. Therefore, NTN has developed ball bearings for alternators which can be continuously used within temperature envelopes of 180°C¹⁾.

Furthermore, anticipating that the operating temperature of alternators will increase up to 200°C, NTN has developed bearings to support such use. In this paper, "Deep Groove Ball Bearing for Alternator Corresponding to 200°C" is introduced, which is twice more resistant than the conventional products, with improvement of bearing material, cage, seal and grease performance.

2. Bearings for alternators with operating temperature of 200°C

2.1 Features

(1) Support to 200°C

Bearing operating temperature range: -40 to 200°C

(2) Long life

Grease life, brittle flaking life: More than two times compared with the conventional product

(3) High corrosion resistance

Grease anti-corrosive performance: More than two times compared with the conventional products

Metal anti-corrosive performance: More than 5 times compared with the conventional products

2.2 Structure

Fig. 1 shows the structure of the bearing for alternators operating up to 200°C.

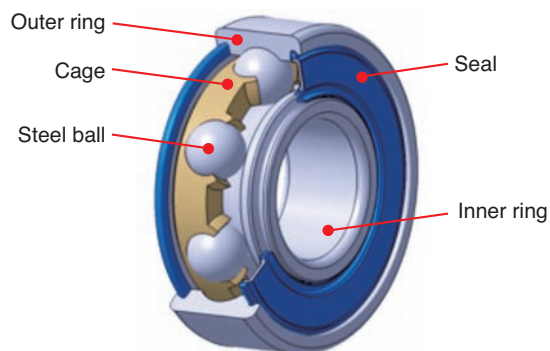


Fig. 1 Deep groove ball bearing for alternator to 200°C

*Automotive Product Design Dept. Automotive Business HQ

2.3 Bearing specifications

(1) Inner ring/outer ring

High carbon chromium bearing steel (SUJ2) is adopted for the inner ring and outer ring that compose the raceways, with improved dimensional stability in high temperature by special heat resistance treatment, as well as improved brittle flaking properties. Fig. 2 shows the comparison results of brittle flaking life.

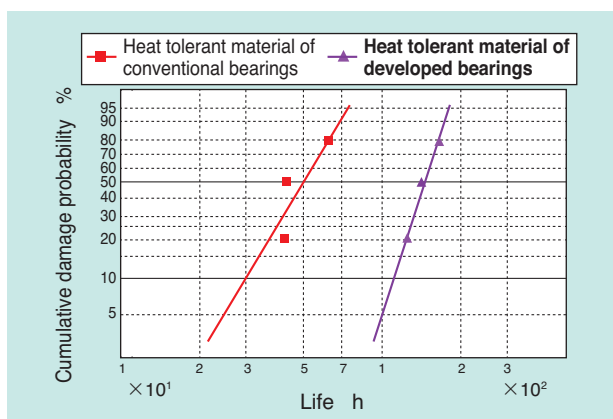


Fig. 2 Brittle flaking life comparison

(2) Cage

Cages of bearings for alternators are required to function in a broad temperature range, in addition to high strength and tolerance to withstand the constant load from the balls caused by rapid acceleration/deceleration and installation error against the shaft. Metallic cages may drive degradation by metallic wear particles or if oil film between balls and cage becomes very low. Therefore, PPS resin was adopted as the cage material, featuring high strength and heat tolerance as longer grease life can be expected.

Fig. 3 shows the analysis results of the stress on the cage, generated when the bearing rotates at 20,000 min⁻¹. Since the maximum stress at the weakest part is 57 MPa and the tensile strength of this material when degradation of 200°C x 1,000 h is assumed is 125.4 MPa, the safety factor is more than two.

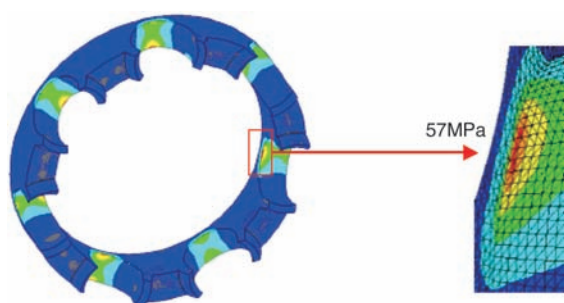


Fig. 3 Results of cage stress analysis

(3) Seal

To prevent leakage of grease and foreign objects from entering, a contact type rubber seal with the uniquely designed seal lip shown in Fig. 4 was adopted. Fluorine-contained rubber, which has good compatibility with the developed grease as described later, was adopted as the rubber material which allowed its use for temperatures up to 200°C.

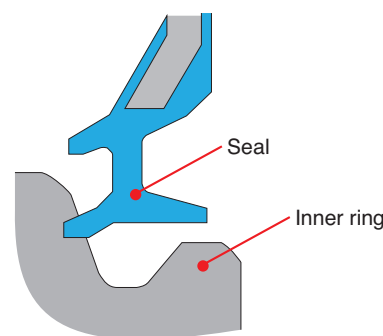


Fig. 4 Seal shape

(4) Grease

NTN has been developing/adopting urea based grease with improved performance in all aspects such as high temperature resistance, brittle flaking resistance, corrosion resistance, low temperature property, etc. These properties are required with bearings for auxiliary equipment²⁾. However, when support for 200°C is considered, fluorine contained grease which has superior high temperature resistance was adopted, since urea based grease has significant precipitation of amine, which attacks rubber seals. However, conventional fluorine contained grease has several issues such as increase of torque during cold starts of alternators, increase of self-heating and metal anti-corrosive properties. Therefore, we developed a new fluorine contained grease improving these issues.

The basic properties of this grease are shown in Table 1.

Table 1 Grease properties

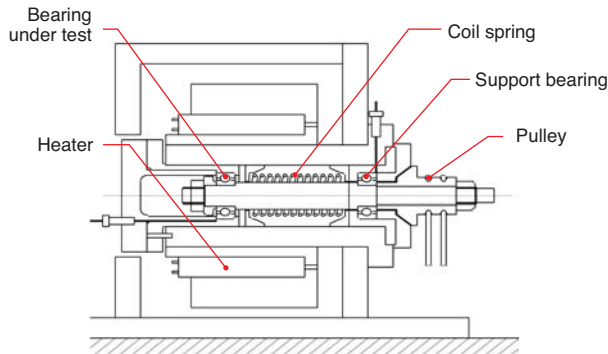
	Developed fluorine contained grease	Conventional fluorine contained grease
Thickener	PTFE	PTFE
Base oil	PFAE	PFAE
Dynamic viscosity of base oil mm ² /s	40°C	130
	100°C	17.5
Worked penetration (60W)	280	265~295
Drop point (°C)	—	232 or more

Test method: JIS K 2283, JIS K 2220

2.4 Performance

(1) High temperature resistance

Fig. 6 shows the result of evaluation for grease life under the temperature of 200°C with the measurement equipment and test conditions listed in Fig. 5. The developed grease has a proprietary additive blended in to prevent metal contact and reduce wear providing more than two times the seizure resistance compared with the conventional grease.



Bearing size	6204 (φ 20 × φ 47 × 14)
Rotational speed	10,000min ⁻¹
Load	$F_r = F_a = 67N$
temperature	200°C

Fig. 5 Grease life tester/test condition

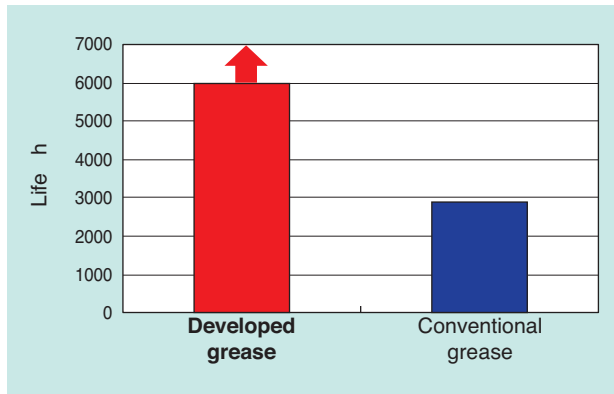


Fig. 6 Grease life test results

(2) Rapid acceleration/deceleration property

The actual operating conditions of alternators include rapid acceleration/deceleration with large loads. Therefore, endurance needs to be evaluated under the actual operating conditions.

Fig. 7 indicates the high temperature and rapid acceleration/deceleration test conditions which match with the actual operating conditions. The results are shown in Fig. 8.

As the results of the rapid acceleration/deceleration test show, the developed grease exhibited longer life than the conventional grease by more than two times, even under the actual operating conditions.

Bearing size	6202 (φ 15 × φ 35 × 11)
Temperature	200°C

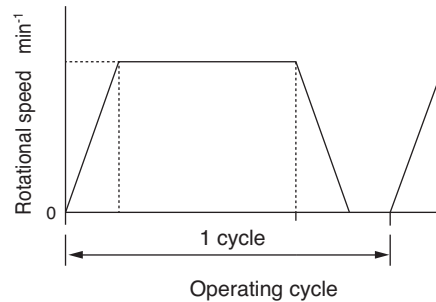


Fig. 7 High temperature rapid acceleration/deceleration test conditions

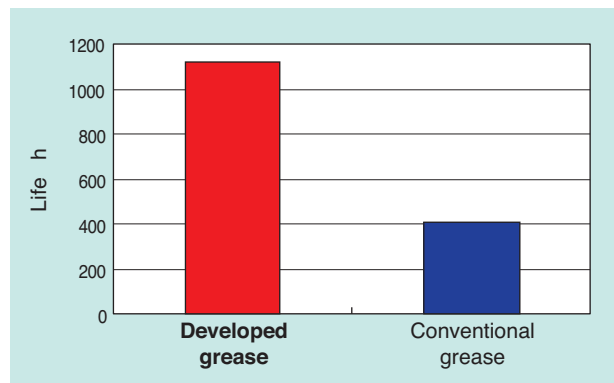


Fig. 8 High temperature rapid acceleration/deceleration test results

(3) Brittle flaking property

Fig. 9 shows the evaluation results of brittle flaking property under the NTN conditions. The developed grease has longer life than the target life by more than twice.

Bearing size	6203 (φ 17 × φ 40 × 14)
Rotational speed	Rapid acceleration/deceleration conditions
Temperature	Room temperature

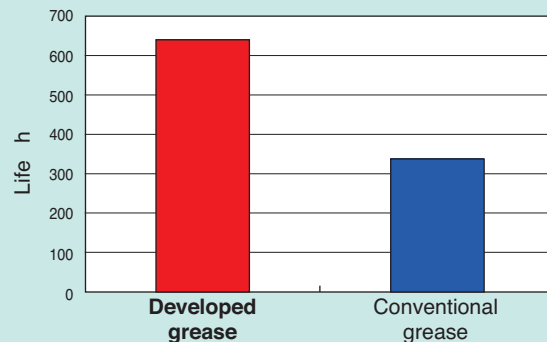


Fig. 9 Brittle flaking life test results

(4) Corrosion resistance

Fig. 10 shows the corrosion resistance test conditions for the developed grease and the results. As the result of the corrosion resistance test, the developed grease exhibited significant improvement on the corrosive resistance.

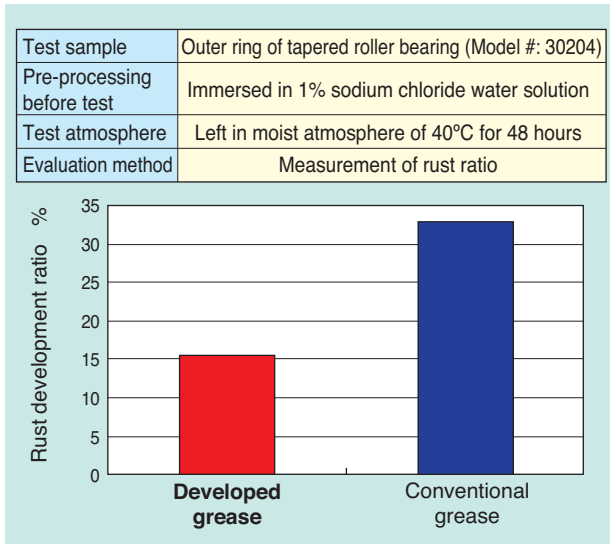


Fig. 10 Rust test results

(5) Low temperature property

The operating environment of alternators can include low temperature operation down to -40°C. Grease inside bearings may be hardened at these temperatures which may prevent the alternator from running smoothly. The low temperature torque test conditions and its results are shown in Fig. 11. The developed grease has improved low temperature torque to 1/6 or less compared with the conventional grease.

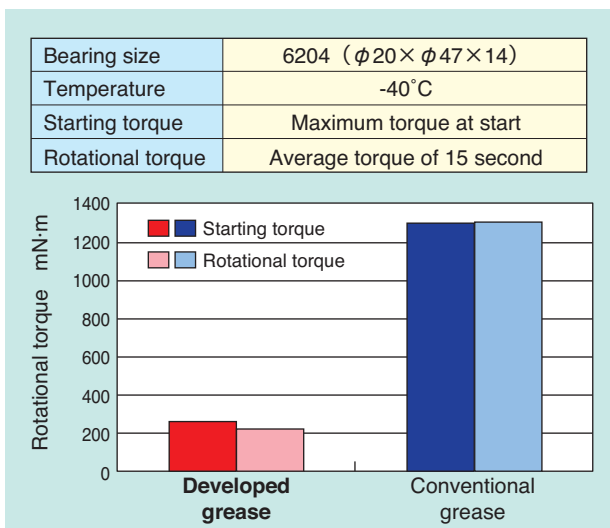


Fig. 11 Rotation torque measurement results

(6) Anti-corrosive property to metal

In general, fluorine bonds with iron (Fe) when it comes in contact with metallic active surface causing corrosion and increasing wear. To address this problem, the developed grease has a unique additive which adheres on the metal surface to reduce reaction of fluorine and iron, then consequently metallic wear.

Fig. 12 shows measurement results of wear amount (iron content) inside bearings under the high temperature resistance evaluation and Fig. 13 shows the appearance of the bearings after the test. With the developed grease, the iron content was 1/5 of the conventional grease, showing the effect of the additive to reduce metallic corrosion from fluorine.

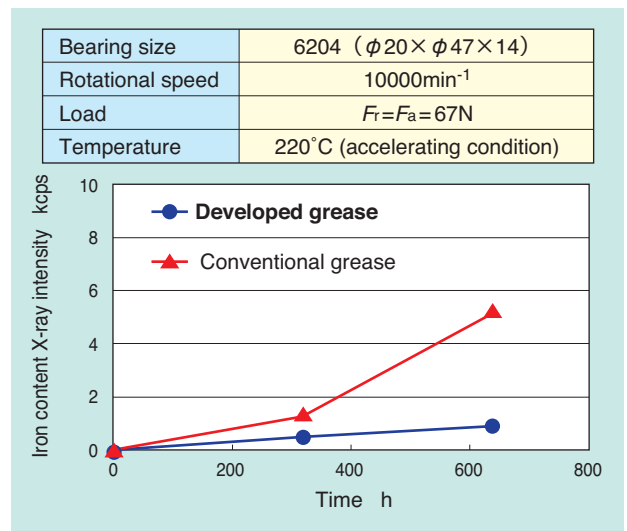


Fig. 12 Iron weight measurement results



Fig. 13 Internal conditions of bearings after test

(7) Temperature rise of self heat generation

Since the alternator rotates at high speed, it is necessary to verify that it does not become unexpectedly hot due to self heat generation inside the bearings. Fig. 14 shows the test equipment and conditions and Fig. 15 shows the measurement results of the temperature rise.

The developed grease has stable result even at 20,000 min⁻¹.

Bearing size	6203 (φ 17×φ 40×12)
Rotational speed	5,000~20,000min ⁻¹
Load	300N
Temperature	Room temperature
Measurement position	Outer ring (when stabilized)

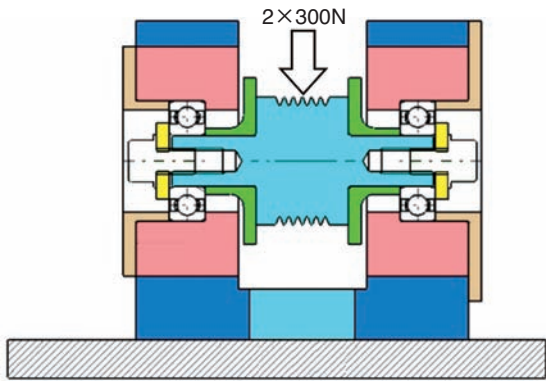


Fig. 14 Grease life tester and test condition

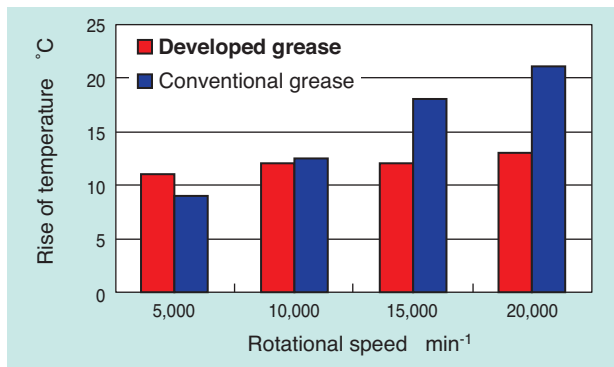


Fig. 15 Measurement results of temperature rise

3. Conclusion

The features of the bearings for alternators operating in 200°C introduced in this paper are as follows:

- By improving the bearing material, cage, seal and grease, the bearing can now be used in a wide temperature range from -40°C to +200°C.

Since this developed product increases the high temperature resistance and prolongs the life by twice, application of these bearings in high temperature environment due to further increase of power generation capability of alternator can be expected. We believe they contribute to further electrification of vehicle components.

Reference

- 1) Ikuo FUJINIWA, Makoto MURAMATSU and Tadahisa TANAKA, Accessory Technology Trends and Product Developments, NTN TECHNICAL REVIEW No. 75 (2007), 110-115
- 2) Takayuki KAWAMURA, Hidenobu MIKAMI, Development of NA103A Long-life Grease for Automotive Components, NTN TECHNICAL REVIEW No. 75 (2007), 116-123

Photo of authors



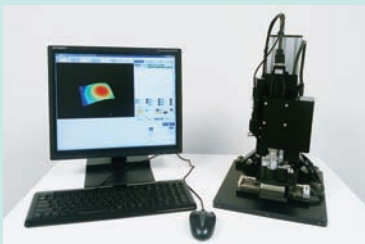
Tomoyoshi IZUTSU
Automotive Product Design Dept.
Automotive Business HQ



Goro NAKAO
Automotive Product Design Dept.
Automotive Business HQ

3D Microgeometry Measuring Machine

Hiroaki OBA*



NTN has developed a 3D microgeometry measuring machine that can measure a height length of 20 micrometer only for 0.6 seconds and is the fastest in class.

By the development of unique image analysis software, in addition to adapting a scanning white light interferometry and a high-speed camera, speeding up has been realized.

The image analysis software has various functions that are 3D viewer, profile viewer, automatic measurement function of height and volume, analysis function of surface roughness, etc.

When this equipment is mounted on NTN desktop fine pasting system, the shape of the ink immediately after pasted can be checked.

1. Introduction

In the microprocessing field, it is important to manage the surface properties and dimensions of finished work after etching, precision machining, application of chemical solution, etc. In order to maintain the required product quality, visual inspection is conducted during processing and after completion of work. Microprocessing has been applied particularly within the electronic component field where advancement in micro wiring patterns is significant and the medical device field where superior reliability is required. Consequently, improvement of productivity (by reducing inspection time) and even higher quality are now required, however most commercially available 3D measurement systems require more than several seconds for measurement, which is not practical for verification along the production line.

NTN has developed the fastest 3D microgeometry measuring machine (hereinafter, "this measurement system") in its class by adopting a white light interferometer and high-speed camera and developing unique image analysis software, allowing a minimum measurement time of 0.6 seconds for a measurement range of 20 μ m. This paper introduces the features of this system.

2. Overview of 3D Microgeometry Measuring Machine

2.1 Principle of Measuring Height

1) Configuration of White Light Interferometer

Fig. 1 shows the white light interferometer adopted in this system for detecting focusing position. The white light interferometer is configured by combining a two-beam interference objective lens with the microscope lens barrel.

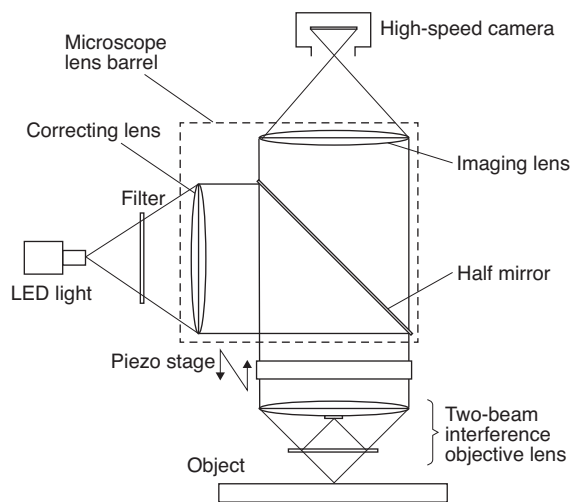


Fig. 1 White light interferometer

*New Product Development R&D Center

In general, the Michelson type two-beam interference objective lens is used for low magnification and the Mirau type is used for high magnification. In this system, the Michelson type is used for x2.5 and x5 and the Mirau type is used for x10, x20 and x50 magnifications.

Fig. 1 shows an example of configuration of the Mirau type two-beam interference objective lens.

2) Measuring Principle

- Generating Principle of Interference Fringes

Fig. 2 shows a diagram of the Mirau type two-beam interference objective lens. This objective lens has a reflective mirror on the central part of the objective lens surface and a semi-transparent mirror in the middle of focal plane of the objective lens. The semi-transparent mirror induces interference between the reflected lights from the surface of the object and from the reflective mirror. The intensity of the interfered light is maximized when the focus on the objective surface is obtained as indicated by the red lines in Fig. 3.

Images are captured by moving the two-beam interference objective lens in the direction of the optical axis in order to obtain the coordinates where the interference light maximizes its intensity for each pixel, from which the focusing position, namely, the height information of the object surface, is calculated.

In order to obtain the coordinates on the optical axis from the intensity of interference light, it is necessary to capture images by moving the lens at a constant interval in the direction of the optical axis. Since the accuracy of this interval affects the measurement accuracy, a piezo stage was implemented for moving the two-beam interference objective lens.

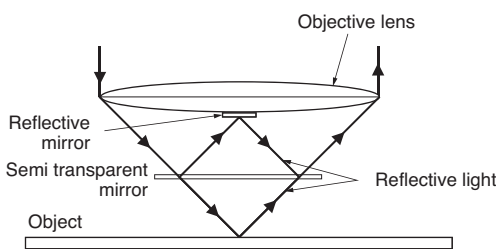


Fig. 2 Mirau interferometry objective lens

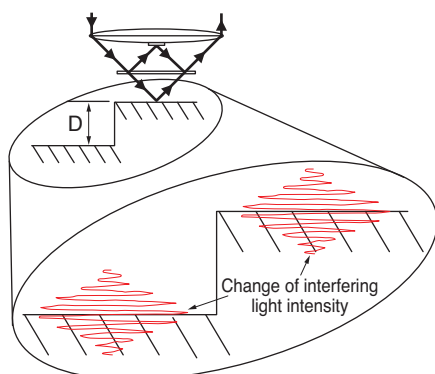


Fig. 3 Intensity variation of interfering light

2.2 Fast Measurement Processing

In order to measure the distance D between levels as shown in Fig. 3, the two-beam interference objective lens must be moved for a distance greater than D.

The speed of the move is restricted by image capture speed of the camera to be used. In this system, we adopted a high-speed camera which can capture more than 1,000 images per second. An algorithm for fast operation was created by allowing the image analysis software to calculate height measurement information from an image during capture of the following image. From the above, we achieved a minimum measurement time of 0.6 seconds for a height measurement range of 20 μm.

2.3 Configuration of the Measurement System

A photo of the measurement system is shown in Fig. 4.

Fig. 5 shows the configuration of this system equipped with automatic XY stage and automatic Z stage. The stroke of each stage is selectable depending on the size of the object to be measured. In addition, the system can be configured differently from Fig. 5, such as integrating only the optical head, the piezo stage, two-beam interference objective lens, and camera. For example, if integrated into the desktop micro application system, it is possible to verify the shape of an ink material immediately after application of the material.

Table 1 shows the system's main specifications. The resolution of the camera, and therefore the visual field size, is 640 pixels horizontally and 480 pixels vertically. The standard for height measurement range is 100 μm, depending on the stroke of the piezo stage combined in the system.

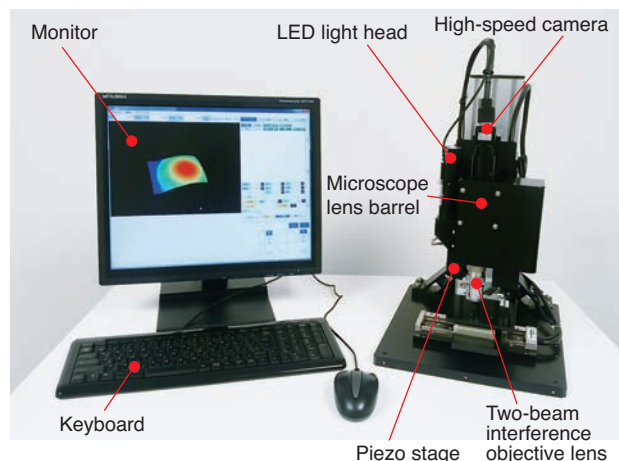


Fig. 4 Appearance of 3D microgeometry measuring machine

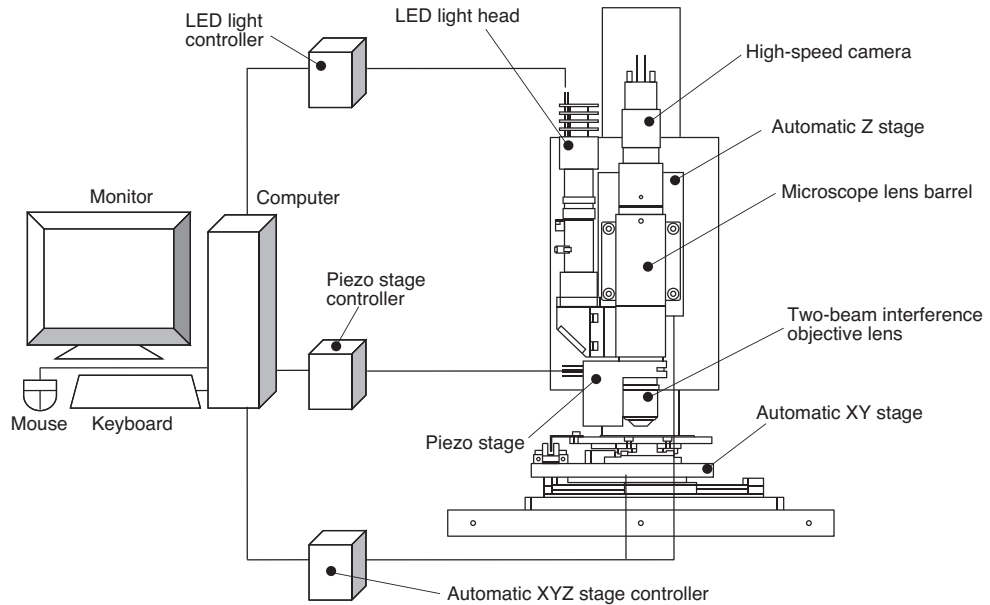


Fig. 5 Configuration example of 3D microgeometry measuring machine

Table 1 Main specifications of 3D microgeometry measuring machine

Item	Description				
High-speed camera	Monochrome CCD camera, resolution horizontal 640 pixels x vertical 480 pixels Measuring frame rate: Over 1,000 images/second				
Visual field size	x2.5	x5	x10	x20	x50
	1,280×960μm	640×480μm	320×240μm	160×120μm	64×48μm
Lighting device	White light LED coaxial episcopic illumination				
Height measurement range/resolution	100μm/5nm				
Computer	CPU: High performance unit, Memory: 4 GB				
Analysis software	License key required				
Power supply	Single phase 100V±10% 50/60Hz 15A(1.5k VA)				

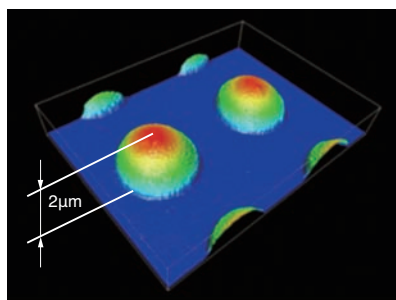
2.4 Example of Measurement

Fig. 6 (a) shows the 3D image of ink applied at a constant interval on a glass plate using the desktop micro application system. A height measurement range of 20 μm was performed in around 0.6 seconds. The actual measured height of the ink was 2 μm.

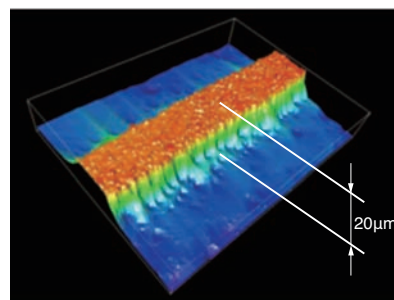
Fig. 6 (b) indicates the 3D display of a printed wiring board after etching. A height measurement

range of 30 μm was performed in around 0.9 seconds. The actual measured height of the wiring was 20 μm.

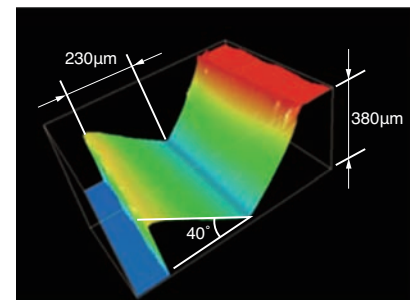
Fig. 6 (c) shows the 3D image of a metallic object made of stainless steel. A height measurement range of 500 μm was performed in around 15 seconds. The distance between the upper and bottom surfaces was 380 μm. In addition, the 2,000 μm stroke piezo stage was used for this measurement.



(a) Pasted ink on glass substrate



(b) Printed wiring board

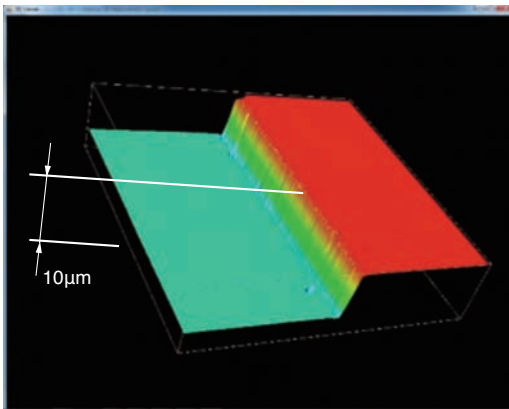


(c) Machined part

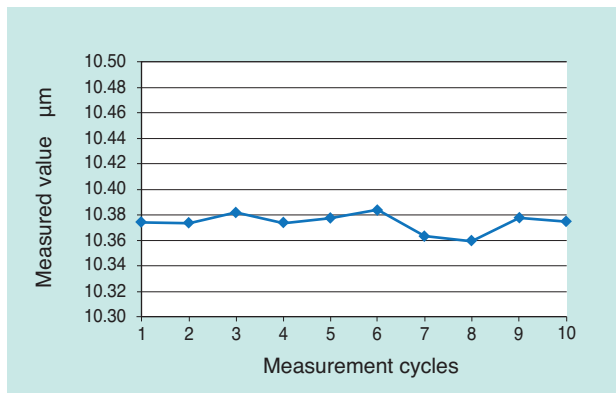
Fig. 6 Measurement result examples

2.5 Verification of Reproducibility

Fig. 7 (a) indicates the measurement results of a height master (Height master made by Mitsutoyo) of 10 μm . Fig. 7 (b) shows the results of repeated measurements. An average result of 10.374 μm and standard deviation of 7 nm (reproducibility: 0.1%) were obtained for the repeated measurement. The reproducibility was calculated from 10 repeated measurements, assuming the measurement results follow the normal distribution with a reliability of 95%.



(a) Height master: level difference of 10 micrometers



(b) Reproducibility of height measurement

Fig. 7 Height master and reproducibility

3. Image Analysis Software

The operation screen of the system is shown in Fig. 8. The operation screen consists of the various controls necessary for measurement and analysis, a result display area to show the secondary feature values such as cross sections, an image display area to show the real-time display of the images captured by the camera and the stage operation area.

By integrating the operation buttons and result display area, no new operation screens need to be opened during the measurement process allowing simple operation with two clicks of a mouse.

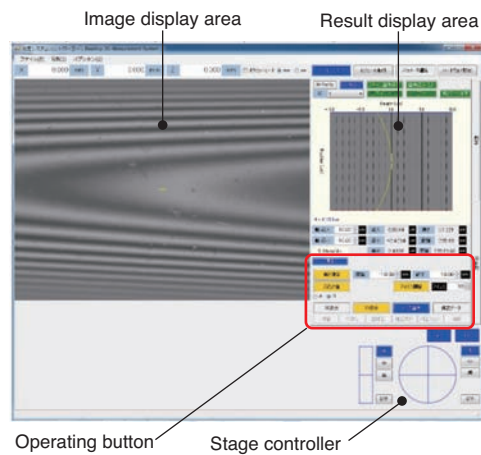


Fig. 8 Operation screen

3.1 Display of the Measurement Results

Three display functions for measurement results are available: color display, 3D display and cross section display.

• Color Display Function

Fig. 9 shows the color display result of a cylindrical object.

The color display function displays the contour-line map in color, with blue indicating the lowest area and red the highest area.

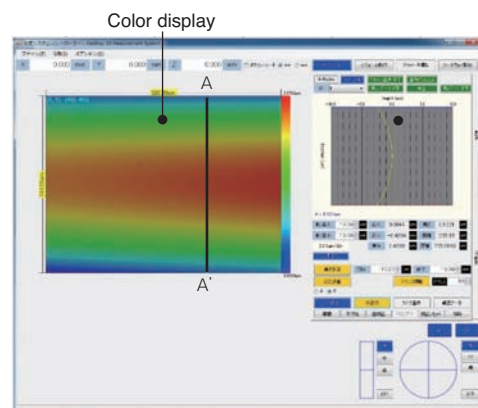


Fig. 9 Color display

● 3D Display Function

This function displays a 3D image of the measured object. It is possible to zoom in/out, shift and rotate with simple mouse operation. Fig. 6 and 7 were displayed by using this function.

● Cross Section Display Function

The height measurement results along with horizontal and vertical lines specified by the mouse on the color display, or a line determined by any two specified points, are displayed. The horizontal axis indicates the height and the vertical axis indicates the pixel position. Fig. 10 shows the cross-section display of A-A' from Fig. 9. At the bottom of the cross-section display, the maximum measurement result, minimum

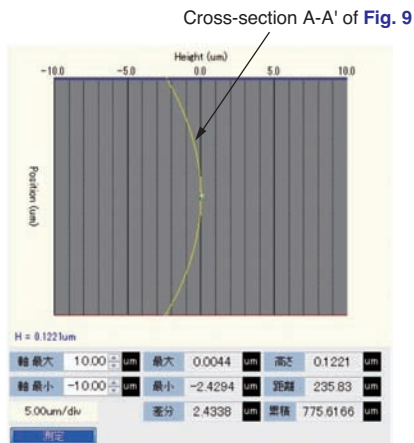


Fig. 10 Cross-section display

and their difference, height and distance of the specified two points, or the cumulative heights between those two points are displayed.

3.2 Data Correction Function

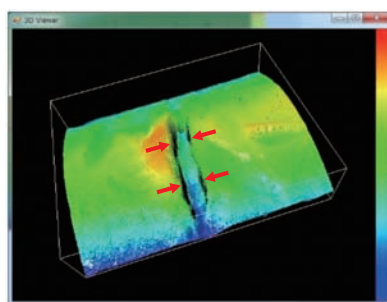
Three data correction functions are available: interpolation, smoothing and surface correction. These functions are used to clean up the measurement results by interpolating missing results and eliminating noise due to measurement errors for cleaner display or to eliminate the inclination or curvature of surface as the preprocessing of the analysis function described later.

● Interpolation

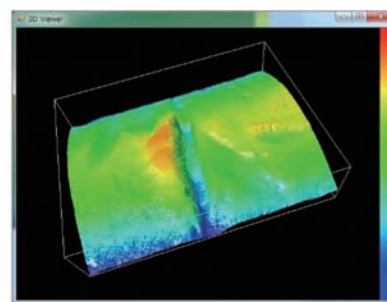
This system may not be able to obtain the interference light required by the operating principle when the height changes quickly. The measurement result shown in Fig. 11 (a) has missing height data in the black area indicated by the arrows. The interpolation function estimates the height of those pixels from the height of the proximate pixels. Fig. 11 (b) shows the 3D display after correction by interpolation.

● Smoothing

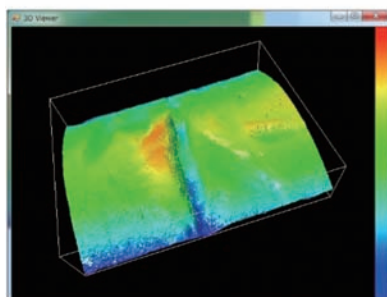
This function eliminates spike-shaped data mixed in the measurement results by smoothing. When the reflective light is low, the maximum intensity of the interference light may be erroneously measured. In that case, the smoothing function averages the data to eliminate the erroneously measured results.



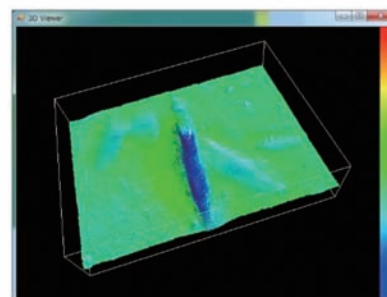
(a) 3D indication after height measurement



(c) 3D indication after smoothing



(b) 3D indication after interpolation



(d) 3D indication after quadric surface correction

Fig. 11 Application examples of data processing functions

● **Surface Correction**

Two types of surface correction functions are available: plane correction and quadric surface correction. The plane correction converts a sloped surface into a plane and the quadric surface correction converts a quadric surface into a plane. Fig. 11 (a) indicates the 3D display of the cylindrical object of 6 mm of diameter. The 3D images after interpolation, smoothing and quadric surface correction are shown in Fig. 11 (b), (c) and (d), respectively. It can be seen that Fig. 11 (d) eliminated curvature in Fig. 11 (c).

3.3 Analysis function

Three analysis functions are available: automatic level measurement, automatic volume measurement and surface roughness analysis.

● **Automatic Level Measurement Function**

This function automatically calculates the maximum height (level difference) of the tested area from the base surface. Fig. 12 shows the measurement results of a 10 μm height master. The area surrounded by the red frame in Fig. 12 (b) is the base surface and the area surrounded by the blue frame is the tested area which can be arbitrarily set. The detected level difference is displayed in the title field on the top left in the measurement window. In the example of Fig. 12 the calculated level difference was 10.266 μm.

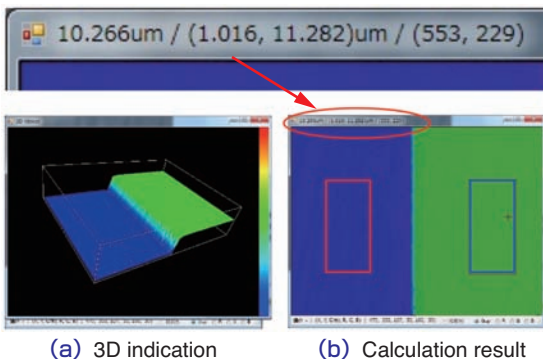


Fig. 12 Example of measurement of level difference

● **Automatic Volume Measurement Function**

This function is used to calculate the diameter, height and volume of a sphere automatically. Fig. 13 shows the measurement of volume of spherical ink applied by the desktop micro application system. The area surrounded by the red frame in Fig. 13 (b) is the base surface and the yellow frame indicates the bounding rectangle of the spherical ink, which is automatically detected by image processing. The height of the detected ink, diameter and volume are

displayed in the title field on the top left of the measurement window. In the example of Fig. 13, a spherical object with a height of 3.444 μm relative to the base surface, diameter of 174 μm and volume of 0.041 nl was measured.

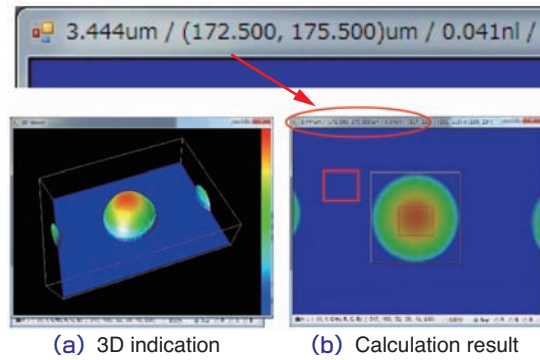


Fig. 13 Example of volume measurement

● **Surface Roughness Analysis Function**

Two functions are available: line roughness area roughness. In the line roughness calculation, roughness information is calculated along a horizontal, vertical or angled line segment. In the area roughness calculation function, roughness information is calculated from the measured values within the specified range. Fig. 14 is an example of line roughness measurement result, calculated along the red line segment.

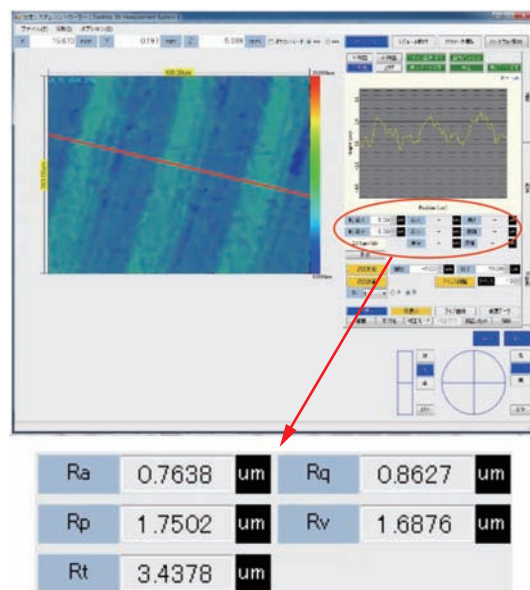


Fig. 14 Display example of line roughness

4. Conclusion

This paper introduced the features of the 3D micro-geometry measurement machine capable of the fastest operation in its class.

The micro machining technologies is used in research and development in various fields such as semiconductors, electronics and medicine, and their application range is expanding. The requirement for quickly measuring, displaying and verifying micro-shaped objects is expected to grow, as high reliability is required in the production line for maintaining product quality.

With this system we will continue to improve performance and enhance functions for the products that contribute to the functions and quality of the micro processed products in research and development, as well as in the production process where high reliability is required.

Reference

- 1) Kieran Gerald Larkin, "Efficient nonlinear algorithm for envelope detection in white light interferometry", J. Opt. Soc. Am. A, Vol.13 (1996) , No.4, 832-843
- 2) Toyohiko Yatagai, "Recent Progress in Optical Interferometric Measurement", Journal of the Japan Society of Precision Engineering Vol. 51 (1985), 33-40
- 3) Hiroshi Kubota, "Coherency of Light and its Application", SEISAN KENKYU Vol. 15 (1963), No. 10, 410-414
- 4) Akiko Harasaki, Joanna Schmit and C. Wyant, "Improved vertical-scanning interferometry", APPLIED OPTICS, Vol.39 (2000) , No.13,2107-2115

Photo of author

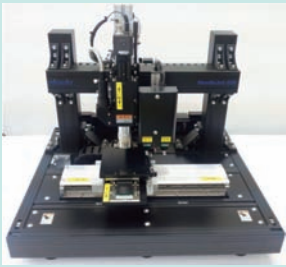


Hiroaki OBA

New Product Development
R&D Center

High-speed Microscopic Coating Applicator

Akihiro YAMANAKA*



In 1990, NTN started manufacture and sell the system to repair defects that have occurred in the production process of flat panel display, there are many adoption proven. Core technology of this repair system are high-precision positioning technology with precision stages, fine processing technology with laser beam and fine pasting technology with pasting needle. In particular, the fine pasting technology is a unique pasting method of NTN, and we can paste many kinds of liquids in a stable with this technology, there are many adoption proven in the repair application for the color filter of a liquid crystal display.

This paper explains newly developed high-speed microscopic coating applicator for the purpose of application deployment of fine pasting technology.

1. Introduction

NTN has been developing and providing pattern correction devices since 1990, which repair flat panel display (FPD) defects produced in the manufacturing process, for use by many FPD manufacturers. These devices make a significant contribution towards reducing the environmental load and FPD manufacturing cost by reducing the number of failed boards which otherwise would have been discarded.

The core technologies of these devices are highly precise positioning technology with precision stages, fine film micro-machining technology with laser, and micro application technology using application needles. Particularly, the micro application technology is the NTN proprietary technology which received the mechanical component award of the “Cho” MONODZUKURI Innovative Components Awards from the Nikkan Kogyo Shimbun Ltd.

This paper introduces the high-speed microscopic coating applicator, which is newly developed for deployment in new fields, leveraging the microscopic application technology principle, and superb feature of adaptation of various types of liquid.

2. Microscopic application technology using application needle method

2.1 Shape of the application needle and application principle

The application needle has a flat surface on the conical tip, as shown in Fig. 1. When the application material (ink) is supplied to the application needle, the material moves up along the application needle by surface tension, as shown in Fig. 2, leaving a fixed amount on the flat surface of the tip. Stable microscopic application is achieved by transferring this application material onto the flat surface of the application surface, as shown in Fig. 3.

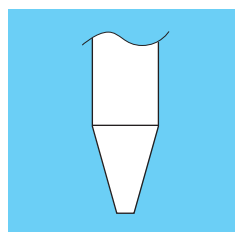


Fig. 1 Shape of needle tip

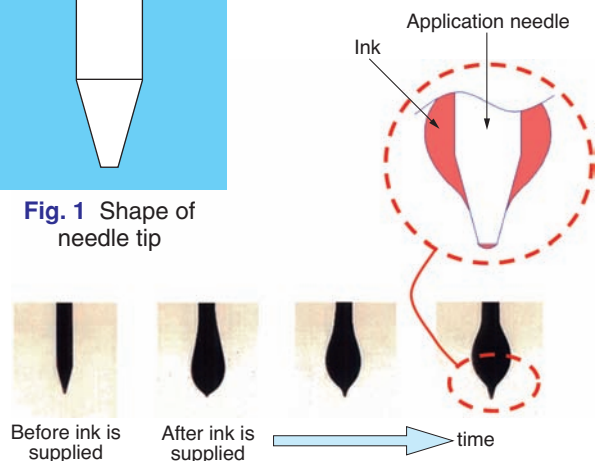


Fig. 2 Supply of application material to application needle

*New Product Development R&D Center

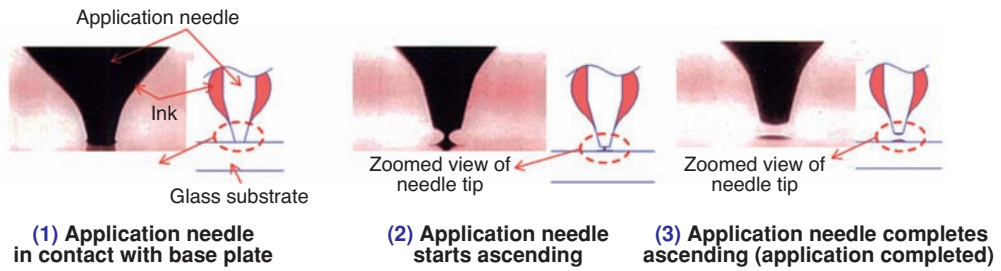


Fig. 3 Pasting process

2.2 Configuration of application needle unit

The application needle unit is configured with the application needle and application material container, which are supported by the application needle support, as shown in Fig. 4. The application needle and application material container are fixed to the application needle support by a magnet to allow easy replacement.

The application material container has holes at the top and bottom so that the application needle can be inserted through. The needle is inserted from the top hole. The application needle is constantly immersed in the application material injected to the application material container, maintaining the application material adhered to the tip of the application needle.

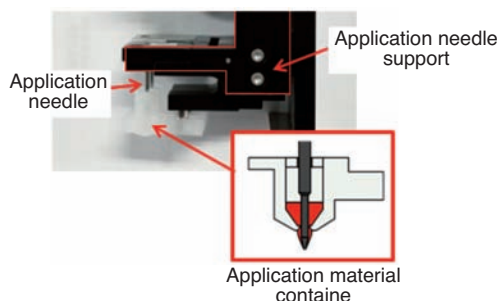


Fig. 4 Support construction of application needle and application material container

When the material is to be applied, the tip of the application needle is pushed out from the bottom hole of the application material container, and the application needle tip makes contact with the surface to apply the application material, as shown in Fig. 3. The application needle is fixed to the sliding mechanism which can move up and down, and the contact pressure is kept constant.

2.3 Features of application needle method

Fig. 5 shows two examples of conventional application methods. Since the application needle method supplies the application material on the outer perimeter of the application needle, no clogging

occurs, unlike the conventional method which uses a nozzle. Therefore, one of the devices greatest features is that it can reliably apply materials with a broad range of viscosity. The comparison with the conventional application methods is given in Table 1 and an example of application by the application needle method is shown in Fig. 6.

In this example the application material was a silver paste with a high viscosity and even after 500 uses there was only a slight change in application diameter, proving consistent application.

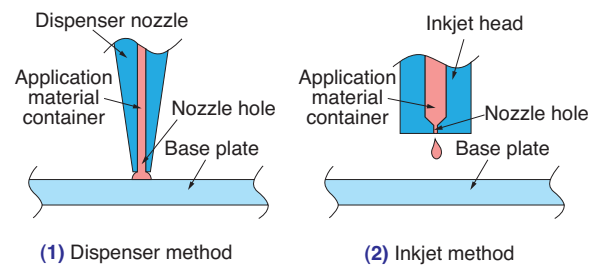


Fig. 5 Conventional application methods

Table 1 Comparison with the conventional application method

	Application needle method	Conventional application methods	
		Dispenser method	Inkjet method
Application size	Diameter >15μm	Diameter >100μm	Diameter >20μm
Application amount	> several p l	>several μ l	5p l to 2000p l
Viscosity of application material	1~1x10 ⁵ mPa · s	50~3x10 ⁵ mPa · s	1~40mPa · s
Clogging	No	Yes	←
<Application> Microscopic application of high-viscosity material	○	△	×

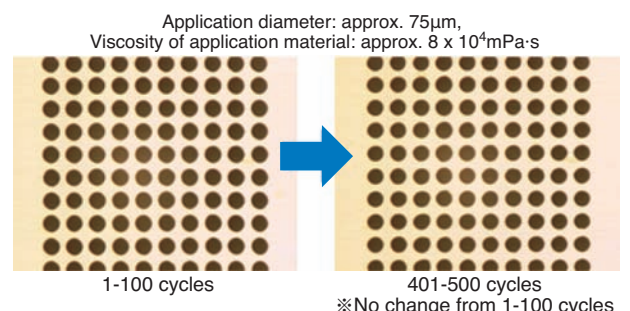


Fig. 6 Example of application

3. High-speed microscopic coating applicator

As the microscopic application technology is extended to new applications such as volume production of electronic devices and circuit pattern drawing, the precision and consistency of the application method gained a great reputation. However, the challenge was the reduction of tact.

Therefore, we have developed an application mechanism to achieve application time of 0.1 second as opposed to 2.4 seconds required by the conventional FPD pattern correction devices, which is 24 times faster.

3.1 High-speed application mechanism

We have implemented a combination of a motor and cam for driving the application needle up and down as the high-speed application mechanism. The rotation of the motor is converted to linear motion using a cam to move the application needle up and down.

Fig. 7 shows the high-speed application mechanism. We have optimized the motor control and cam geometry to reduce the strong impact from high speed vertical motion at the instance the application needle makes contact with the application surface, and reviewed the structure of the application needle holder to reduce the weight of the application needle support. Fig. 8 shows the application needle holder.

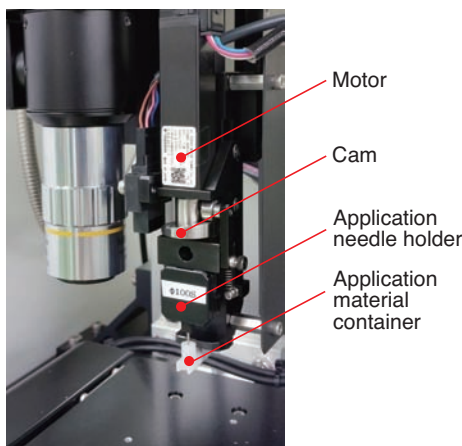


Fig. 7 High-speed application mechanism

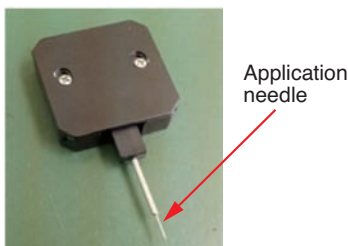


Fig. 8 Application needle holder

The sliding mechanism was integrated into the application needle holder to reduce the size and weight of the application needle support. Due to these features, the impact load at the instance that the application needle makes contact with the application surface was reduced to approximately 0.06 N and the contact load during application to approximately 0.03 N.

Table 2 shows the comparison between the newly developed high-speed application mechanism and the conventional application mechanism.

Table 2 Comparison of conventional pasting unit

Application method	Application speed	Contact load
Conventional application mechanism	2.4 sec/application	Approx. 0.07N
High speed application mechanism	0.1 sec/application	Approx. 0.03N
Ratio	x24	Less than half

3.2 High-speed microscopic coating applicator

Fig. 9 shows an example of the high-speed microscopic coating applicator (hereinafter, applicator) with the high-speed application mechanism. The system shown here is equipped with 2 application mechanisms which make it possible to install multiple application mechanisms in a system. By installing multiple units, the system can be used for application of different sizes and different materials.

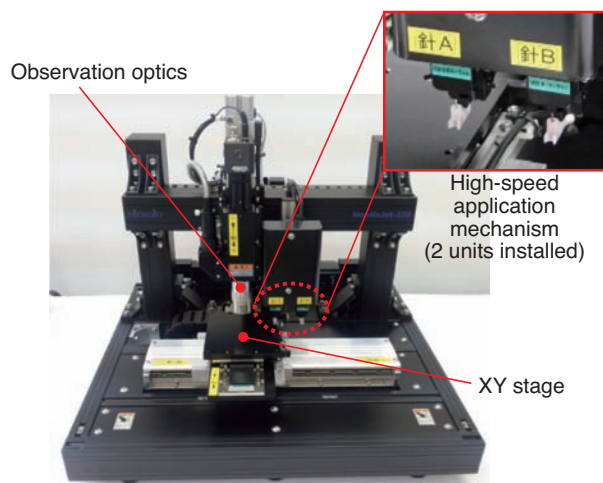


Fig. 9 High-speed microscopic coating applicator example

1) User interface

The operation of this system is controlled by input from the mouse in the operation screen shown on the display of the computer. Fig. 10 shows an example of the operation screen.

This screen displays an image of the application surface in the observation image display area. The position for material application can be chosen by clicking the mouse on this image. The mouse can also be used to move the XYZ stage by clicking in the XYZ stage operation instruction area shown in the bottom right of Fig. 10.

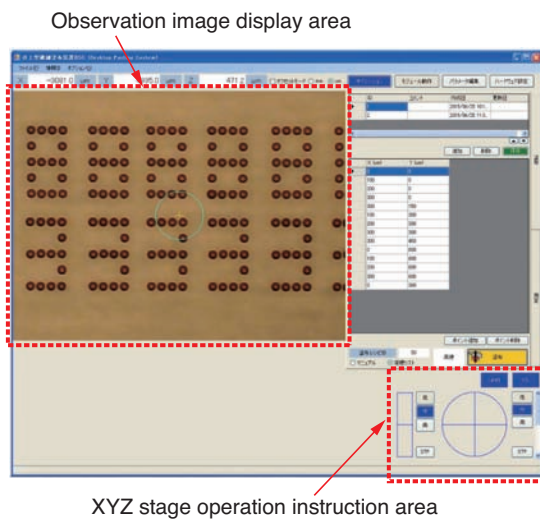


Fig. 10 Operation screen of high-speed microscopic coating applicator

2) Application mode

There are 6 types of application modes provided as standard modes in Fig. 11.

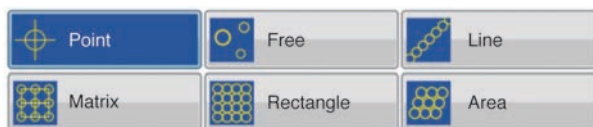


Fig. 11 Application modes

(1) Point application mode

Application occurs at the cross mark position of the observation image display area (center of image).

(2) Free application mode

Application occurs at the position specified by the mouse click in the observation image display area.

(3) Line application mode

By specifying the starting point and end point of a line by the click of the mouse in the observation image display area, a line is applied at the predetermined pitch.

(4) Matrix application mode

By specifying the pitch and number of dots for XY directions, a matrix is applied.

(5) Rectangle application mode

By specifying the top left and bottom right corners of the rectangle with the mouse, a rectangular area is applied.

(6) Area application mode

Similar to the rectangle application mode, by specifying the top left and bottom right corners, a diamond shaped area is applied.

In addition to the above, the following automatic bulk application operations are optionally available.

(7) Automatic bulk application to the registered coordinates

As shown in the observation image display area of Fig. 10, the positions indicated with the pre-registered coordinates are automatically applied in bulk.

(8) Automatic bulk application with CAD data

Automatic bulk application is available by the image data of the BMP format and CAD data of the DXF format.

3) Other options

Our 3D micro-geometry measurement machine, which is introduced separately, can be optionally installed, which allows verification of the application shape and evaluation of the application area immediately after the application. Fig. 12 shows an example of the measurement of application shape.

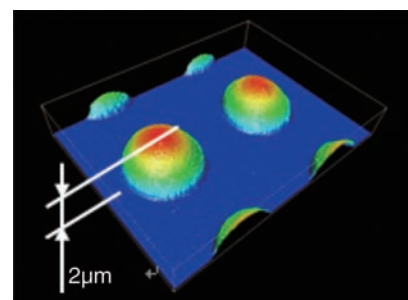


Fig. 12 Measurement of application example

4) Specification and configuration example of high-speed microscopic coating applicator

An example of specification of the basic configuration is shown in Table 3 and the outline view is shown in Fig. 13

This compact system can be operated with 100VAC and requires an area of 300 square millimeters to operate. Trial applicator can be rented out for evaluation.

Table 3 Specification of high-speed microscopic coating applicator as an example

Item	Description
Application unit	Application speed: 0.1 s/application or more Accuracy of application positioning: $\pm 15\mu\text{m}$ or less (reproducibility)
Application needle	Number of installable needles: 1 Diameter of application needle tip : $\phi 10\mu\text{m}$ or larger (determined by prearrangement)
Optical unit	Microscope lens barrel: Clear vision single eye microscope lens barrel Objective lens: Ultra long operating distance objective lens: 1 (x10) Visual field on image: 0.48x0.64mm Lighting: 100W halogen lamp Cold light with fiber (length of fiber: 1m)
Stage unit	XY stage : Stroke : (determined by prearrangement) Resolution : $0.1\mu\text{m}/\text{pulse}$ Maximum speed : 200mm/s Z stage : Effective stroke : 35mm Resolution : $0.2\mu\text{m}/\text{pulse}$ Maximum speed : 10mm/s
Control unit	Computer Main unit : FA/PC Monitor : 17 inch LCD color display (1 unit) Language : OS/Application Japanese (Windows 7 Professional)

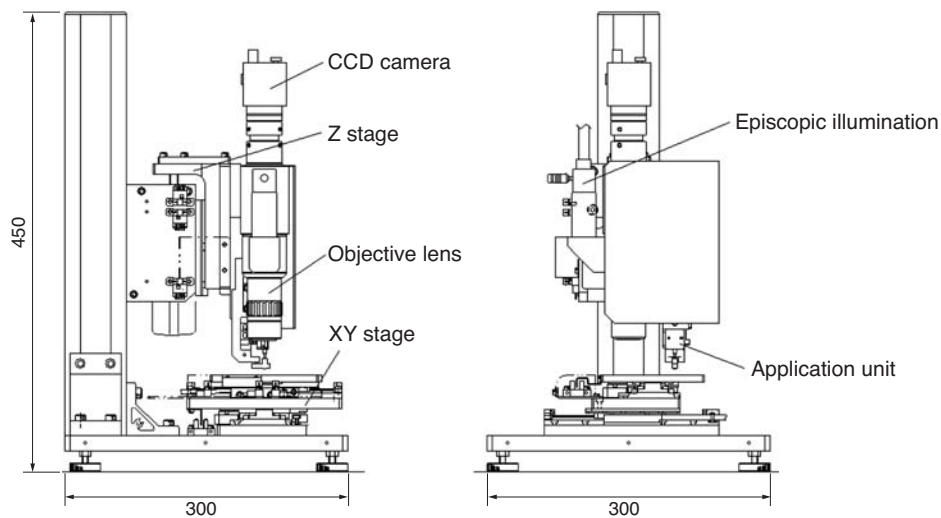


Fig. 13 Outline view of high-speed microscopic coating applicator

5) Examples of application

Currently, specific evaluations and studies are being conducted in various fields including correction of electrodes of high-density printed wiring board (PWB), mounting of electronic components, application of catalytic material on sensors, application of agents in bio-related area, application of conductive paste in the printed electronics field, etc. **Fig. 14** shows examples of the application of low-viscosity material and conductive paste on a printed wiring board. As shown in **Fig. 14 (3)**, the electrode pattern can be directly drawn by applying the conductive paste. The high-speed and stable operation of this proposal is already

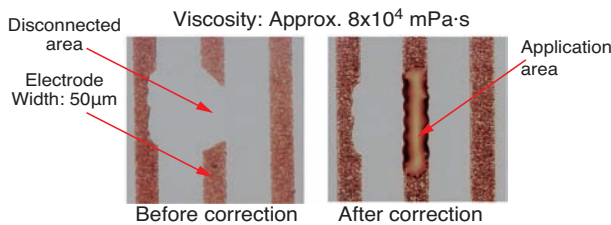
recognized in various applications and it is adopted in volume production process.

As mentioned above, application materials of a broad range of viscosity can be applied precisely, quickly, and reliably by using the high-speed microscopic coating applicator. We believe the use of this technology will be extended to many other fields.

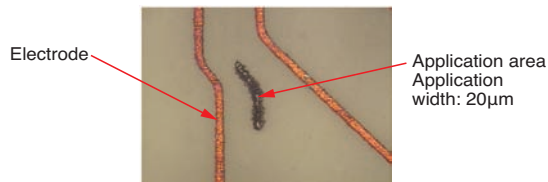
Viscosity: Approx. 70 mPa·s,
application diameter: approx. 50μm



(1) Application of low-viscosity application material (color ink) example



(2) Correction of electrode in printed wiring board example



(3) Application on PWB example

Fig. 14 Application example

4. Conclusion

This article introduced the high-speed microscopic coating applicator.

NTN is conducting research aimed at the development of highly reliable application of a broad range of materials, in addition to the high speed application we introduced, with the microscopic application method using our unique application needles.

The demand for fast and stable microscopic application is growing in new fields such as electronic micro-components and bio-related fields. We will continue to develop systems to contribute to research, development, and production in these fields.

Reference

- Yamanaka, Monthly magazine "Display", Dec. 2004 issue.
- Yamanaka, "Complete Works of color filter material development and manufacturing processes", Technical Information Institute Co., Ltd., July 2006 issue
- Yamanaka, Monthly magazine "Display", Dec. 2006 issue.
- Saruta, NTN TECHNICAL REVIEW No. 72, (2004).
- Yamanaka and Matsushima, NTN TECHNICAL REVIEW No. 72, (2004).
- Yamanaka and Matsushima, NTN TECHNICAL REVIEW No. 76, (2008).
- Suzuki, Monthly Tribology, No. 294 (2012) 34-36.
- Uchiyama, "Precision thin film coating technology using wet process", Technical Information Institute Co., Ltd., Aug 2014 issue

Photo of author



Akihiro YAMANAKA
New Product Development
R&D Center

2014 “CHO” MONODZUKURI Innovative Components Awards Automotive Components Award

Mechanical Clutch Unit for Direct Adaptive Steering

Naotsugu KITAYAMA Shintaro ISHIKAWA

1. Introduction

NTN’s “Mechanical Clutch Unit for Direct Adaptive Steering” (hereinafter, “MCU for DAS”) received the Automotive Component Award at the “2014 “CHO” MONODZUKURI Innovative Components Awards” sponsored by the Monodzukuri Promotion Council and the Nikkan Kogyo Shimbun, Ltd. (Assisted by Ministry of Economy, Trade and Industry, The Japan Chamber of Commerce and Industry).

“MCU for DAS” is a product adopted as the mechanical back-up mechanism for the world’s first DAS system for mass produced vehicles that Nissan Motor Co., Ltd. introduced to the market. It uses a compact configuration combining an electromagnetic clutch and roller clutch, and switches torque transmission on and off depending on the presence of electrical power.

* Registered trademark of Nissan Motor Co., Ltd.



Photo: Courtesy of Nissan Motor Co., Ltd.

2. Structure of mechanical clutch unit

“MCU for DAS” is a product that NTN developed as a new mechanical element to switch the torque transmission between the input and output shafts.

When DAS is functioning, the roller clutch is released by electrical power supplied to the electromagnetic clutch, and the steering operation is transmitted to the tires through electrical signals. On the other hand, when the electrical power to the electromagnetic clutch is not supplied, the roller clutch is instantly engaged to mechanically transmit the steering operation to the tires, achieving a fail safe capability.

In addition to the electromagnetic clutch and roller clutch, a pair of rollers are arranged, as well as the newly adopted ball cam mechanism (converting the axial linear motion to rotating motion) to reduce the backlash when mechanically connected, realizing the clutch characteristic of high torque capacity.

This product is introduced separately in detail.

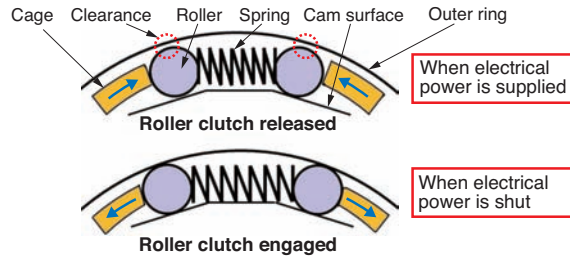


Fig. 1 Roller clutch mechanism

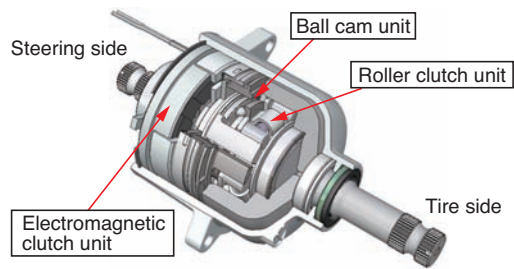


Fig. 2 Component

3. Conclusion

This product realized the reliability that customers require by adopting a linear/rotation conversion mechanism (ball cam) into NTN’s proprietary roller and electromagnetic clutch. We will continue to develop new products that support next-generation vehicle technologies.



Commendation of Cho-monodzukuri award

Photo of authors



Naotsugu KITAYAMA
Automotive Business HQ



Shintaro ISHIKAWA
Automotive Business HQ

AVEC'14 Best Paper Award

Roll Control Using Tire Longitudinal Forces Integrated with Tire Force Distribution of Full Drive-by-Wire Electric Vehicle

Yuta SUZUKI Tomohiro SUGAI Junichi HIRATA Nobuyuki SUZUKI

1. Introduction

The paper of the above title, which presented the results from joint research with the Kanagawa Institute of Technology, received the “AVEC'14 Best Paper Award” at the “International Symposium on Advanced Vehicle Control” which took place at Tokyo University of Agriculture and Technology in September, 2014. This symposium is an international conference regarding vehicle motion performance and control, sponsored by the Society of Automotive Engineers of Japan. Since its first conference held in 1992 in Yokohama, it has been held in various venues throughout the world such as Germany, the U.S. and Taiwan every two other year, and has become one of the world's leading places for automotive engineers and researchers to present state-of-the-art technologies. In this article, we briefly introduce this award winning research.

2. Control method

By installing in-wheel motors for each wheel, it is possible to independently control the driving force for each wheel very quickly and accurately. In addition, the controllability will increase with full drive-by-wire vehicles, which are able to independently steer four wheels. Fig. 1 shows an experimental vehicle equipped with the above system.

When longitudinal forces are applied to the tires from the in-wheel motors, the vehicle receives vertical force through the suspension mechanism. Past research has demonstrated that by applying longitudinal forces in opposite directions, between the front and rear wheels or between the left and right wheels, vehicle roll can be controlled by leveraging this effect.

However, due to the behavior of the tires, the active use of longitudinal forces reduces the lateral forces. Consequently, the application of this roll control during a turn, where high lateral gravitational forces are put on the vehicle, increases the tire load ratio on the turning inner wheels, reducing the lateral forces, which may make the vehicle behavior unstable. Therefore, leveraging the properties of the full drive-by-wire vehicle, the increase of the tire load ratio can be reduced during roll control, by applying the roll control while distributing the longitudinal forces and lateral forces to all four wheels so that the load on each wheel becomes uniform.



Fig. 1 Experimental Full Drive-by-Wire EV

3. Test results from an actual vehicle

We conducted a lane change experiment to the left lane, assuming an emergency avoidance situation. Fig. 2 shows the results. The tire load ratio on the rear turning inner wheel is significantly increased by the longitudinal force when only roll control is applied (green line) compared to no control (blue line). However, when roll control, integrated with the tire force distribution control (red line) is applied, the tire load ratio is uniform between the left and right wheels without a significant increase on the rear wheels. From this experiment, using an actual vehicle, we could verify that the roll control with longitudinal forces requires an integration with vehicle stabilization control, such as tire force distribution control.

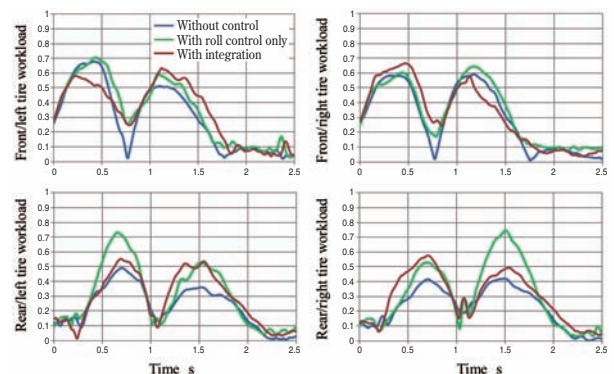


Fig. 2 Work-load of each tire

4. Conclusion

We will continue exploring vehicle motion control leveraging motor response and high accuracy of in-wheel motors to make the EV system more effective.

Photo of author (presenter)



Yuta SUZUKI

Chassis System Engineering,
EV Module Business HQ

Self-Aligning Roller Bearing (ULTAGE EMA type)

Optimized internal design: maximized size and number of rollers
The world's highest level of high load-carrying capacity is achieved!

ULTAGE



Features

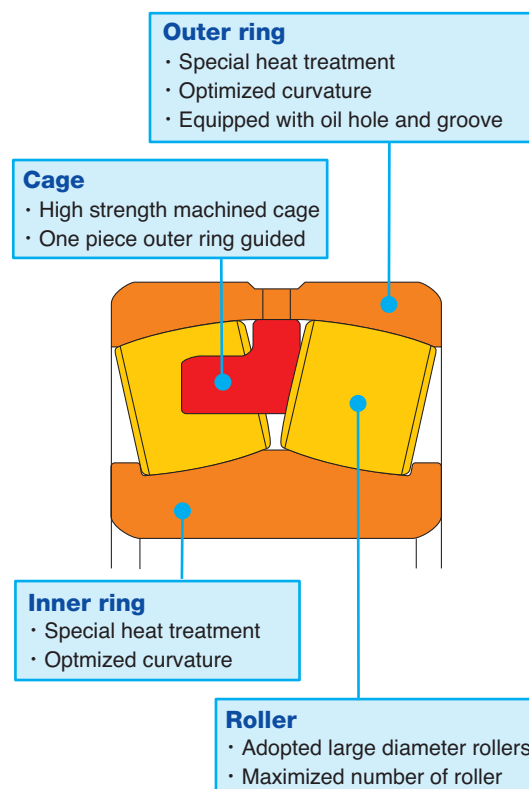
- (1) **World's highest level of load-carrying capacity**
 - Basic dynamic load rating: Improved by up to 20%*
- (2) **Superior vibration resistance and impact load tolerance**
 - Cage strength: Improved by up to 55%*
- (3) **Low heat generation**
 - The rise of temperature in the bearings is reduced by up to 10% under vibration/impact load test conditions*
- (4) **Heat resistant up to 200°C**
 - Dimensional stability and long life are achieved in a high temperature environment by adopting special thermal treatment

*Compared with our UA type product

Applications

- **Crushing machines, grinders, disintegrators, vibrating screening machines, reducers, etc.**

Structure



Wireless Measurement Unit for Condition Monitoring System (CMS)

World's first! The condition monitoring capability is improved by using **wireless communication for condition monitoring of wind power generators!**



Features

(1) Wireless communication creates a connection between the data collection device and sensors

- Compact design allowing for ease of installation on rotating components - Measurements are possible even in areas where cabling installation is prevented
- Simultaneous measurement of two signals (2 channel input)

(2) Available for off-shore and severe conditions

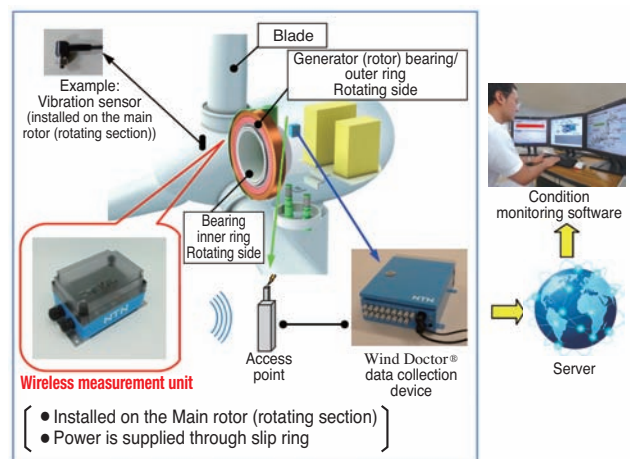
- Dust/water proof performance complies with JIS C 0929 IP65

Applications

- Wind power generators, various machines, test/inspection devices, etc.

Structure

- Example of synchronous type wind turbine, bearing outer ring and rotor rotation



Size and weight of unit

Size : 130 mm W x 180 mm D x 102 mm H
 Weight : 550 g
 (Water protection cover is available)

Resin-made Thrust Rolling Bearings for Food Processing Equipment

Resin-made rolling bearings with **superior performance** and **easy handling**



Features

Adoption of heat tolerant resin and ceramic balls

- (1) Lightweight and corrosion resistant design
- (2) Ensures heat tolerant performance up to 200°C

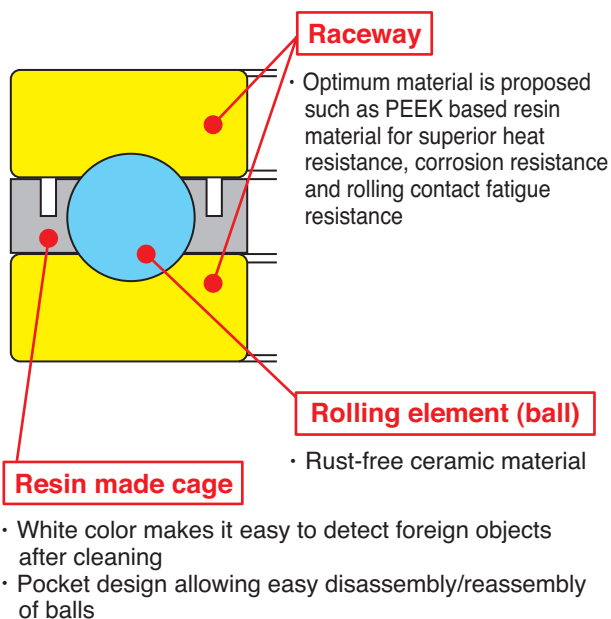
Maintenance conscious material blending and design

- (3) Superior handling performance is achieved due to easy cleaning
- (4) White color makes it easy to detect foreign objects after cleaning

Applications

- Food processing equipment (stirrers and pumps), medical devices, underwater equipment, clean-room environments

Structure



NTN's advanced technologies and services actively used in various fields

NTN®

Aerospace



Three-point contact ball bearings for jet engines

High speed railroad



Bearings for axle shafts of Hokuriku Shinkansen cars

Automotive



Press connect spline hub joint



Sensor-integrated 3rd generation hub bearings

Machine tools



Bearings for ball screw support



Angular contact ball bearings with lubrication holes

Aftermarket



Technical training session by specialized staff



Technical service car



Various maintenance tools